

SYNTHESIS AND CHARACTERIZATION
OF
ORDERED MESOPOROUS TRANSITION METAL OXIDES AND NITRIDES

A Dissertation

Presented to the Faculty of the Graduate School
of Cornell University

In Partial Fulfillment of the Requirements for the Degree of Doctor of Philosophy

by

Spencer William Robbins

January 2015

© 2015 Spencer William Robbins

SYNTHESIS AND CHARACTERIZATION OF
ORDERED MESOPOROUS TRANSITION METAL OXIDES AND NITRIDES

Spencer William Robbins, Ph. D.

Cornell University 2015

Controlling the structure of inorganic materials on the mesoscale (2-50 nm) is desirable for many applications and can influence the materials' properties and performance in devices. Amphiphilic block copolymers (BCPs) have been used extensively to structure-direct transition metal oxides, controlling their mesoscale morphology. By selectively incorporating metal oxide precursors into one block of the BCP and removing the BCP through thermal decomposition, ordered mesoporous metal oxides with well-defined mesoscale morphologies can be achieved that are interesting, *e.g.* for energy conversion and storage applications.

This dissertation reports on the amphiphilic block terpolymer poly(isoprene)-*block*-poly(styrene)-*block*-poly(ethylene oxide) used in combination with sol-gel metal oxide precursors to generate ordered three-dimensionally (3D) mesoporous metal oxides. 3D co-continuous cubic network structures such as the alternating gyroid are particularly interesting for energy applications due to their chirality, co-continuity, and high porosity. In particular, the high porosity and mesoscale dimensions can facilitate rapid diffusion of gases/liquids, but limit solid state diffusion lengths in the inorganic structure during chemical conversions of the oxides, *e.g.* nitriding.

Freestanding gyroidal mesoporous metal oxides can be further processed into gyroidal mesoporous metal nitrides by heating under flowing ammonia gas. Transition metal nitrides are

of interest due to their electrical conductivity and electrochemical stability. The development of a synthesis for 3D ordered mesoporous nitrides opens paths for studying the effects of well-defined block copolymer mesostructures on superconductivity, an exciting new field.

BIOGRAPHICAL SKETCH

Spencer William Robbins was born in Poughkeepsie, NY on July 25th 1987. He was raised in nearby Hopewell Junction, NY, just outside the New York metro area. From a young age, Spencer was interested and passionate about science—including participating in a young scientist club as early as elementary school. Throughout middle school and high school, his interest in science continued to grow.

Spencer's interest in chemistry was solidified upon taking Honors and AP Chemistry courses. Chemistry came naturally to him, and the ability to explain the world around him was a powerful tool. By the time he graduated high school, Spencer knew he would pursue chemistry, including a graduate degree. He would begin to achieve this goal in 2005 as he moved north to Binghamton University to begin college. He continued to excel in his studies in college and began to learn more about academic research opportunities in the chemistry field. Around the same time, he discovered the field of materials science—a topic barely touched throughout his years of chemistry classes.

As it turned out, the university offered a 3-2 Bachelors-Masters program in chemistry and materials science, in which he promptly enrolled. While researching under Prof. Omowunmi Sadik for several years, Spencer completed the B.S. and M.S. coursework in a total of 4 years. However, before completing the thesis for the M.S., applications and acceptances to Ph.D. chemistry programs came through. Impressed by its strongly interdisciplinary culture, and armed with his knowledge of chemistry and materials science, Spencer began pursuing his Ph.D. at Cornell University in 2009, in the Department of Chemistry and Chemical Biology, in lieu of completing his M.S. at Binghamton.

The transition to the Ph.D. program was at times rocky. However, after a year of teaching Physical Chemistry labs and taking classes, things began to settle into place for Spencer. He had initially joined Prof. Francis J. DiSalvo's solid state chemistry group in the Department of Chemistry and Chemical Biology to work on materials for energy applications, but continued to year for even more interdisciplinary research. In the spring of 2010, that opportunity came from Prof. Ulrich Wiesner and his polymer science group in the Department of Materials Science and Engineering. As a joint student between the DiSalvo and Wiesner groups, Spencer continued a fruitful collaboration that dated back several Ph.D. students. His work developed into combining the expertise of inorganic materials in the DiSalvo group with the expertise of block copolymers and self-assembly in the Wiesner group.

In his spare time, Spencer enjoys various activities including sports with friends and colleagues, tinkering with computers and electronics, riding his motorcycle, painting, and simply relaxing.

This dissertation is dedicated to my parents, brother, and friends who provided me countless opportunities and unconditional support. I would have no such success without all of you.

ACKNOWLEDGEMENTS

I must acknowledge a great number of people who have made my achievements possible.

First, I want to thank my co-advisors: Prof. Frank DiSalvo and Prof. Uli Wiesner for giving me the opportunity and means to do meaningful work throughout my Ph.D. My third committee member, Prof. Tobias Hanrath has also been an indispensable resource of knowledge and encouragement for which I thank him.

Other faculty members who have contributed explicitly or implicitly in my career at Cornell include Prof. Sol M. Gruner, Prof. R. Bruce van Dover, Prof. Poul Petersen, Prof. William Dichtel, Prof. Héctor Abruña, and Prof. James Sethna.

I must also acknowledge my predecessors for their work and insight that set me up for success from the time I walked in the door. Their guidance, patience, and research contributions paved the way for my research and success and for that I am grateful. Specifically, I would like to thank Dr. Ray Burns, Dr. Chinmayee Subban, Dr. Chris Orilall, Prof. Morgan Stefk, Prof. Scott Warren, and Dr. Juho Song, and Dr. Balthazar Lechêne.

My colleagues were also instrumental in supporting me both in and out of the lab. I could probably not hand pick a better group of people to work with. Specifically, Jörg Werner, Yibei Gu, Dr. Kwan Wee Tan, Dr. Rachel Dorin, Dr. Yao Sun, Dr. C Cowman-Eggert, Dr. Hiroaki Sai, Dr. Tobias Hoheisel, Prof. Kahyun Hur, and Zihui Li are just a few of the many positive influences on me at Cornell. I would also like to thank Dolores Dewbury and Kelly Case for their constant support, conversation, and ensuring that I follow through with what I need to do.

I must also acknowledge my collaborators for all their contributions to this work. Dr. Hiro Sai was involved with all my work, providing countless ideas, telling me when and why I'm wrong, and measuring countless numbers of SAXS samples. Jörg Werner also measured numerous SAXS samples, provided constant feedback on my projects and helped with polymer

synthesis and ethanol studies. Dr. Kwan Wee Tan lent his impressive SEM imaging skills to provide some of the publication quality images. Peter Beaucage also measured many SAXS samples and has continued and expanded upon my work with his expertise in X-ray scattering. Ji-yeob Kim helped with the larger ISO Nb₂O₅/NbN work. Dr. Dave Moore and Dr. Yao Sun helped with optical characterization of various materials. External collaborators have helped expand the breadth of my work, especially Prof. Mikhail Noginov and Srujana Prayakarao at Norfolk State University and Prof. Dominik Eder and Dr. Alexey Cherevan at WWU Münster.

I also need to thank the funding and facilities, especially the Energy Materials Center at Cornell (emc²) for funding, the Cornell Center for Materials Research (CCMR), the Cornell Nanoscale Science and Technology Facility (CNF), and the Cornell High Energy Synchrotron Source (CHESS) for facilities. The associated staff were indispensable throughout my time including Dr. Paul Mutolo, Dr. Jon Shu, Steve Kriske, John Grazul, Don Werder, Dr. Kit Umbach, Dr. Arthur Woll, Phil Carubia, and Tony Condo.

Finally, I thank my parents, my brother, my friends back home, and my friends at Cornell. Without all of your nearly infinite patience and support for me, there is no way I would have been able to do this.

TABLE OF CONTENTS

Biographical Sketch.....	iii
Dedication.....	v
Acknowledgements.....	vi
Table of Contents.....	viii
List of Figures.....	ix
List of Tables.....	x
Chapter 1:	1
Introduction	
Chapter 2:	8
“Monolithic gyroidal mesoporous mixed titanium-niobium nitrides”	
Chapter 3:	41
“Mesoporous TiN, $Ti_{1-x}Nb_xN$, and NbN gyroids from block copolymer self-assembly and nitridation”	
Chapter 4:	75
“Block copolymer self-assembly directed synthesis of mesoporous gyroid superconductors”	
Chapter 5:	101
“Gyroidal mesoporous antimony-doped tin oxide from self-assembly of crystalline nanoparticles and a triblock terpolymer”	
Chapter 6:	117
Conclusion	

LIST OF FIGURES

Figure 2.1: Schematic of the synthesis of G ^A metal nitride monoliths.....	12
Figure 2.2: Photographs of freestanding monolithic materials throughout processing	13
Figure 2.3: SAXS patterns of G ^A Ti:Nb 8:2 and 1:1 throughout processing.....	13
Figure 2.4: Powder XRD patterns of Ti:Nb 8:2 and 1:1 G ^A oxides and nitrides.....	15
Figure 2.5: SEM images of G ^A Ti:Nb 8:2 and 1:1 oxides.....	17
Figure 2.6: SEM images of G ^A Ti:Nb 8:2 and 1:1 nitrides.....	17
Figure A2.1: SAXS patterns of G ^A Ti:Nb 8:2 from ISO1 throughout processing.....	27
Figure A2.2: 2D SAXS patterns of G ^A Ti:Nb 8:2 hybrid showing compression.....	28
Figure A2.3: SEM image of G ^A Ti:Nb 8:2 nitride.....	30
Figure A2.4: SEM image of G ^A Ti:Nb 8:2 nitride.....	31
Figure A2.5: SEM image of G ^A Ti:Nb 8:2 nitride.....	32
Figure A2.6: UV-vis-NIR spectra of G ^A Ti:Nb 8:2 oxide and nitride.....	33
Figure A2.7: UV-vis-NIR spectra of G ^A Ti:Nb 1:1 oxide and nitride.....	34
Figure A2.8: UV-vis-NIR spectra of G ^A Ti:Nb 8:2 oxide band gap calculation.....	35
Figure A2.9: UV-vis-NIR spectra of G ^A Ti:Nb 1:1 oxide band gap calculation.....	35
Figure A2.10: Raman spectra of G ^A TiO ₂ and G ^A Ti:Nb 8:2 oxide and nitride.....	37
Figure A2.11: Raman spectra of G ^A TiO ₂ and G ^A Ti:Nb 1:1 oxide and nitride.....	38
Figure 3.1: Schematic of synthesis and processing of G ^A nitrides.....	47
Figure 3.2: Photographs of Ti:Nb = 0 and 1 throughout processing.....	49
Figure 3.3: SAXS patterns for many Ti:Nb compositions of G ^A hybrids, oxides, and nitrides....	50
Figure 3.4: SEM images for many Ti:Nb compositions of G ^A nitrides.....	53
Figure 3.5: XRD patterns for many Ti:Nb compositions of G ^A oxides, and nitrides.....	54
Figure 3.6: XRD patterns comparing G ^A and non-structured TiO ₂ and TiN.....	57
Figure 3.7: Schematic, SAXS patterns, and SEM images comparing G ^A and G ^D NbN.....	60
Figure A3.1: 2D SAXS patterns of G ^A TiO ₂ and TiN	70

Figure A3.2: Plot of lattice parameter vs. Nb content for G ^A nitrides.....	71
Figure A3.3: XRD patterns for G ^A Nb ₂ O ₅ and NbN.....	72
Figure A3.4: XRD patterns for G ^D Nb ₂ O ₅ and NbN.....	72
Figure 4.1: Schematic and photographs of synthesis of superconducting NbN samples.....	79
Figure 4.2: SAXS patterns of ordered mesoporous Nb ₂ O ₅ /NbN throughout processing.....	80
Figure 4.3: SEM images of ordered mesoporous Nb ₂ O ₅ /NbN throughout processing.....	81
Figure 4.4: N ₂ sorption and porosity characterization of ordered mesoporous Nb ₂ O ₅ /NbN.....	82
Figure 4.5: XRD patterns of ordered mesoporous Nb ₂ O ₅ /NbN.....	83
Figure 4.6: Magnetization measurements of superconducting ordered mesoporous NbN.....	85
Figure A4.1: SEM images of collapsed NbN after nitriding at 1050 °C.....	95
Figure A4.2: Field-swept magnetization of superconducting ordered mesoporous NbN.....	96
Figure A4.3: SEM image and FFT of superconducting ordered mesoporous NbN.....	97
Figure A4.4: SEM image and FFT of superconducting ordered mesoporous NbN.....	98
Figure A4.5: SEM image and FFT of superconducting ordered mesoporous NbN.....	99
Figure A4.6: SEM image and FFT of superconducting ordered mesoporous NbN.....	100
Figure 5.1: Schematic of the synthesis of G ^A ATO.....	105
Figure 5.2: Photographs of dried ATO particles and powder of G ^A ATO.....	105
Figure 5.3: SAXS patterns of G ^A ISO/ATO hybrid and freestanding G ^A ATO.....	106
Figure 5.4: XRD patterns of dried ATO particles and powder of G ^A ATO.....	107
Figure 5.5: SEM images of G ^A ATO.....	108

LIST OF TABLES

Table A2.1: Compositions and PDIs of ISO terpolymers.....	26
Table A2.2: d_{100} -spacings for 8:2 Ti:Nb 8:2 and 1:1 hybrids, oxides, and nitrides.....	27
Table A2.3: Electric conductivity measures for Ti:Nb 8:2 nitrides from ISO3.....	29
Table 3.1: Compositions and PDIs of ISO terpolymers.....	48
Table A3.1: Diameters and comparisons of various Ti:Nb hybrid, oxide, and nitrides.....	73
Table A3.2: d_{100} -spacings for various Ti:Nb hybrids, oxides, and nitrides.....	73
Table A3.3: Comparison of shrinkage from photos and SAXS d_{100} -spacings.....	73
Table A3.4: Various Ti:Nb nitride G ^A feature dimensions measured from SEM.....	73
Table A3.5: Crystallite sizes of G ^A TiO ₂ and various Ti:Nb G ^A nitrides.....	74
Table A3.6: d_{100} -spacings of G ^A and G ^D Nb ₂ O ₅ /NbN hybrids, oxides and nitrides.....	74
Table A4.1: Surface areas and pore volumes for ordered mesoporous Nb ₂ O ₅ /NbN.....	95

CHAPTER 1

INTRODUCTION

Overview

The interest and use of mesostructured materials has risen dramatically in recent years.¹ By controlling the dimensions and morphology of materials on the mesoscale (2-50 nm), the properties and performance of devices can be altered. This is particularly true for inorganic materials that are broadly incorporated in devices for their functionality. The three examples from literature show very different mesostructured inorganic systems that show performance enhancements as a result.

In a lithium-sulfur battery system, Ji *et al.* used carbon which was hard templated by mesoporous silica to generate a carbon-sulfur cathode.² They found that mesostructured carbon cathodes dramatically reduced the amount of sulfur dissolved in the electrolyte during cycling compared to non-structured carbon; this results in a comparative capacity increase. He *et al.* deposited Pb into mesoporous silica generate nanowires of the superconducting metal.³ Upon testing the superconducting properties of the nanowires, they observed dramatic increases in the critical field as well as fluctuating increases in the critical temperature. Docampo *et al.* used diblock and triblock terpolymers to mesostructure titanium dioxide in solid-state dye-sensitized solar cells.⁴ They discovered that the solar cells mesostructured from triblock terpolymers showed an increased efficiency compared to solar cells made with the diblock or no block copolymer. These vastly different systems all showed desirable performance enhancements by mesostructuring, despite different materials, applications, and methods of mesostructuring.

Using block copolymers to mesostructure inorganic materials, as in the aforementioned TiO₂ solar cell, is a well-established method of generating highly ordered mesostructures with

tunable morphology and dimensions.⁵⁻⁷ The powerful mesostructuring abilities of block copolymers derive from their thermodynamic self-assembly behavior.⁶

Amphiphilic block copolymers are comprised of chemically distinct polymer chains or “blocks” which are covalently bonded to one another.⁸ The mixing behavior of block copolymers can be described by the free energy of mixing as a function of the degree of polymerization, N , the relative volume fractions of the blocks, as well as the Flory-Huggins interaction parameter, χ , which describes the extent to which the blocks are miscible or immiscible.⁸⁻¹⁰ At sufficiently high values and above (~12) for χN , the blocks will phase separate to minimize their interfacial surface area.^{6, 8} However, the covalent linkage between the blocks prevents macrophase separation and the dimensions of the phase separation are limited to the mesoscale (2-50 nm), which are on the scale of the polymer chain lengths.^{6, 8} The specific morphology that is generated depends on the volume fractions of the blocks and χN .^{6, 8-10} This self-assembly of mesoscale morphologies by block copolymers can be induced by dissolving the polymer in a solvent, and slowly evaporating the solvent away; this process came to be known as evaporation induced self-assembly.¹¹ This processing is used throughout this dissertation to generate self-assembled ordered mesostructures.

The gyroid is a minimal surface which divides space into two equal and opposite networks.¹² In block copolymer self-assembly, gyroids are networked morphologies that are of interest. In diblock copolymer systems, the double gyroid is comprised by the two networks of one block, and the matrix separating the networks of the other block such that the networks never intersect.¹³ In triblock terpolymer systems, the core-shell double gyroid is analogous, where the two networks are one block with a shell of the middle block, and are separated by a matrix of the third block.¹³ Triblock terpolymer systems can also form a unique gyroidal morphology called

the alternating gyroid. In the alternating gyroid structure, there are still two networks separated by a matrix, however, each network is composed of a different endblock, and the matrix is composed of the middle block.¹³ This makes the alternating gyroid particularly interesting as the structure is chiral due to the fact that the inverse networks are comprised of different materials. Furthermore, this structure can be processed to remove the matrix and one network, leaving a single network alternating gyroid structure.¹⁴ Such a bicontinuous single network gyroid is highly porous, with a larger surface area, and is still chiral.¹⁴ This single alternating gyroid morphology is very interesting for applications where diffusion and connectivity are important. The continuous porosity can facilitate diffusion of gases or liquids into the structure while mesoscale dimensions of the network limit solid state diffusion lengths.^{5, 15} The continuity of the network itself allows a continuous pathway, for example electron transfer if the network is an inorganic material.^{5, 15}

To generate ordered mesostructured inorganic materials using BCPs, there are several strategies, including selective block etching and backfilling^{16, 17} and BCP-inorganic coassembly.^{18, 19} In this dissertation, the strategy employed is that of BCP-inorganic coassembly, followed by thermal decomposition of the BCP, yielding freestanding ordered mesoporous inorganic materials. More specifically, sol-gel derived metal oxides can be selectively incorporated into particular blocks of BCPs and this strategy has been used for quite some time in generating ordered mesoporous metal oxides.¹⁹ This is typically achieved through hydrophilic metal oxide particles hydrogen bonding to a hydrophilic block of a BCP such as poly(ethylene oxide).^{5, 6} This strategy allows further tuning of the mesoscale morphology by controlling the amount of oxide added to the BCP since additional oxide content increases the effective volume fraction of the hydrophilic block. To generate ordered mesoporous oxides from these BCP-oxide

composites, some process is used to remove the organic material. These processes can include plasma treatment,¹⁴ direct calcination in air,¹⁹ or inert treatment followed by calcination in air.²⁰

To provide additional functionality, many transition metal oxides can be converted to transition metal nitrides. Transition metal nitrides have many interesting properties, such as electrical conductivity,^{21, 22} chemical stability,^{22, 23} hardness,²¹ wear resistance,²⁴ and low temperature superconductivity.²⁵ By heating many metal oxides under flowing gaseous ammonia (NH_3), they can be converted to their corresponding metal nitride through the solid state diffusional exchange of oxygen and nitrogen.²⁶ This process is driven by the production of water, and thus much be performed with pure anhydrous NH_3 and isolated from ambient: this can be written generally as $\text{MO}_x + (2/3)x\text{NH}_3 \rightarrow \text{MN}_y + x\text{H}_2\text{O} + (x/3 - y/2)\text{N}_2$ where M represents a metal.²⁶ There has been limited exploration into mesoporous nitrides, with the primary examples being dealloying of complex metal nitrides^{27, 28} and BCP-derived carbon-nitride composites.²⁹ This dissertation explores the synthesis and characterization of freestanding BCP-derived ordered mesoporous nitrides, without using a hard template such as a rigid carbon framework.

The development of the synthesis of well-defined ordered mesoporous of metal nitrides opens doors to exploring potentially interesting behavior of mesostructured transition metal nitrides. For example, applications of nitrides such as a non-precious plasmonic materials,³⁰ and superconductivity²⁵ could display novel properties as a function of mesoscale dimensions and morphologies. The dimensional and morphological control of BCP self- and coassembly provide an ideal platform for the exploration of mesostructural effects on various nitride systems and applications. This dissertation sets forth the synthesis, processing, and characterization of well-defined ordered mesoporous transition metal oxide and nitrides that may find use in any number of applications in the future.

Outline of this dissertation

Chapter 1, this section, introduces the general concepts and motivations explored in the dissertation. This includes mesostructuring inorganic materials, block copolymer self-assembly, gyroid structures, and transition metal oxides/nitrides.

Chapter 2 discusses using of block copolymer-inorganic coassembly to generate monolithic gyroidal mesoporous titanium-niobium oxides and nitrides in 8:2 and 1:1: titanium:niobium ratios. Their atomic, mesoscale, and bulk properties are characterized. This chapter sets up the synthesis and characterization for subsequent chapters.

Chapter 3 discusses expanding the synthesis and processing introduced in Chapter 1. More specifically, it explores the binary oxides and nitrides of titanium and niobium in gyroid structures, as well as additional titanium-niobium atomic compositions of the oxides and nitrides. Furthermore, the effects of the mesostructure on nitriding and an additional gyroid structure with a large block copolymer are investigated.

Chapter 4 discusses the use of block copolymer-inorganic coassembly in generating an ordered mesoporous superconductor of NbN. This chapter applies the techniques and pushes the limits of the processing explored in the first two chapters, introducing block copolymer self-assembly as an ideal tool for studying mesostructural effects in superconducting materials.

Chapter 5 discusses an alternate approach using block copolymer-inorganic coassembly to generate crystalline gyroidal oxide structures. Crystalline antimony doped tin oxide nanoparticles are used as building blocks for the gyroidal structure, rather than traditional amorphous sol gel material.

Chapter 6 summarizes the dissertation and presents an outlook.

REFERENCES

1. U.S. Department of Energy Basic Energy Sciences, *From Quanta to the Continuum: Opportunities for Mesoscale Science* **2012**, <http://www.meso2012.com>.
2. Ji, X.; Lee, K. T.; Nazar, L. F. *Nat. Mater.* **2009**, *8*, 500.
3. He, M. *et al.* *ACS Nano* **2013**, *7*, 4187.
4. Docampo, P. *et al.* *Advanced Energy Materials* **2012**, *2*, 676.
5. Orilall, M. C.; Wiesner, U., *Chem. Soc. Rev.* **2011**, *40*, 520.
6. Hoheisel, T. N.; Hur, K.; Wiesner, U. B. *Prog. Polym. Sci.* **2015**, *In Press*.
7. Deng, Y.; Wei, J.; Sun, Z.; Zhao, D. *Chem. Soc. Rev.* **2013**, *42*, 4054.
8. Bates, F. S.; Fredrickson, G. H. *Annu. Rev. Phys. Chem.* **1990**, *41*, 525.
9. Floudas, G. *et al.* *Macromolecules* **2001**, *34*, 2947.
10. Cochran, E. W.; Garcia-Cervera, C. J.; Fredrickson, G. H. *Macromolecules* **2006**, *39*, 2449.
11. Templin, M. *et al.* *Science* **1997**, *278*, 1795.
12. Schoen, A. H., *Infinite Periodic Minimal Surfaces without Self-Intersections*. National Aeronautics and Space Administration: **1970**.
13. Meuler, A. J.; Hillmyer, M. A.; Bates, F. S. *Macromolecules* **2009**, *42*, 7221.
14. Stefkík, M. *et al.* *J. Mater. Chem.* **2012**, *22*, 1078.
15. Rolison, D. R. *et al.* *Chem. Soc. Rev.* **2009**, *38*, 226.
16. Urade, V. N.; Wei, T.-C.; Tate, M. P.; Kowalski, J. D.; Hillhouse, H. W. *Chem. Mater.* **2007**, *19*, 768.
17. Crossland, E. J. W. *et al.* *Nano Lett.* **2008**, *9*, 2807.
18. Jain, A.; Wiesner, U. *Macromolecules* **2004**, *37*, 5665.
19. Yang, P. D.; Zhao, D. Y.; Margolese, D. I.; Chmelka, B. F.; Stucky, G. D. *Chem. Mater.* **1999**, *11*, 2813.
20. Lee, J. *et al.* *Nat. Mater.* **2008**, *7*, 222.

21. Vasu, K.; Krishna, M. G.; Padmanabhan, K. A. *J. Mater. Sci.* **2012**, *47*, 3522.
22. Yang, M.; Van Wassen, A. R.; Guarecuco, R.; Abruña, H. D.; DiSalvo, F. J. *Chem. Commun. (Cambridge, U. K.)* **2013**, *49*, 10853.
23. Cui, Z.; Burns, R. G.; DiSalvo, F. J. *Chem. Mater.* **2013**, *25*, 3782.
24. Sproul, W. D. *Surf. Coat. Technol.* **1996**, *81*, 1.
25. Brauer, G. *Journal of the Less Common Metals* **1960**, *2*, 131.
26. Elder, S. H.; DiSalvo, F. J.; Topor, L.; Navrotsky, A., T *Chem. Mater.* **1993**, *5*, 1545.
27. Yang, M.; MacLeod, M. J.; Tessier, F.; DiSalvo, F. J.; Klein, L. C. *J. Am. Ceram. Soc.* **2012**, *95*, 3084.
28. Yang, M. H.; DiSalvo, F. J. *Chem. Mater.* **2012**, *24*, 4406.
29. Ramasamy, E. *et al. Chem. Mater.* **2012**, *24*, 1575.
30. Naik, G. V. *et al. Optical Materials Express* **2012**, *2*, 478

CHAPTER 2

MONOLITHIC GYROIDAL MESOPOROUS MIXED TITANIUM-NIOBIUM NITRIDES*

Abstract

Mesoporous transition metal nitrides are interesting materials for energy conversion and storage applications due to their conductivity and durability. We present ordered mixed titanium-niobium (8:2, 1:1) nitrides with gyroidal network structures synthesized from triblock terpolymer structure-directed mixed oxides. The materials retain both macroscopic integrity and mesoscale ordering despite heat treatment up to 600 °C, without a rigid carbon framework as a support. Furthermore, the gyroidal lattice parameters were varied by changing polymer molar mass. This synthesis strategy may prove useful in generating a variety of monolithic ordered mesoporous mixed oxides and nitrides for electrode and catalyst materials.

*Reprinted (adapted) with permission from Robbins, S. W.; Sai, H; DiSalvo, F. J.; Gruner, S. M.; Wiesner, U., Monolithic Gyroidal Mesoporous Mixed Titanium–Niobium Nitrides, *ACS Nano* **2014** 8, 8217. Copyright 2014 American Chemical Society.
<http://pubs.acs.org/articlesonrequest/AOR-i7aCkd5svhaViD7mbWKf>

Introduction

Transition metal nitride materials are interesting for a host of applications due to their hardness, thermal/electrical conductivity, chemical stability, and catalytic properties.¹⁻⁴ Furthermore, mixed nitrides often have a combination of useful properties derived from their component nitrides, such as thermal stability and conductivity.³⁻⁵ Transition metal nitrides have been investigated as both catalyst and catalyst support materials in different energy devices, including dye-sensitized solar cells,⁶⁻⁹ fuel cells,¹⁰⁻¹⁴ and batteries.¹⁵ For these energy applications, there is a particular interest in controlled synthetic approaches for monolithic structures that provide three-dimensional (3D) porosity and connectivity with high surface areas and accessibility for the diffusion of fuel, electrolyte, and waste products.^{16, 17}

Previous work has shown the ability to convert porous doped and mixed oxides into their corresponding metal nitrides from inverse opal¹⁸ or dealloyed oxide materials,¹⁹ by heating under flowing ammonia (NH_3) gas. The resulting transition metal nitrides exhibited orders of magnitude higher conductivities than their respective oxides.¹⁸ These materials were either periodically ordered and macroporous or disordered and mesoporous but not both periodically ordered and mesoporous. Furthermore, none of these materials resulted in monoliths.

Gyroid structures are typically comprised of two interpenetrating networks structurally related by an inversion operation and separated by a continuous matrix, thus fulfilling the aforementioned structural criteria. In a double gyroid structure, these two networks are composed of the same material, whereas in an alternating gyroid (G^{A}) they are different materials.²⁰ In triblock terpolymer G^{A} structures, the two networks are made of the two different polymer endblocks while the middle block makes up the matrix separating these networks. If everything but one network in the G^{A} structure is removed, as in this work, the resulting structure is a chiral single gyroidal 3D network.²¹

Block copolymer (BCP) self-assembly has been extensively used for soft templating or structure direction of ordered mesoporous transition metal oxides.²²⁻²⁸ This approach can generate ordered 3D continuous inorganic structures.²⁵ The sole report of a BCP-templated transition metal nitride from an oxide was titanium nitride that was neither a freestanding monolith nor a highly porous 3D continuous network structure.⁸ Furthermore, the retention of a rigid carbon scaffold was required to prevent mesostructural collapse during polymer removal and nitride crystallization.⁸ Retaining the carbon scaffold may not be ideal in energy systems like PEMFCs¹¹ and Li-O₂ batteries.²⁹ We report monolithic gyroidal mesoporous mixed transition metal nitrides. These mesoporous crystalline materials maintain a high degree of both macroscopic integrity and mesoscale order that have not been previously observed for BCP-templated inorganic structures; all of this is accomplished without a rigid carbon support.

In the current work, BCP-templated monolithic 3D networked mixed metal oxides ($Ti_{1-x}Nb_xO_2$), were converted to monolithic 3D networked mixed metal nitrides ($Ti_{1-x}Nb_xN$) by heating under flowing NH₃ gas. The Ti:Nb molar ratios in the oxide sol were 8:2 or 1:1. 8:2 was chosen since Nb can be incorporated into anatase TiO₂ at and above this composition.³⁰ The 1:1 composition was chosen since we have previously investigated mesoporous $Ti_{0.5}Nb_{0.5}N$ as a catalyst support for oxygen reduction.³¹ $Ti_{1-x}Nb_xO_2$ is also a known transparent conducting oxide with various mesoporous morphologies and applications studied.^{30, 32} As detailed in the Methods section, the BCP/oxide hybrids are prepared by the co-assembly of triblock terpolymers and sol-gel derived precursors.²⁵ The poly(isoprene-*b*-styrene-*b*-ethylene oxide) triblock terpolymers are referred to as ISO1, ISO2, and ISO3. Polymer ISO1 had a molar mass of 59,600 g mol⁻¹ and was comprised of 29.7, 62.8, and 7.5 wt% polyisoprene (I), polystyrene (S), and poly(ethylene oxide) (O), respectively, with a polydispersity index of 1.09. Polymer ISO2 had a molar mass of 69,000

g mol^{-1} and was comprised of 29.6, 64.8, and 5.6 wt% I, S, and O, respectively, with a polydispersity index of 1.04. Polymer ISO3 had a molar mass of $63,800 \text{ g mol}^{-1}$ and was comprised of 18.7, 40.5, and 4.6 wt% I, S, and O, respectively, with a polydispersity index of 1.03. The amphiphilic triblock terpolymers, ISO1, ISO2 or ISO3, are dissolved in tetrahydrofuran (THF) and mixed with an aliquot of the hydrophilic oxide sols. Hybrids from ISO1, ISO2, and ISO3 self-assemble into ordered morphologies upon solvent evaporation, a process now referred to as evaporation-induced self-assembly.^{26, 33} The hydrophilic metal oxide sol selectively swells the hydrophilic poly(ethylene oxide) (PEO) block of the BCP. The hydroxyl groups of the oxide sol hydrogen bond to oxygen atoms in the PEO chains. As the solvent is evaporated from the system during film casting, the polymer blocks phase separate on the mesoscale to minimize the interfacial surface area between the blocks, which leads to ordered morphologies.¹⁶ In this work, the PEO block incorporates the metal oxide sol which comprises one network of the alternating gyroid structure after solvent evaporation, shown as the blue network in Figure 2.1. Calcination in air at 450°C removes the BCP templates, sintering the inorganic sol particles, leaving freestanding monolithic mesoporous oxides with a 3D ordered continuous network morphology as shown as the white network in Figure 2.1. These oxides can then be converted to monolithic nitrides with a subsequent heat treatment at 600°C under flowing ammonia shown as the black network in Figure 2.1.

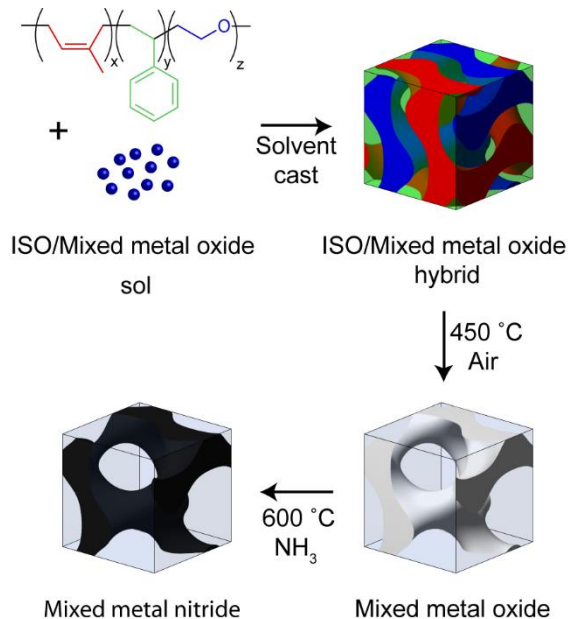


Figure 2.1. Schematic of the process for the generation of ordered mesoporous metal nitride monoliths.

Results and Discussion

Interestingly, as the polymer templates are removed at 450 °C in air, the oxides maintain their macrostructure, despite major shrinkage. In Figure 2.2, the width of the as-made ISO₂ Ti₈Nb₂O₂ hybrid sample (a) is 8.7 mm and the width after conversion to an oxide (b) is 6.8 mm, a difference of 22%. In contrast, there is little change in the width between the oxide (b) and resulting nitride sample (c). In Figure 2.2, the width of the as-made ISO₃ Ti₅Nb₅O₂ hybrid sample (2d) is 14.3 mm and the width after conversion to an oxide (2e) is 11.2 mm, a difference of 22%. After nitriding (2f), the sample width is 10.1 mm, a difference of 10%. The oxides are translucent white, consistent with the removal of polymeric material under these calcination conditions.²⁵ Furthermore, the materials retain their macrostructure after the nitriding process at 600 °C. The resulting monolithic materials are black (c, f), consistent with metal center reduction, yielding the nitrides.

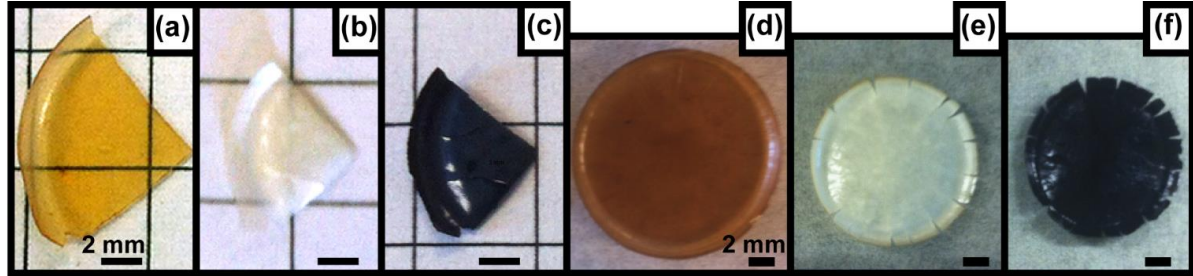


Figure 2.2. Photographs of the freestanding monolithic materials throughout processing. (a) ISO₂/Ti₈Nb₂O₂ hybrid, (b) Ti₈Nb₂O₂, and (c) Ti₈Nb₂N; (d) ISO₃/Ti₅Nb₅O₂ hybrid, (e) Ti₅Nb₅O₂, and (f) Ti₅Nb₅N.

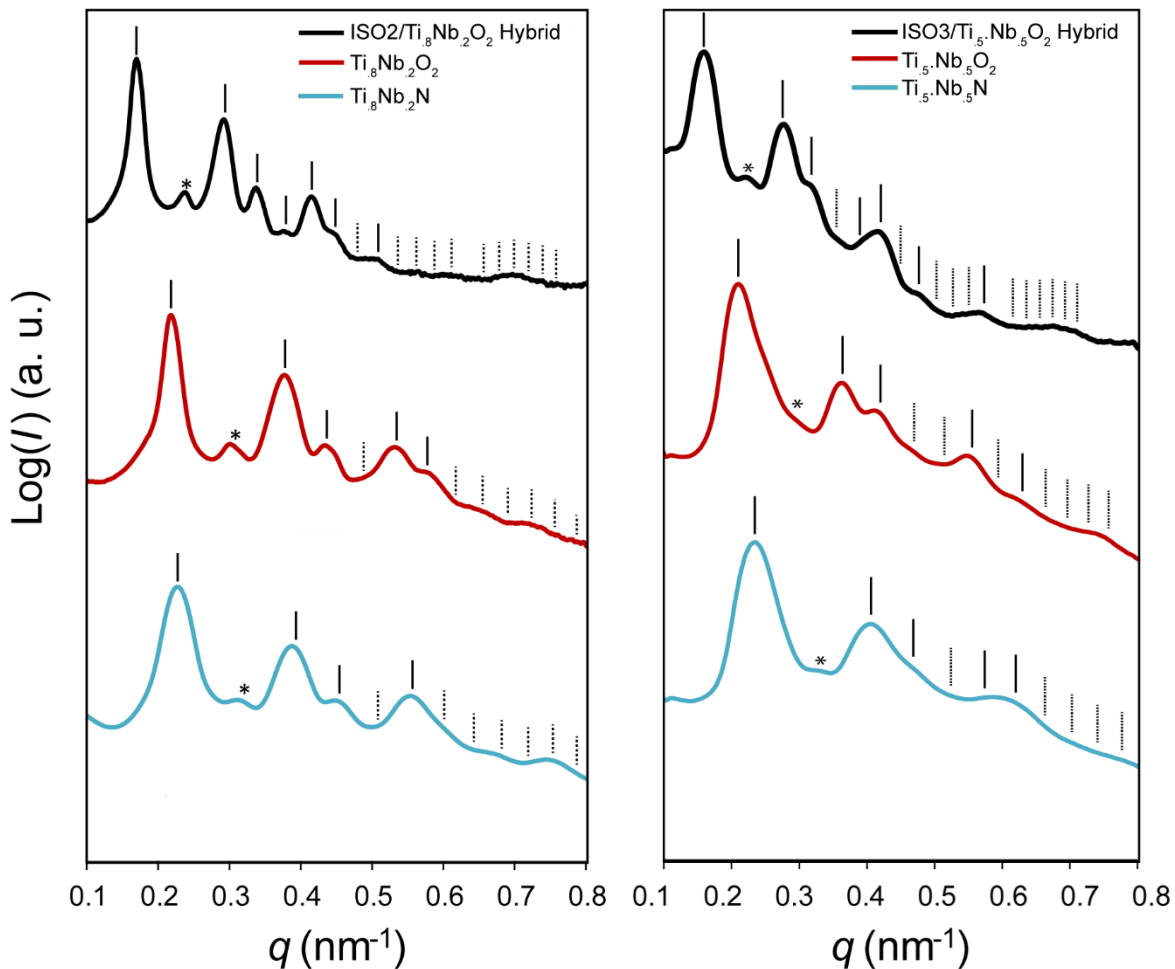


Figure 2.3. Azimuthally integrated small angle X-ray scattering patterns of the ISO₂/Ti₈Nb₂O₂ hybrid (left, top), calcined freestanding Ti₈Nb₂O₂ (left, middle), and freestanding Ti₈Nb₂N (left, bottom); ISO₃/Ti₅Nb₅O₂ hybrid (right, top), calcined freestanding Ti₅Nb₅O₂ (right, middle), and freestanding Ti₅Nb₅N (right, bottom). The vertical lines indicate expected peak positions for the G^A morphology. Dashed lines represent unobserved G^A peaks and asterisks are centered at forbidden $(q/q_{100})^2 = 4$ peak positions that appear due to z-direction compression.

Small angle X-ray scattering (SAXS) was used to measure the mesoscale order of the various ISO1- ISO2- and ISO3-derived samples. The left of Figure 2.3 shows the results for the ISO2/Ti₈Nb₂O₂ system (for SAXS of ISO1/Ti₈Nb₂O₂ see Figure A2.1): ISO2/Ti₈Nb₂O₂ hybrid (left, top), freestanding Ti₈Nb₂O₂ (left, middle), and freestanding Ti₈Nb₂N (left, bottom). The two-dimensional experimental patterns taken with incident X-rays parallel to the film normal (*z*-direction) were azimuthally integrated to yield the one-dimensional patterns shown in the figures. These patterns are consistent with the G^A morphology, except for a forbidden peak at $(q/q_{100})^2 = 4$. This peak is attributed to symmetry breaking from *z*-direction compression during solvent evaporation (see Figure A2.2). This phenomenon has been studied previously in similar BCP/oxide systems.^{25, 34} A systematic shift of the $(q/q_{100})^2 = 6$ peak compared to $(q/q_{100})^2 = 2$ and $(q/q_{100})^2 = 8$ in the nitride is also observed in some samples (see also Figure A2.1). This shift may be due to anisotropic shrinkage of the mesostructure during processing.³⁴ As the sample progresses from a hybrid, to a freestanding oxide, to a freestanding nitride, all peaks shift to higher *q* values and tend to broaden. The shift to higher *q* values correlates to decreases in *d*₁₀₀-spacings (52.4 nm, 40.7 nm, and 39.1 nm for the hybrid, oxide, and nitride, respectively). The hybrid to oxide *d*₁₀₀-spacing shrinkage of 22% is consistent with the 22% macroscopic shrinkage observed upon polymer removal as seen in Figure 2.2. The smaller 4% *d*₁₀₀-spacing shrinkage between the oxide and nitride is consistent with macroscopic size retention. The SAXS patterns of the ISO3/Ti₅Nb₅O₂ system (shown in Figure 2.3, right) displays similar trends to the ISO2/Ti₈Nb₂O₂ system: shifting to higher *q* values and broadening of peaks throughout the processing. The shift to higher *q* values correlates to decreases in *d*₁₀₀-spacings (55.9 nm, 42.3 nm, and 37.9 nm for the hybrid, oxide, and nitride, respectively). For ISO3/Ti₅Nb₅O₂, the hybrid to oxide *d*₁₀₀-spacing shrinkage of 24% is consistent with the 22% macroscopic shrinkage

observed upon polymer removal as seen in Figure 2.2. The smaller 10% d_{100} -spacing shrinkage between the oxide and nitride is also consistent with macroscopic shrinkage of 10%. Remarkably, as indicated by the SAXS patterns, the materials maintain significant long range mesoscale order, despite a total d_{100} -spacing shrinkage of over 25% and heat treatments as high as 600 °C. The d_{100} -spacings of all ISO terpolymer derived materials, including ISO1-derived films (see SI), are summarized in Table A2.2 and demonstrate tailoring of cubic lattice parameters by polymer molar mass and BCP/sol composition.

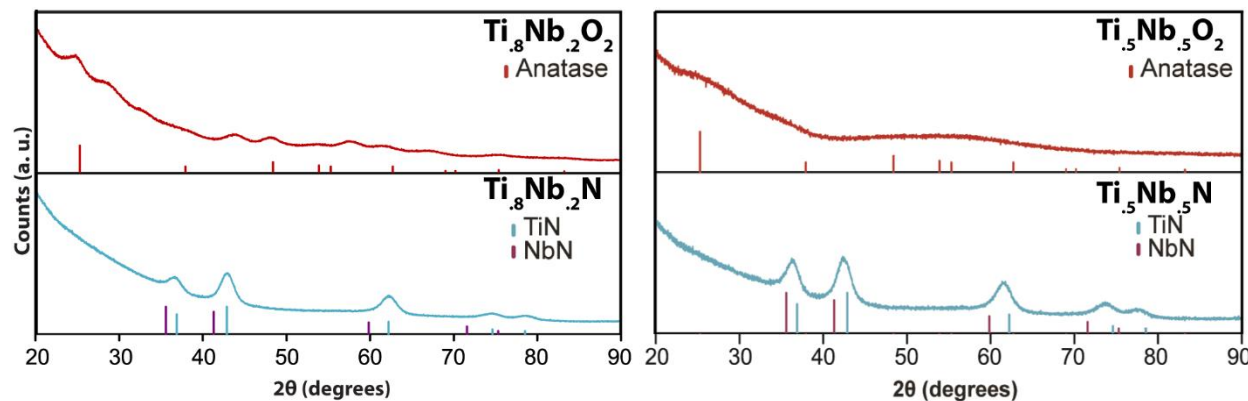


Figure 2.4. Powder X-ray diffraction (XRD) patterns of the ordered mesoporous freestanding $\text{Ti}_{8}\text{Nb}_{2}\text{O}_2$ and $\text{Ti}_{5}\text{Nb}_{5}\text{O}_2$ (top) as well as ordered mesoporous freestanding $\text{Ti}_{8}\text{Nb}_{2}\text{N}$ and $\text{Ti}_{5}\text{Nb}_{5}\text{N}$ (bottom) derived from ISO2/ $\text{Ti}_{8}\text{Nb}_{2}\text{O}_2$ and ISO3/ $\text{Ti}_{5}\text{Nb}_{5}\text{O}_2$ hybrids, respectively. The oxide patterns have peak markings with relative intensities for anatase TiO_2 (PDF Card 00-001-0562). Unindexed peaks for $\text{Ti}_{8}\text{Nb}_{2}\text{O}_2$ are likely due to different $\text{Ti}_{1-x}\text{Nb}_x\text{O}_y$ compositions. The nitrides patterns (bottom) are a cubic rock salt structure, characteristic of many metal nitrides, including TiN and NbN. Peak markings and relative intensities for TiN (blue) (PDF Card 04-015-2441) and NbN (purple) (PDF Card 04-008-5125) are shown.

Powder X-ray diffraction (XRD) measurements were performed on the calcined and nitrided samples from an ISO2/ $\text{Ti}_{8}\text{Nb}_{2}\text{O}_2$ hybrid, as shown in Figure 2.4 (left) and from an ISO3/ $\text{Ti}_{5}\text{Nb}_{5}\text{O}_2$ hybrid, as shown in Figure 2.4 (right). The ISO2/ $\text{Ti}_{8}\text{Nb}_{2}\text{O}_2$ oxide sample calcined at 450 °C in air shows very broad peaks consistent with very small crystallites and predominantly amorphous content (Figure 2.4, top left). Under these calcination conditions, pure titania is crystalline anatase and pure niobia remains fully amorphous.³⁵ It is known, however,

that introducing dopant atoms such as Nb delays the onset of crystallization and anatase-to-rutile transformations in titania^{30, 32}. Some of the weak peaks in the observed oxide pattern match expected anatase TiO₂ peaks but several others do not index with anatase TiO₂, rutile TiO₂, or *T*-Nb₂O₅ and may indicate a mixed composition. The broad peaks with low intensity make definitive microphase identification of the composite material difficult. The corresponding nitrided sample (Figure 2.4, bottom left) shows an XRD pattern exhibiting peaks consistent with the rock salt structure, and intensities consistent with a TiN-rich phase. There appears to be no crystalline oxide present. The crystallite size for the nitride, as calculated by the Scherrer equation, is approximately 4.7 nm, roughly half the diameter of a network strut as seen in SEM (see below). Due to the broadness of the peaks and similar lattice parameters, it is difficult to definitively distinguish between a single phase of Ti_{0.8}Nb_{0.2}N and a mix of the two nitrides, as well as from any amorphous or oxynitride content. The ISO3/Ti_{0.5}Nb_{0.5}O₂ derived oxide sample calcined at 450 °C in air only shows amorphous material due to the higher niobia content (Figure 2.4, top right). The nitrided sample (Figure 2.4, bottom right) also shows an XRD pattern exhibiting peaks consistent with the rock salt structure, with peak positions and intensities consistent with a mixed TiN-NbN. There appears to be no crystalline oxide present. The crystallite size for the nitride, as calculated by the Scherrer equation, is approximately 4.5 nm, roughly half the diameter of a network strut as seen in SEM (see below).

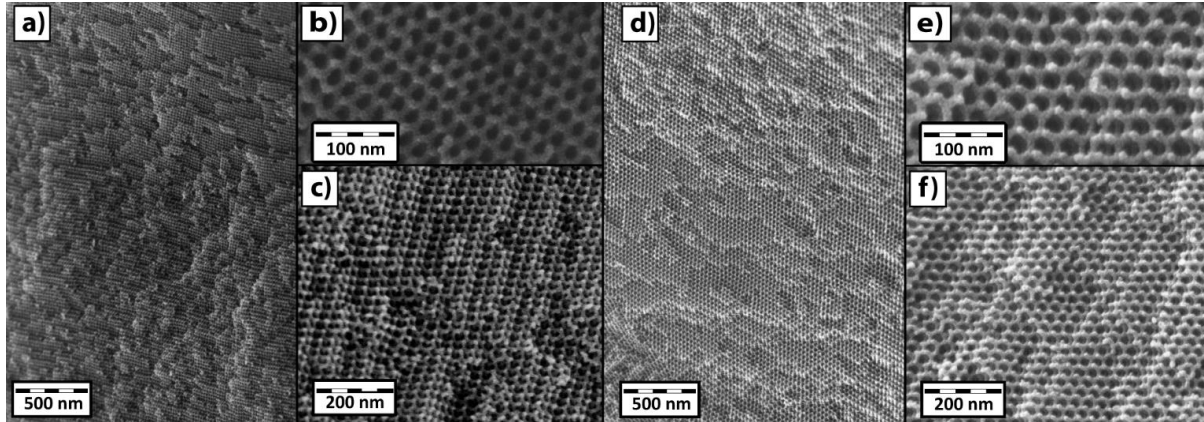


Figure 2.5. Cross-sectional SEM images, at different magnifications, of single domains $> 1 \mu\text{m}$ of Au/Pd coated $\text{Ti}_{8}\text{Nb}_{2}\text{O}_2$ (a, b, c) samples made with ISO2 and $\text{Ti}_{5}\text{Nb}_{5}\text{O}_2$ (d, e, f) samples made with ISO3. The long range order of single domains is shown in (a) and (d), while (b), (c), (e), and (f) reveal the three-dimensionality of the cubic G^{A} structures.

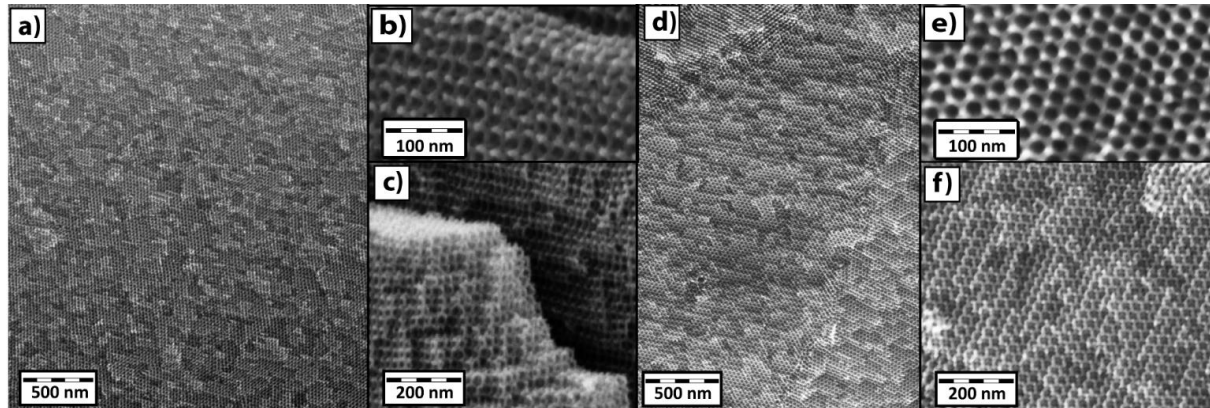


Figure 2.6. Cross-sectional SEM images, at different magnifications, of single domains $> 1 \mu\text{m}$ of uncoated $\text{Ti}_{8}\text{Nb}_{2}\text{N}$ (a, b, c) samples made with ISO2 and $\text{Ti}_{5}\text{Nb}_{5}\text{N}$ (d, e, f) samples made with ISO3. The long range order of a single domain is shown in (a), while (b), (c), (e), and (f) reveal the three-dimensionality of the cubic G^{A} structures.

Cross-sectional scanning electron microscopy (SEM) images (Figs. 2.5 and 2.6) and images in the Appendix (Figure A2.3-A2.5) show the 3D networks of oxide and nitride samples. The oxide sample required coating with Au-Pd for sufficient conductivity for imaging. In contrast, the nitride SEM samples required no conductive coating, indicating electrical conductivity, as expected. The measured feature sizes in $\text{Ti}_{8}\text{Nb}_{2}\text{O}_2$ (Figures 2.5 a-c) sample were about 11 nm strut diameters with 19 nm pores. For $\text{Ti}_{8}\text{Nb}_{2}\text{N}$ (Figures 2.6 a-c) the strut diameter, as measured by SEM, is 9 nm, with pores of 15 nm. The measured feature sizes in the

$\text{Ti}_{1.5}\text{Nb}_{5}\text{O}_2$ sample (Figures 2.5 d-f) were about 10 nm strut diameters with 21 nm pores. For the $\text{Ti}_{1.5}\text{Nb}_{5}\text{N}$ sample (Figures 2.6 d-f) the strut diameter, as measured by SEM, is 9 nm, with pores of 20 nm. While the gyroid structure is the same between the oxides and nitrides (as confirmed by SAXS), the feature sizes are slightly larger for the oxides than in the nitrides, which is consistent with a small difference in SAXS d_{100} -spacings. SEM measurements of the feature sizes are strongly influenced by the projection and orientation of the sample, however, and merely serve as a guide while the SAXS provides a more bulk sampling of the characteristic morphology dimensions. Slight variations between samples may also result in slightly different feature sizes.

Conductivity measurements on monoliths of the nitrides were performed using a two point probe setup. Two $\text{Ti}_{1.8}\text{Nb}_{2}\text{N}$ monoliths showed an average conductivity of 7.3 S/cm and two $\text{Ti}_{1.5}\text{Nb}_{5}\text{N}$ monoliths showed an average conductivity of 3.5 S/cm. The conductivity calculations did not take into account porosity, which lowers the conductivity of the bulk material. Results of additional conductivity characterization, as well as optical characterization (UV-Vis-NIR and Raman spectroscopies) can be found in the SI, revealing more changes of materials properties when moving from the oxides to the nitrides.

It is particularly interesting that, in contrast to syntheses explored previously, the structure retention occurs in these materials without a carbon scaffold that usually prevents collapse of the structure during calcination or crystallization.^{8, 27} The slow ramp rates of the heating procedures (1-2 °C/min) and the nature of the amorphous matrix containing small crystallites in one case, may mitigate the stresses of shrinkage, particularly in the case of the $\text{Ti}_{1.8}\text{Nb}_{2}\text{O}_2$ composition. We speculate the 3D nature of the gyroidal structure and large grain sizes in both compositions may aid mesostructure retention without a hard template.³⁶

Incorporating Nb may prevent macroscopic pulverization by delaying crystallization at the calcination temperature. In addition, the uniform 3D mesoporosity of the structure provides short diffusion lengths on the order of nanometers for the nitriding process, allowing the reaction to occur at 600 °C, mild enough to prevent mesostructure collapse during crystallization.

Conclusions

In summary, by combining self-assembling triblock terpolymers with oxides that are crystalline (titania) and amorphous (niobia) at 450 °C, we generate a mixed oxide, $Ti_{8}Nb_{2}O_2$ with small oxide crystallites in an amorphous oxide matrix as well as an amorphous mixed oxide, $Ti_{5}Nb_{5}O_2$. These materials maintain their macrostructure and mesostructure extremely well upon heat treatment, compared to the BCP-directed component oxides that have been studied.²⁷ These mesoporous mixed oxides can subsequently be nitrided at 600 °C to generate conductive monolithic ordered mesoporous materials for electrode applications. The retention of both the ordered mesostructure and macrostructure during heat treatments, shrinkage, and crystallization opens new possibilities for ordered mesoporous materials. This strategy may be generalized for generating various BCP-directed, ordered mesoporous mixed transition metal oxides and nitrides.

Methods

Materials: Hydrochloric acid (37 wt%, ACS/NF/FCC, Aristar BDH), titanium(IV) isopropoxide (Aldrich, 97%), niobium(V) ethoxide (Aldrich 99.95%, trace metal basis) (for $Ti_{8}Nb_{2}O_2$), niobium(V) ethoxide (Alfa-Aesar 99.999%, metals basis, Ta <500 ppm) (for $Ti_{5}Nb_{5}O_2$), and tetrahydrofuran (Sigma-Aldrich, anhydrous, ≥99.9%, inhibitor-free) were all used as received.

The block copolymers, poly(isoprene-*b*-styrene-*b*-ethylene oxide) (ISO1, ISO2, and ISO3), were synthesized by sequential anionic polymerization. The block copolymer compositions and polydispersity indices (PDI) were characterized by a combination of size exclusion chromatography and nuclear magnetic resonance.

Synthesis of ISO Block Terpolymers: The block terpolymers, poly(isoprene)-*block*-poly(styrene)-*block*-poly(ethylene oxide) were synthesized by sequential anionic polymerization techniques which are described in greater detail elsewhere.^{25, 37, 38} The poly(isoprene) block was initiated by *sec*-butyllithium in benzene, to which the isoprene monomer was added. The styrene monomer was added to the living poly(isoprene) to generate poly(isoprene)-*block*-poly(styrene). The living poly(isoprene)-*block*-poly(styrene) chains were endcapped with ethylene oxide and terminated with methanolic HCl, yielding –OH terminated poly(isoprene)-*block*-poly(styrene). The diblock copolymer was purified using water/chloroform washing and dried on a Schlenk line. The diblock copolymer was then dissolved in tetrahydrofuran and reinitiated with potassium napthalide. The poly(ethylene oxide) block was grown by the addition of ethylene oxide to the initiated diblock copolymer. Finally, the triblock terpolymer poly(isoprene)-*block*-poly(styrene)-*block*-poly(ethylene oxide) was terminated with methanolic HCl, purified by washing, and dried on a Schlenk line. We note that *sec*-butyllithium is a pyrophoric liquid and ethylene oxide is a highly toxic, flammable gas at room temperature. As such, extreme caution should be used with these reagents! Air- and water-free conditions are necessary for the anionic synthesis.

Synthesis of Monolithic Mesoporous Mixed Nitrides: For Ti_{0.8}Nb_{0.2}O₂, 100 mg of either ISO1 or ISO2 was dissolved in 3 mL anhydrous THF to give a 3.5 wt% solution. The mixed oxide sol was prepared by a hydrolytic route, adapted from a previous publication.²⁵ First, 1 mL (3.4 mmol) titanium(IV) isopropoxide was quickly added to 0.38 mL HCl, stirring vigorously in a 20

mL vial. After 2.5 minutes, 0.21 mL (0.8 mmol) niobium(V) ethoxide was quickly added to the stirring vial. After another 2.5 minutes, 2.5 mL (30.8 mmol) anhydrous tetrahydrofuran was quickly added. After 2 minutes, an aliquot of the transparent pale yellow sol was added to the polymer solution. For ISO1 (59.6 kg/mol ISO, 4.5 kg/mol PEO), the sol aliquot was 0.32 mL/100 mg ISO1 to generate a G^A morphology. For ISO2 (69 kg/mol ISO, 3.9 kg/mol PEO), the sol aliquot was 0.34 mL/100 mg ISO2 to generate a G^A morphology, due to its smaller PEO block.

For Ti₅Nb₅O₂, 75 mg of ISO3 was dissolved in 2 mL anhydrous THF to give a 4.0 wt% solution. The mixed oxide sol-gel precursor for Ti₅Nb₅N was also prepared by a hydrolytic sol-gel route. First, 0.90 mL (3 mmol) of titanium(IV) isopropoxide was added to 0.74 mL (3 mmol) of niobium(V) ethoxide in an inert atmosphere glovebox to give a mixed alkoxide precursor. Second, 0.778 g (~0.85 mL) of the mixed alkoxide precursor was quickly added to 0.30 mL HCl and 1 mL anhydrous tetrahydrofuran, stirring vigorously in a 4 mL vial. After 5 minutes, another 1 mL of anhydrous tetrahydrofuran was quickly added to the stirring vial. After 2 minutes, an aliquot of the transparent yellow sol was added to the polymer solution. The sol aliquot was 0.24 mL/75 mg ISO3 to generate a G^A morphology.

The ISO/oxide mixtures were stirred vigorously for at least 3 hours. Films were then cast in PTFE dishes. The solvent was evaporated with the PTFE dish on a glass petri dish covered by a glass dome, on a hot plate set to 50 °C overnight. Films were subsequently aged at 160 °C (Ti₈Nb₂O₂) or 130 °C (Ti₅Nb₅O₂) overnight in a vacuum oven. The highly ordered structure is generated through the slow, controlled evaporation of solvent, leading to large gyroidal domain sizes. The aging process does not appear to play a major role in the generation of large domain ordered mesostructures, but makes the films more robust and less prone to cracking over time.

Films were calcined in air to generate the freestanding oxide in a flow furnace, 3 hours at 450 °C with a ramp rate of 1 °C/min and allowed to cool to ambient.

For nitriding the resulting oxides, the films were heated in a flow furnace under anhydrous ammonia gas at a flow rate of 2.5 L/h for 6 hours at 600 °C, with a ramp rate of 1.6 °C/min (about 100 °C/h). The flow tubes were cooled to room temperature under flowing ammonia, then purged with N₂. One tube valve was opened to air for 30 minutes, then the tube end was removed. Finally, the sample was removed from the tube.

XRD Characterization: Powder X-ray Diffraction (XRD) data for powders of the mixed oxide and mixed nitride were collected on a Rigaku Ultima IV diffractometer equipped with a D/teX Ultra detector, using CuK_α radiation and a scan rate of 2 °/min (Ti_{0.8}Nb_{0.2}O₂) or 5 °/min (Ti_{0.5}Nb_{0.5}O₅).

SAXS Characterization: Small angle X-ray scattering (SAXS) patterns were obtained on a home-built beamline equipped with a Rigaku RU-3HR copper rotating anode generator, a set of orthogonal Franks focusing mirrors and a phosphor-coupled CCD detector, as described elsewhere.³⁹ Some SAXS patterns were also obtained at the G1 station of the Cornell High Energy Synchrotron Source (CHESS), with a beam energy of 10.5 keV and sample-to-detector distance of approximately 2.5 m. The two-dimensional patterns obtained from a point-collimated beam were azimuthally integrated to yield the one-dimensional plots shown in Figures 2.3 and A2.1.

SEM Characterization: Fractured and powdered oxide monoliths were directly mounted on stubs and coated with Au-Pd. Fractured and powdered nitride monoliths were directly mounted on stubs using carbon tape without any coating. Samples were characterized by scanning-

electron microscopy (SEM) on a Zeiss LEO-1550 FE-SEM instrument and a TESCAN MIRA3 LM FE-SEM instrument using in-lens detectors.

Conductivity Characterization: Conductivity of ISO-derived nitride monoliths were measured by a 2-point probe setup. Before calcination, the ISO-derived hybrid films were treated with CF₄ plasma to remove any closed overayers. After calcination and nitriding, monoliths were masked with tape and sputtered with Au/Pd to deposit electrode contacts. On each of these Au/Pd contacts, a drop of liquid metal eutectic Ga/In was placed. The Ga/In eutectic is useful for avoiding direct pressure to the monoliths during measurements which can cause cracking. Resistance measurements were performed across the known cross-section of nitride monolith using a Keithley 2400 SourceMeter. Conductivity values were calculated using the measured resistance and measured sample dimensions of the cross-section.

Acknowledgments

This work was supported as part of the Energy Materials Center at Cornell (EMC2), an Energy Frontier Research Center funded by the U.S. Department of Energy, Office of Science, Basic Energy Sciences under Award No. DESC0001086. This work made use of the Cornell Center for Materials Research Shared Facilities, which are supported through the NSF MRSEC program (DMR-1120296). This work is based upon research conducted at the Cornell High Energy Synchrotron Source (CHESS) which is supported by the National Science Foundation and the National Institutes of Health/National Institute of General Medical Sciences under NSF award DMR-0936384. H.S. was supported by the National Science Foundation (NSF) Single Investigator Award (DMR-1104773). S.W.R. acknowledges K.W. Tan for help in acquiring SEM images, and D.T. Moore for help with UV-vis-NIR measurements.

REFERENCES

1. Marchand, R.; Laurent, Y.; Guyader, J.; L'Haridon, P.; Verdier, P. *J. Eur. Ceram. Soc.* **1991**, *8*, 197.
2. Oyama, S. T. *Catal. Today* **1992**, *15*, 179.
3. DiSalvo, F. J.; Clarke, S. J. *Curr. Opin. Solid State Mater. Sci.* **1996**, *1*, 241.
4. Niewa, R.; DiSalvo, F. J. *Chem. Mater.* **1998**, *10*, 2733.
5. Elder, S. H.; DiSalvo, F. J.; Topor, L.; Navrotsky, A. *Chem. Mater.* **1993**, *5*, 1545.
6. Jiang, Q. W.; Li, G. R.; Gao, X. P. *Chem. Commun.* **2009**, *44*, 6720.
7. Li, G. R.; Wang, F.; Jiang, Q. W.; Gao, X. P.; Shen, P. W. *Angew. Chem. Int. Ed.* **2010**, *49*, 3653.
8. Ramasamy, E. *et al.* *Chem. Mater.* **2012**, *24*, 1575.
9. Xu, H. *et al.* *ACS Appl. Mater. Interfaces* **2012**, *4*, 1087.
10. Ishihara, A. *et al.* *Electrochem. Solid-State Lett.* **2005**, *8*, A201.
11. Zhong, H. X. *et al.* *J. Power Sources* **2007**, *164*, 572.
12. Avasarala, B.; Murray, T.; Li, W.; Haldar, P. *J. Mater. Chem.* **2009**, *19*, 1803.
13. He, P.; Wang, Y. G.; Zhou, H. S. *Chem. Commun.* **2011**, *47*, 10701.
14. Wang, Y. R *et al.* *J. Mater. Chem.* **2012**, *22*, 15549.
15. Dong, S. M. *et al.* *Chem. Commun.* **2011**, *47*, 11291.
16. Orilall, M. C.; Wiesner, U. *Chem. Soc. Rev.* **2011**, *40*, 520.
17. Walcarius, A. *Chem. Soc. Rev.* **2013**, *42*, 4098.
18. Subban, C. V.; Smith, I. C.; DiSalvo, F. J. *Small* **2012**, *8*, 2824.
19. Yang, M.; MacLeod, M. J.; Tessier, F.; DiSalvo, F. J.; Klein, L. C. *J. Am. Ceram. Soc.* **2012**, *95*, 3084.
20. Meuler, A. J.; Hillmyer, M. A.; Bates, F. S. *Macromolecules* **2009**, *42*, 7221.

21. Li, Z. *et al.* *Nat. Commun.* **2014**, *5*, 3247.
22. Yang, P. D.; Zhao, D. Y.; Margolese, D. I.; Chmelka, B. F.; Stucky, G. D. *Chem. Mater.* **1999**, *11*, 2813.
23. Smarsly, B.; Antonietti, M. *Eur. J. Inorg. Chem.* **2006**, *6*, 1111.
24. Ren, Y.; Ma, Z.; Bruce, P. G. *Chem. Soc. Rev.* **2012**, *41*, 4909.
25. Stefik, M. *et al.* *J. Mater. Chem.* **2012**, *22*, 1078.
26. Templin, M. *et al.* *Science* **1997**, *278*, 1795.
27. Lee, J. *et al.* *Nat. Mater.* **2008**, *7*, 222.
28. Bastakoti, B. P. *et al.* *Langmuir* **2014**, *30*, 651.
29. Ottakam Thotiyil, M. M.; Freunberger, S. A.; Peng, Z.; Bruce, P. G. *J. Am. Chem. Soc.* **2012**, *135*, 494.
30. Dros, A. B. *et al.* *Microporous Mesoporous Mater.* **2006**, *94*, 208.
31. Cui, Z.; Burns, R. G.; DiSalvo, F. J. *Chem. Mater.* **2013**, *25*, 3782.
32. Liu, Y. J. *et al.* *ACS Nano* **2010**, *4*, 5373.
33. Brinker, C. J.; Lu, Y. F.; Sellinger, A.; Fan, H. Y. *Adv. Mater.* **1999**, *11*, 579.
34. Toombes, G. E. S. *et al.* *Macromolecules* **2007**, *40*, 8974.
35. Orilall, M. C.; Abrams, N. M.; Lee, J.; DiSalvo, F. J.; Wiesner, U. *J. Am. Chem. Soc.* **2008**, *130*, 8882.
36. Finnefrock, A. C. *et al.* *Angew. Chem. Int. Ed.* **2001**, *40*, 1207.
37. Allgaier, J.; Poppe, A.; Willner, L.; Richter, D. *Macromolecules* **1997**, *30*, 1582.
38. Warren, S. C.; DiSalvo, F. J.; Wiesner, U. *Nat. Mater.* **2007**, *6*, 156.
39. Finnefrock, A. C.; Ulrich, R.; Toombes, G. E. S.; Gruner, S. M.; Wiesner, U. *J. Am. Chem. Soc.* **2003**, *125*, 13084.

APPENDIX 1

Table A2.1. Compositions and polydispersity indices of the three ISO terpolymers.

Component	M _n (kg/mol)	Wt%	Vol%	PDI
ISO1	59.6	-	-	1.09
PI	17.7	29.7%	33.3%	1.09
PS	37.4	62.8%	60.2%	-
PEO	4.5	7.5%	6.5%	-

Component	M _n / (kg/mol)	Wt%	Vol%	PDI
ISO2	69.0	-	-	1.04
PI	20.4	29.6%	33.1%	1.02
PS	44.7	64.8%	62.0%	-
PEO	3.9	5.6%	4.9%	-

Component	M _n / (kg/mol)	Wt%	Vol%	PDI
ISO3	63.8	-	-	1.03
PI	18.7	29.3%	32.8%	1.02
PS	40.5	63.6%	61.0%	-
PEO	4.6	7.1%	6.3%	-

Table A2.2. d_{100} -spacings in nm for ISO1 and ISO2 (8:2 Ti:Nb) and ISO3 (1:1 Ti:Nb)

	ISO1	ISO2	ISO3
Hybrid	48.9	52.4	55.9
Oxide	37.5	40.7	42.3
Nitride	36.1	39.1	37.9

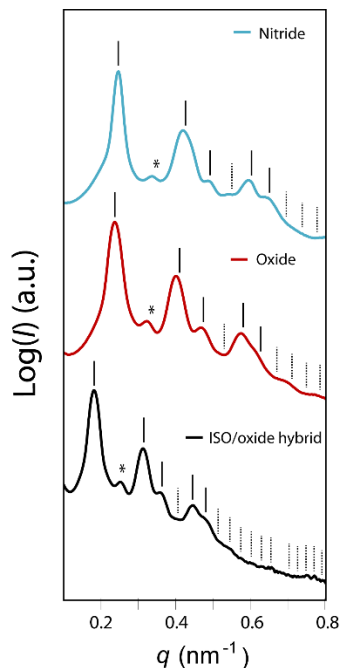


Figure A2.1. Azimuthally integrated small angle X-ray scattering patterns of the ISO1/oxide hybrid (bottom, black), calcined freestanding oxide (middle, red), and freestanding nitride (top, blue). The vertical lines indicate expected peak positions for the G^A morphology. Dotted lines represent unobserved peaks and asterisks are centered at forbidden $(q/q_{100})^2 = 4$ peak positions that appear due to z -direction compression. The d_{100} -spacings of the hybrid, oxide, and nitride are 48.9 nm, 37.5 nm, and 36.1 nm, respectively.

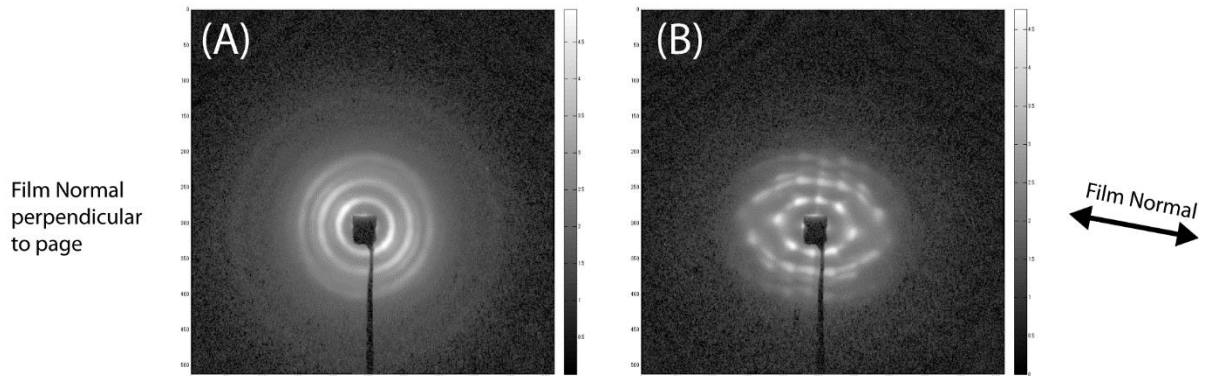


Figure A2.2. 2D SAXS patterns of an ISO2/oxide hybrid with incident X-rays parallel (A) and perpendicular (B) to the film normal. In (B), compression along the film normal direction, as well as clear texturing in the $<110>$ direction parallel to the film normal, is observed.

Additional conductivity measurements:

ISO3 is a third triblock terpolymer with similar molar mass and composition to ISO1 and ISO2 (see Table A2.1) and was used to generate monolithic gyroidal nitrides with similar feature sizes and *d*-spacings as ISO1 and ISO2. These nitride monoliths materials were used for additional conductivity measurements as tabulated below.

ISO3 nitride materials were used to measure both powder and pellet conductivities. Powder conductivity under a pressure 200 psi was measured in an apparatus as described in a previous publication.¹ Pellets were pressed from powders of ground monoliths and pressed into a pellet under a pressure of 9000 psi in a die. The conductivity of the pellet was measured using the 4-point probe setup.

A monolithic nitride sample generated from ISO2 was also used for the four point probe conductivity measurements. The four point probe measurements were performed on a Cascade Microtech CPS-06 using tungsten carbide probe tips and a Keithley 2400 sourcemeter.

Table A2.3. Electrical conductivity measurements from ISO3-derived nitrides

	Conductivity (S/cm)
Monolith	~5.2, ~9.3
Pellet (9000 psi)	~ 6.3×10^{-2}
Powder (200 psi)	~ 7.1×10^{-4}

The monoliths from ISO3 showed similar electrical conductivity to the ISO2 monolith, on the order of 1-10 S/cm. However, the measured powder and pellet conductivities were markedly lower than any of the monoliths. The higher pressure pellet did show higher conductivity than the low pressure powder, as expected. This disparity between monoliths and powders/pellets is likely due to poor particle-particle contact in the powders/pellets. In monoliths, the excellent 3D connectivity provides a continuous path for electrons and avoids the additive contact resistance from each particle-particle contact in the powders or pellets.

Additional Figures:

Not shown here are closed off layers on the top and bottom of the film from bulk casting which have been observed in similar systems previously.²

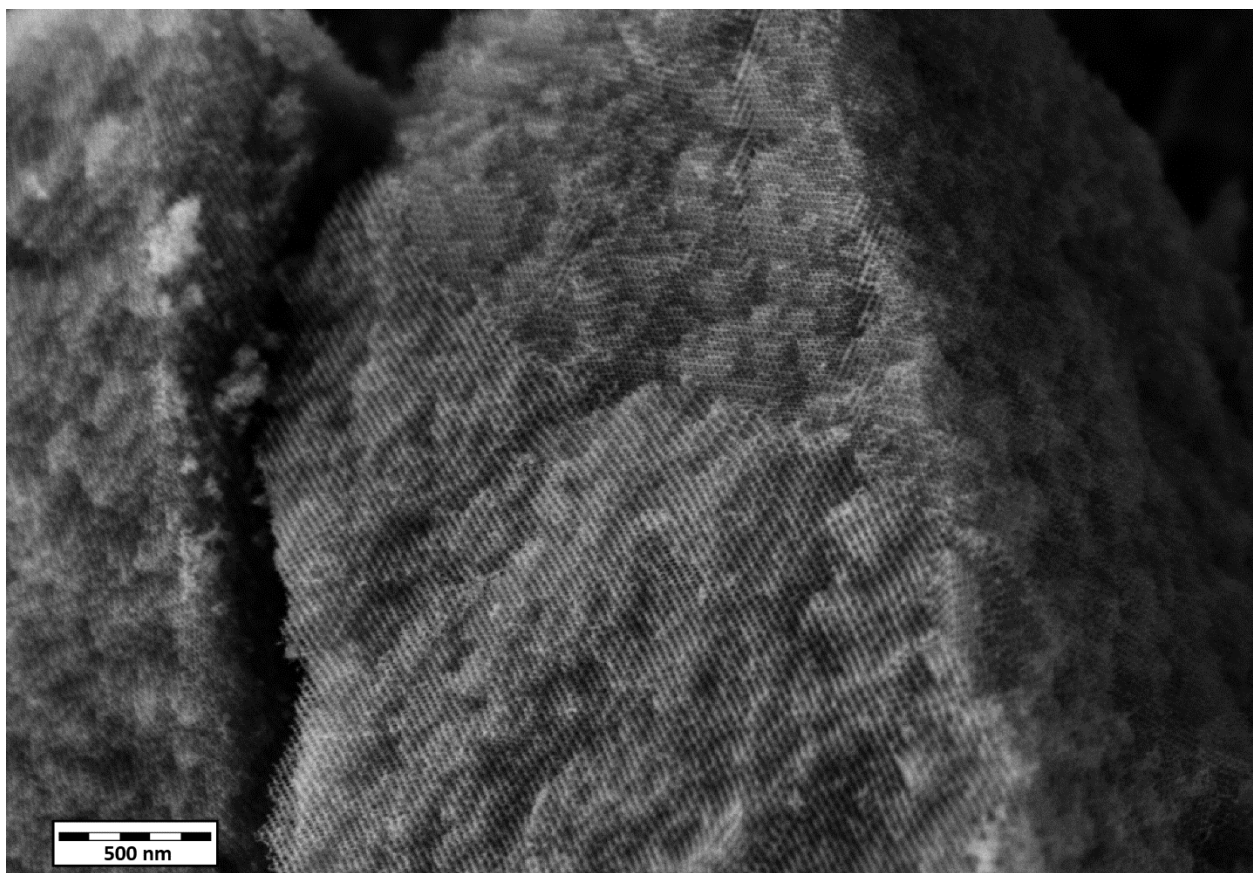


Figure A2.3. SEM image of Ti_{0.8}Nb_{0.2}N from ISO1, showing fracture edges in a powder sample. Several grains of different orientations are evident.

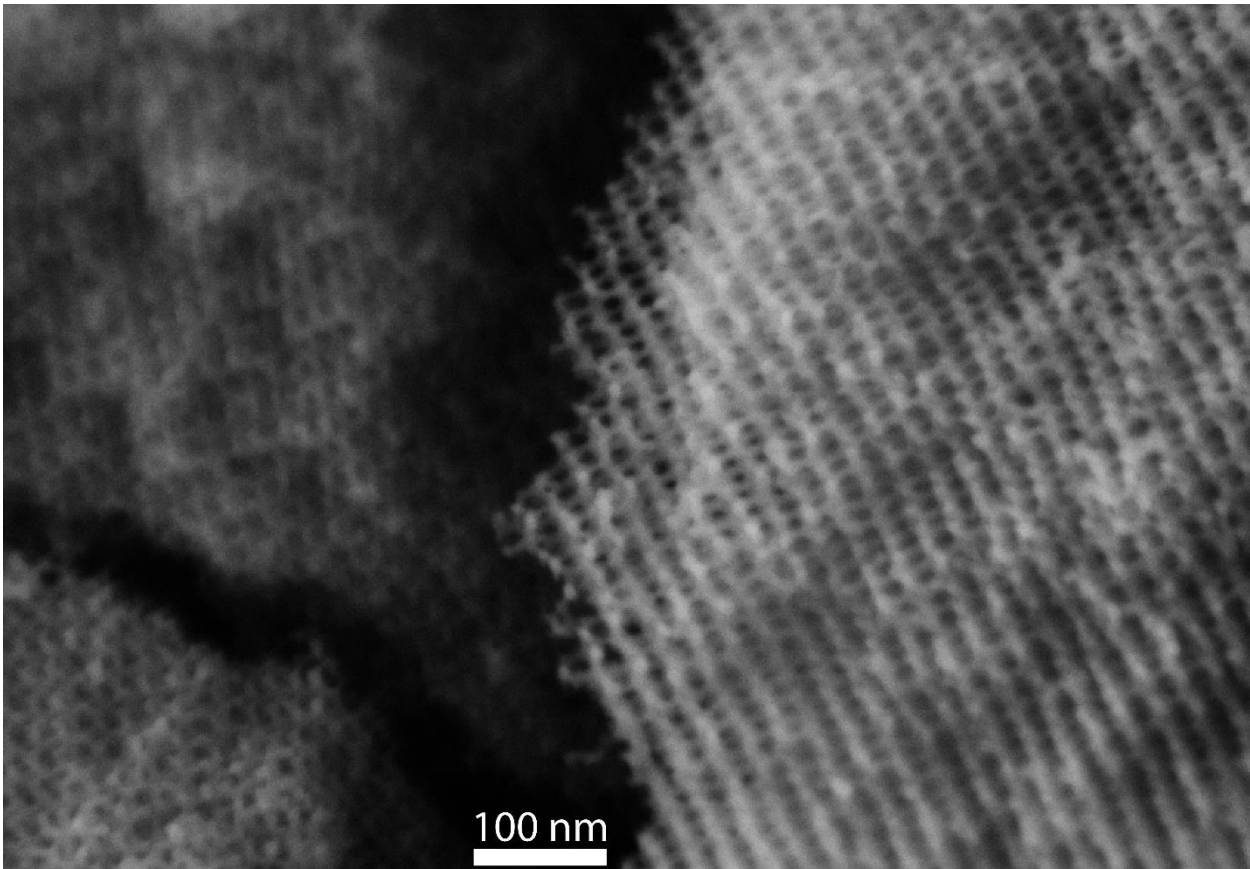


Figure A2.4. SEM image of $\text{Ti}_{0.8}\text{Nb}_{0.2}\text{N}$ from ISO1, showing fracture edges in a powder sample. Multiple layers of struts are evident along the edge.

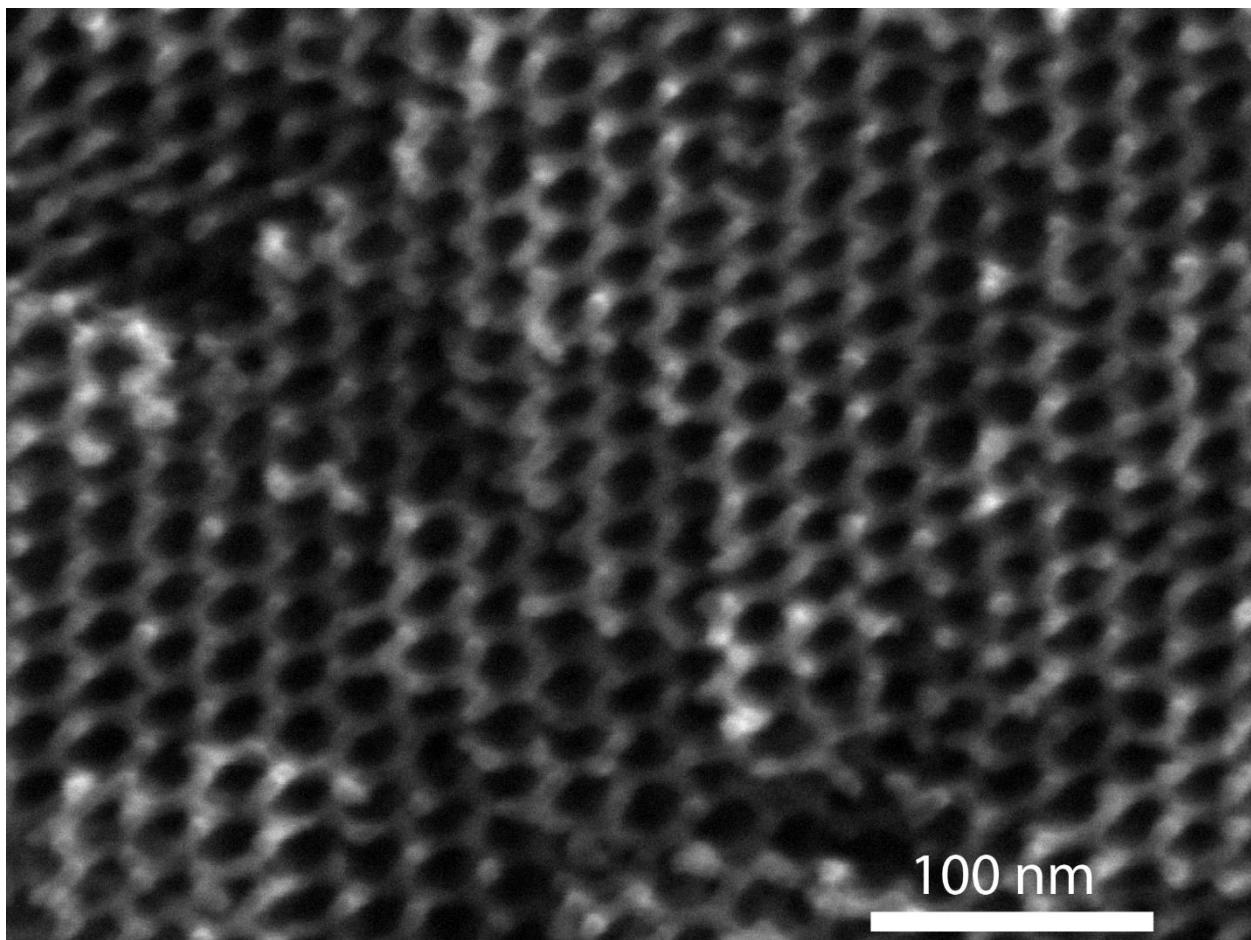


Figure A2.5. SEM image of $\text{Ti}_{0.8}\text{Nb}_{0.2}\text{N}$ from ISO2 showing structures consistent with the G^{A} morphology.

UV-vis-NIR Spectroscopy

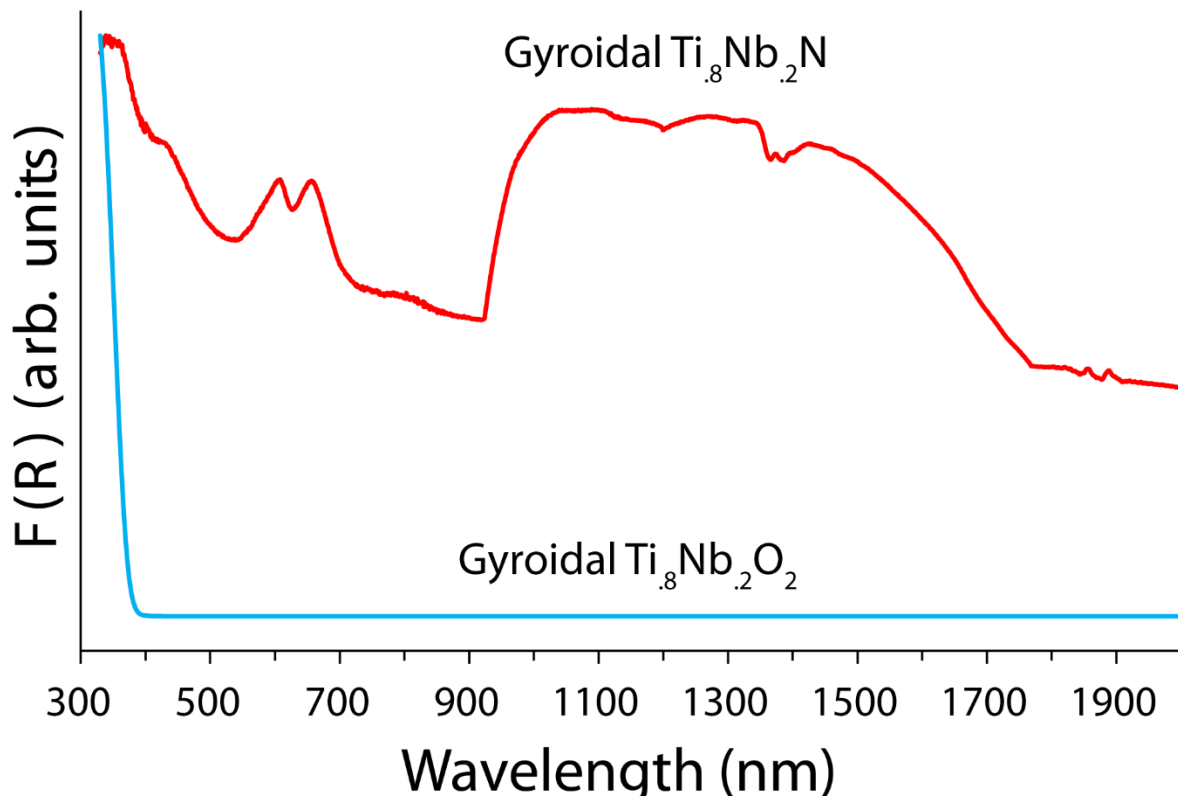


Figure A2.6. Normalized UV-vis-NIR spectra of the Kubelka-Munk function as a function of wavelength for a powdered gyroidal $\text{Ti}_{0.8}\text{Nb}_{0.2}\text{O}_2$ (blue, bottom) and a powdered gyroidal $\text{Ti}_{0.8}\text{Nb}_{0.2}\text{N}$ (red, top). Lamp/grating switchover discontinuities were removed at 1200 nm and 800 nm.

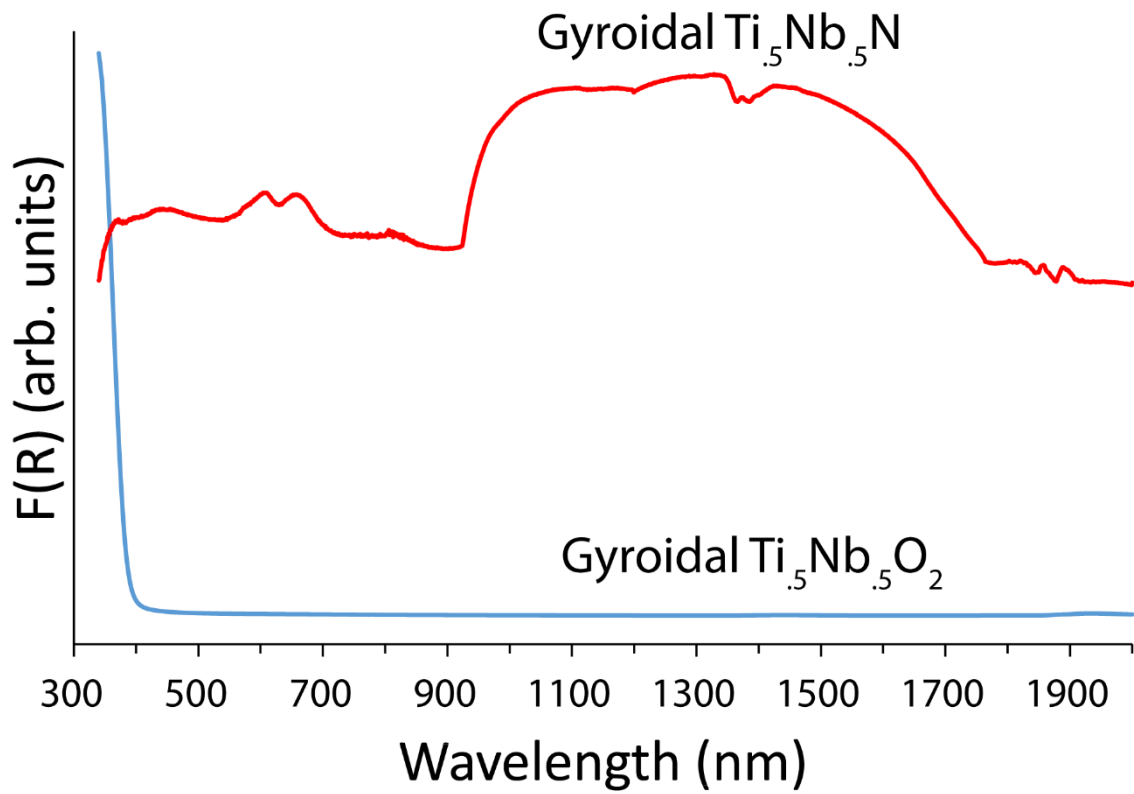


Figure A2.7. Normalized UV-vis-NIR spectra of the Kubelka-Munk function as a function of wavelength for a powdered gyroidal $Ti_{0.5}Nb_{0.5}O_2$ (blue, bottom) and a powdered gyroidal $Ti_{0.5}Nb_{0.5}N$ (red, top). Lamp/grating switchover discontinuities were removed at 1200 nm and 800 nm.

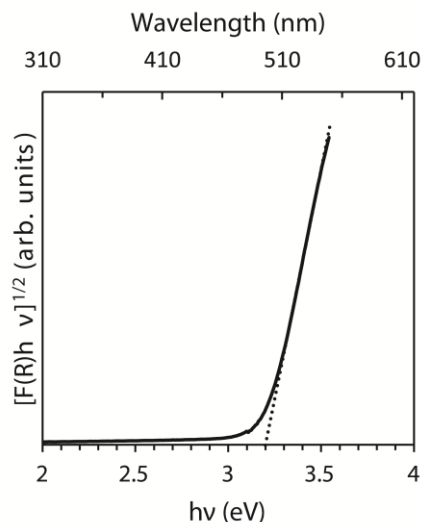


Figure A2.8. $[F(R)hv]^{1/2}$ vs. $h\nu$ plot and linear extrapolation to the x-axis for the powdered gyroidal $Ti_{0.8}Nb_{0.2}O_2$ sample. The x-intercept is at 3.20 eV, estimating the band gap of the oxide.

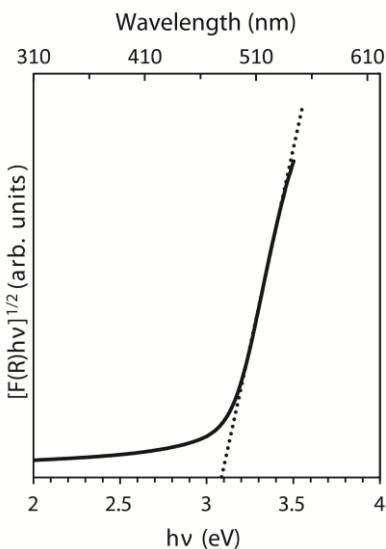


Figure A2.9. $[F(R)hv]^{1/2}$ vs. $h\nu$ plot and linear extrapolation to the x-axis for the powdered gyroidal $Ti_{0.5}Nb_{0.5}O_2$ sample. The x-intercept is at 3.09 eV, estimating the band gap of the oxide.

Powdered gyroidal oxide and nitride samples were characterized by UV-vis-NIR spectroscopy with an integrating sphere accessory on an Agilent Cary 5000 UV-vis-NIR using reflectance mode and is plotted as the Kubelka-Munk function against wavelength.³ The powders were sandwiched between microglass slides for the measurements.

The white colored powder $\text{Ti}_{0.8}\text{Nb}_{0.2}\text{O}_2$ sample showed a characteristic absorption edge around 380 nm as shown in Figure A2.6, (bottom, blue). The band gap was estimated (assuming an indirect optical band gap) to be 3.20 eV by extrapolating the linear region of an $[\text{F}(\text{R})^*\text{hv}]^{1/2}$ vs. hv plot (where $\text{F}(\text{R})$ is the Kubelka-Munk function) to the x-intercept, shown in Figure A2.8.³ This value is in good agreement with reported values of anatase TiO_2 ^{4,5} and $\text{Ti}_{1-x}\text{Nb}_x\text{O}_2$.^{6,7} In comparison, the white colored powder $\text{Ti}_{0.5}\text{Nb}_{0.5}\text{O}_2$ showed a broadened absorption edge, which was not surprising since the material is amorphous. The band gap was estimated (assuming an indirect optical band gap) to be 3.09 eV by extrapolating the linear region of an $[\text{F}(\text{R})^*\text{hv}]^{1/2}$ vs. hv plot (where $\text{F}(\text{R})$ is the Kubelka-Munk function) to the x-intercept, shown in Figure A2.9. The black colored powdered nitride samples showed dramatically different optical behavior (Figures A2.6, A2.7, red). $\text{Ti}_{0.8}\text{Nb}_{0.2}\text{N}$ (Figure A2.6) showed broad absorption across the measured spectrum with some defined features: two peaks around 610 and 665 nm and a significant absorption between 920 and 1700 nm. $\text{Ti}_{0.5}\text{Nb}_{0.5}\text{N}$ (Figure A2.7) showed a similar broad absorption across the measured spectrum with some defined features: two peaks around 620 and 675 nm and a significant absorption between 920 and 1700 nm. The peaks around 620 and 675 are less intense than in $\text{Ti}_{0.8}\text{Nb}_{0.2}\text{N}$ and it also tends to absorb less at shorter wavelengths.

The color change from white wide band gap oxides to black and conducting nitrides is similar to that observed for TiO_2 which was nitrided to yield TiN .⁵ The gyroidal nitride's optical behavior resembles the cubic nitride rather than a N-doped oxide, which is consistent with the XRD results.^{5,8}

Raman Spectroscopy

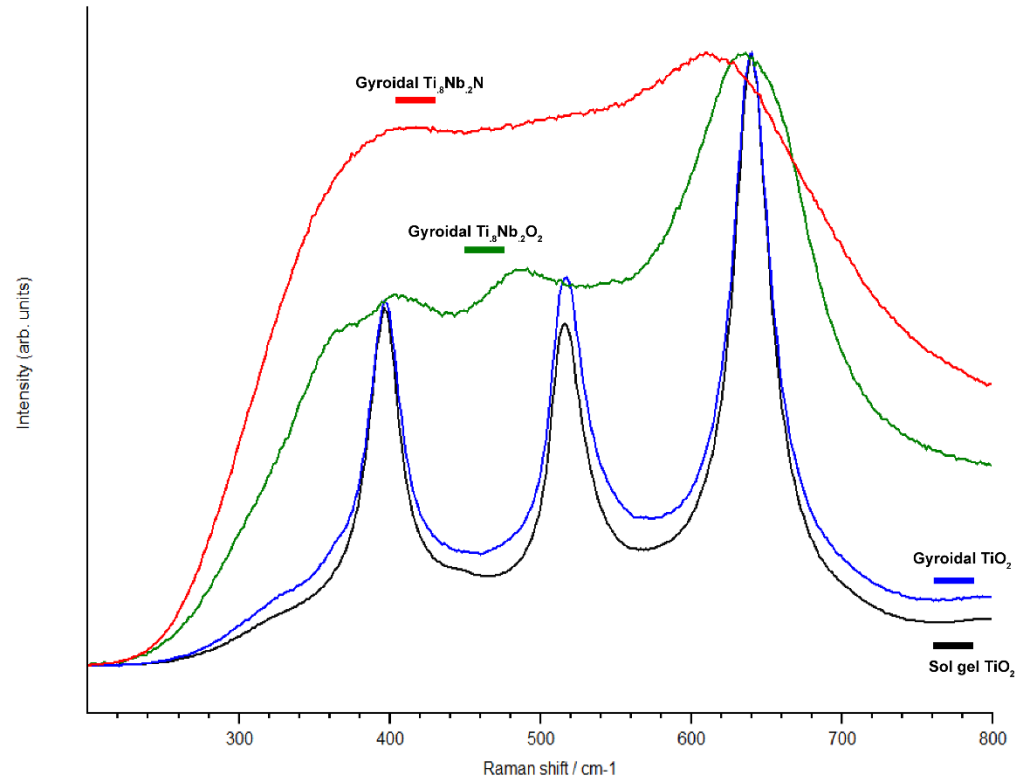


Figure A2.10. Normalized Raman spectra for non-structured TiO₂ (black, bottom), gyroidal TiO₂ (blue), gyroidal Ti_{0.8}Nb_{0.2}O₂ (green), and gyroidal Ti_{0.8}Nb_{0.2}N (red, top).

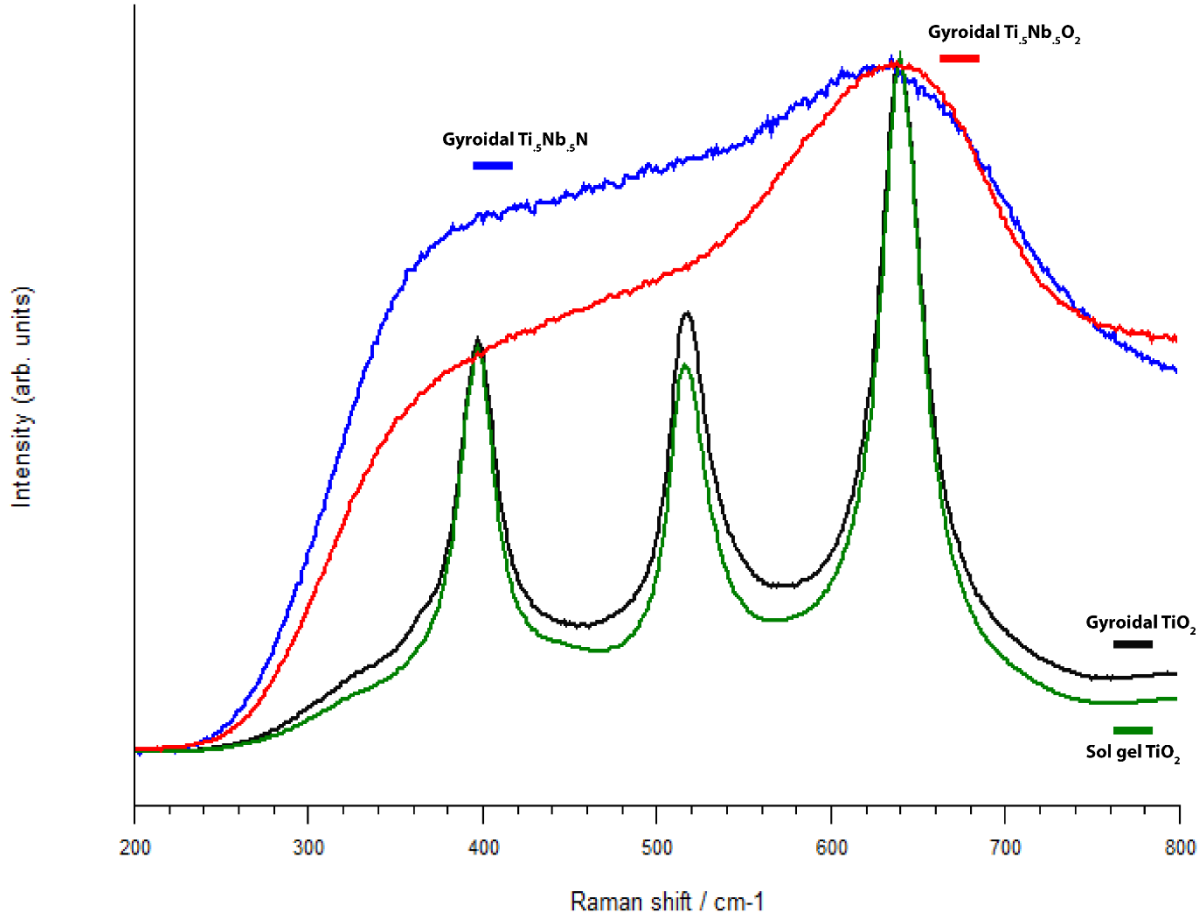


Figure A2.11. Normalized Raman spectra for non-structured TiO₂ (green, bottom), gyroidal TiO₂ (black), gyroidal Ti_{0.5}Nb_{0.5}O₂ (red), and gyroidal Ti_{0.5}Nb_{0.5}N (blue, top).

We performed Raman spectroscopy measurements on the powders of the gyroidal oxide and gyroidal nitride samples on a Renishaw InVia Confocal Raman Microscope using a 488 nm laser and a 50x long working distance objective. The results are displayed in Figures A2.10 and A2.11.

To see the effects of Nb incorporation and nitriding, we first probed non-structured sol-gel derived anatase TiO₂ and gyroidal anatase TiO₂ (both crystalline). These showed strong scattering, as expected for crystalline materials, and are consistent with the well-defined expected bands for anatase.^{6,9}

The gyroidal $\text{Ti}_{0.8}\text{Nb}_{0.2}\text{O}_2$ sample (Figure A2.10) shows broad bands (due to amorphous oxide content), with most prominent anatase band observed around 640 cm^{-1} which is expected for anatase TiO_2 and Nb-doped TiO_2 ⁶ or niobia/titania composites.⁹

The shift of the broad band around 400 cm^{-1} may be due to the incorporation of Nb in the anatase lattice.⁶ However, the broad middle band near 485 cm^{-1} is significantly shifted between expected positions for either anatase or rutile and could not be definitively identified.⁹

The gyroidal $\text{Ti}_{0.5}\text{Nb}_{0.5}\text{O}_2$ sample (Figure A2.11) is amorphous and shows very broad bands, but the strongest band is still around 640 cm^{-1} .

After nitriding, both materials show very broad bands which are consistent with a cubic nitride like TiN or $\text{Ti}_{1-x}\text{Nb}_x\text{N}$ (both cubic rock salt structure), rather than a nitrogen doped TiO_2 or $\text{Ti}_{1-x}\text{Nb}_x\text{O}_2$.⁵ Small grain sizes can also contribute to broad bands.⁹ In cubic binary nitrides, first order scattering is forbidden, so scattering is predominantly derived from impurities and defects, resulting in the observed broad bands.^{5,11,12} We speculate that oxygen⁵ and Nb¹² content can shift the bands in the gyroidal $\text{Ti}_{0.8}\text{Nb}_{0.2}\text{N}$ samples.

REFERENCES

1. Subban, C. V.; Smith, I. C.; DiSalvo, F. J. *Small* **2012**, *8*, 2824.
2. Stefik, M. *et al. J. Mater. Chem.* **2012**, *22*, 1078.
3. Geladi, P.; MacDougall, D.; Martens, H. *Appl. Spectrosc.* **1985**, *39*, 491.
4. Beranek, R.; Kisch, H. *Photochem. Photobiol. Sci.* **2008**, *7*, 40.
5. Zhang, Z. *et al. J. Eur. Ceram. Soc.* **2009**, *29*, 2343.
6. De Trizio, L. *et al. Chem. Mater.* **2013**, *25*, 3383.
7. Hirano, M.; Ichihashi, Y. *J. Mater. Sci.* **2009**, *44*, 6135.
8. Cottineau, T. *et al. J. Mater. Chem. A* **2013**, *1*, 2151.
9. Pittman, R. M.; Bell, A. T., *J. Phys. Chem.* **1993**, *97*, 12178.
10. Barshilia, H. C.; Rajam, K. S. *J. Appl. Phys.* **2005**, *98*, 0143111.
11. Guo, Q. *et al. J. Am. Ceram. Soc.* **2005**, *88*, 249.
12. Vasu, K.; Gopikrishnan, G. M.; Ghanashyam Krishna, M.; Padmanabhan, K. A. *Appl. Phys. A* **2012**, *108*, 993.

CHAPTER 3

MESOPOROUS TiN, $Ti_{1-x}Nb_xN$, AND NbN GYROIDS FROM BLOCK COPOLYMER SELF-ASSEMBLY AND NITRIDATION

Abstract

Mesoporous transition metal oxides and nitrides are of interest for applications including energy conversion and storage. Here we describe binary and ternary oxides and nitrides from titania and niobia structure directed with the help of three triblock terpolymers poly(isoprene)-block-poly(styrene)-block-poly(ethylene oxide) (ISO) of varying molar mass (from 64 to 93 kg/mole) into periodic alternating and double gyroid (G^A , G^D) network morphologies with tunable lattice parameters. Using a combination of scattering and imaging techniques we demonstrate how the macro- and mesostructure of the samples evolves from the as-made hybrids to the heat-treated oxides (450 °C in air) to the final nitrides obtained via heat-treatment to 600 °C under flowing ammonia. Comparison with non-mesostructured oxide and nitride samples elucidates that phase purity of the resulting rock salt nitride structures obtained at the relatively low temperatures are due to small structural dimensions and diffusion lengths as a result of the gyroidal mesostructures. The methods described here may provide access to a range of well-ordered mesostructured binary and ternary oxides and nitrides for model studies of structure-property correlations in materials for applications ranging from energy conversion and storage to catalysis to plasmonics and superconductivity.

* Robbins, S. W.; Sai, H.; Tan, K. W.; Kim, J.-Y.; DiSalvo, F. J.; Gruner, S. M.; Wiesner, U., *In Preparation*.

Introduction

Transition metal oxides and nitrides are interesting classes of materials that can provide a variety of functions. The titanium and niobium oxides and nitrides are some of the most studied of the transition metal oxides and nitrides and they have various useful properties and applications. Titanium dioxide (TiO_2) is well-known for its use in dye-sensitized solar cells¹ and is a known photocatalyst.² Niobium pentoxide (Nb_2O_5) is electrochromic³ and is a promising lithium intercalator for pseudocapacitors.⁴ Titanium nitride (TiN) is used extensively as an abrasion resistant coating for tools⁵ and is also a non-precious plasmonic material.⁶ Niobium nitride (NbN) is best known as a low temperature superconductor.⁷ Titanium and niobium can also form ternary oxides⁸⁻¹⁰ and ternary nitrides¹¹⁻¹³ and their atomic composition can be tuned to influence their physical properties. In $\text{Ti}_{1-x}\text{Nb}_x\text{O}_2$, a transparent conducting oxide, the Ti:Nb ratio can be used to tune its electrical conductivity^{9,10} and optical properties.¹⁰ Similarly, controlling the atomic composition of $\text{Ti}_{1-x}\text{Nb}_x\text{N}$ can tune its electrical conductivity,^{12,13} corrosion stability,^{11,12} hardness,¹³ and optical properties.¹³

Introducing ordered mesoporosity into oxide and nitride systems can affect their properties and performance through various mechanisms. For example, ordered porosity in superconductors can influence vortex pinning¹⁴; in batteries, ordered mesoporosity can provide continuous pathways for electrons or electrolyte while also minimizing solid state diffusion lengths of ions.^{15,16} By exerting control over both atomic composition and mesostructural features of ternary transition metal nitrides, one can tune the properties and performance of the material for a desired application. While there has been extensive research and progress on generating ordered mesoporous transition metal oxides,¹⁷ far less studies exist on ordered mesoporous nitrides.

Block copolymers (BCPs) can undergo microphase separation which serves as a tool for generating ordered mesoporosity in inorganic materials. By controlling the BCP molar mass and volume fractions, one can generate a variety of complex and interesting mesoscale morphologies with specific dimensions.¹⁸ In triblock terpolymers systems, the alternating gyroid (G^A) and core-shell double gyroid (G^D) can be generated.¹⁹ Both gyroid structures contain two interpenetrating networks separated by one or more domains. In the G^A , the two different BCP endblocks make up the two networks, and they are separated by a matrix of the middle block. In the G^D , the two networks are comprised of one of the endblocks, are encased in a shell of the middle block, and are separated by a matrix of the other endblock. Hydrophilic metal oxide precursors can be selectively incorporated into one of the BCP domains and can ultimately yield gyroidal metal oxides after BCP removal.^{20,21} By heating under flowing ammonia gas, these gyroidal oxides can be converted into gyroidal metal nitrides.²¹ Gyroidal mesoporous materials are particularly interesting due to their large surface areas, continuous three-dimensional porosity, and mesoscale inorganic dimensions which can provide the beneficial effects of ordered mesoporosity discussed above. These properties are particularly relevant in the systems in this work due to the necessity of both gas diffusion in/out of the mesoporous structure as well as solid state diffusion of atoms in/out of the inorganic structure during the nitriding process.

We have previously shown the retention of the macroscopic integrity and ordered mesostructure in gyroidal $Ti_{0.8}Nb_{0.2}O_2/Ti_{0.8}Nb_{0.2}N$ and $Ti_{0.5}Nb_{0.5}O_2/Ti_{0.5}Nb_{0.5}N$ systems, despite major shrinkage of the materials, as well as the crystallization of the nitrides without rigid carbon supports.²¹ Here, we show the macroscopic integrity, mesoscale ordering, and atomic crystal behavior of gyroidal binary oxides TiO_2 and Nb_2O_5 , their corresponding gyroidal binary nitrides TiN and NbN , as well as a range of gyroidal mixed compositions of $Ti_{1-x}Nb_xO_2$ and their

conversion to nitrides. In particular, we demonstrate a crystalline-to-crystalline oxide-to-nitride (TiO_2 -to-TiN) conversion, an amorphous-to-crystalline oxide-to-nitride (Nb_2O_5 -to-NbN) conversion, and the intermediate mixed composition oxides' conversions ($\text{Ti}_{1-x}\text{Nb}_x\text{O}_2$ -to- $\text{Ti}_{1-x}\text{Nb}_x\text{N}$) to nitrides. We provide support that the gyroidal structure facilitates the conversion of oxides to nitrides by comparing results to a non-mesostructured oxide. Finally, we use a larger BCP and change the BCP:oxide ratio to generate highly ordered oxides and nitrides with a second gyroidal mesostructure, demonstrating further mesostructural control.

Experimental

Materials: Hydrochloric acid (37 wt%, ACS/NF/FCC, Aristar BDH), titanium(IV) isopropoxide (Aldrich, 97%), niobium(V) ethoxide (Alfa-Aesar 99.999%, metals basis, Ta <500 ppm), and tetrahydrofuran (THF) (Sigma-Aldrich, anhydrous, ≥99.9%, inhibitor-free). All reagents were used as received.

ISO Block Terpolymers: The poly(isoprene)-*block*-poly(styrene)-*block*-poly(ethylene oxide) (ISO) block terpolymers were synthesized by sequential anionic polymerization. The specific experimental techniques employed have been described extensively in the literature.²⁰⁻²⁴ The block terpolymers were characterized by size exclusion chromatography and proton nuclear magnetic resonance and their compositions and polydispersity indices are shown in Table 3.1.

Synthesis of Gyroidal Mesoporous Transition Metal Nitrides: All gyroidal mesoporous transition metal nitrides were synthesized by incorporating hydrolytic oxide sol-gel materials with an ISO block terpolymer. An aliquot of the oxide sol-gel material was added to a solution of ISO in an organic solvent (THF) and an ordered gyroidal BCP/oxide hybrid was obtained by evaporation of the solvent. The BCP/oxide hybrids were then calcined in air at 450 °C to yield gyroidal transition metal oxide materials. Finally, the gyroidal oxides were nitrided at 600 °C in NH_3 to

yield the final gyroidal transition metal nitrides. The differences in ISO compositions and size, as well as density differences of the oxides are the reasons for the different sol loadings and precursor amounts, and all were intended to provide similar final d_{100} -spacings for the final nitride G^A structures, as demonstrated in the SAXS section. We note that the HCl is concentrated and caustic and that the transition metal alkoxide precursors are very reactive with moisture and the water in the HCl. PTFE septum-capped vials and careful handling are recommended for the following procedures.

ISO/Oxide Hybrids: In general, all compositions were generated with a similar procedure, modified from previous publications.^{20,21} Detailed syntheses descriptions for each type of sample can be found in the Supporting Information. An amount of ISO was first dissolved in THF. Then, in a separate vial, to generate a pure or mixed metal oxide sol, either a single metal alkoxide or a mixture of metal alkoxides (respectively) was added to either HCl or HCl diluted with THF (respectively), and was stirred for 5 minutes. Next, THF was added to the vial and it was stirred for another 2 minutes. An aliquot of the oxide sol was added to the ISO/THF solution, and was stirred at least 3 hours. Subsequently, the ISO/oxide/THF solution was placed into a PTFE dish on a crystallization dish that was covered with a hemispherical glass dome, and was put on a hot plate set to 50 °C. The solvent was allowed to slowly evaporate overnight which yielded the ISO/oxide hybrid film. The film in the PTFE dish was transferred into a vacuum oven and held at 130 °C for at least 3 hours under vacuum. We have found that this aging process helps minimize cracking of the films over time.²¹

Gyroidal Mesoporous Oxides: The aforementioned BCP/oxide hybrids were all subjected to the same procedure to generate gyroidal mesoporous oxides. The BCP/oxide hybrid film was placed in a combustion boat inside an unsealed tube furnace, exposed to atmosphere. The furnace was

ramped to 450 °C at a rate of 1 °C/min and held for 3 hours at 450 °C. This procedure removed the BCP and sintered the oxide material, which yielded the gyroidal mesoporous oxide sample.

Gyroidal Mesoporous Nitrides: The aforementioned gyroidal mesoporous oxides were all subjected to the same nitridation treatment to generate gyroidal mesoporous nitrides. The gyroidal mesoporous oxides were placed in a combustion boat and loaded into a quartz tube which was placed in a tube (flow) furnace. The quartz tube was connected with stainless steel endpieces to purified anhydrous ammonia (NH₃) at the inlet and a mineral oil bubbler at the outlet. Anhydrous NH₃ was flowed through the tube at a rate of 2.5 L/h. The furnace was ramped to 600 °C at a rate of 1.6 °C/min (~100 °C/h) and held for 6 hours at 600 °C. The furnace was allowed to cool under flowing NH₃ and the tube was purged with N₂ to remove residual NH₃ gas. One end-piece was removed for 30 minutes to gradually expose the sample to air and then the nitride sample was removed for characterization.

XRD Characterization: Powder X-ray Diffraction (XRD) was measured for powdered samples of the various oxide and nitride samples. The samples were measured on a Rigaku Ultima IV diffractometer with a D/teX Ultra detector using Cu K α radiation and a scan rate of 5 °/min.

SAXS Characterization: Small angle X-ray scattering (SAXS) patterns were collected either at the G1 station of the Cornell High Energy Synchrotron Source (CHESS) with a typical beam energy of 10.5 keV and sample-to-detector distance of 2.6 m or on a home-built beamline with a Rigaku RU-3HR Cu rotating anode, a set of orthogonal Franks focusing mirrors and a phosphor coupled CCD detector, detailed previously.²⁵ Two-dimensional patterns were azimuthally integrated, yielding the one-dimensional plots seen in Figures 3.3 and 3.7.

SEM Characterization: Fractured nitride monoliths were mounted on stubs for scanning electron microscopy (SEM) imaging and required the addition of no conductive coating for imaging.

Zeiss LEO-1550 FE-SEM and TESCAN MIRA3 LM FE-SEM instruments using in-lens detectors were used to perform the SEM imaging.

Results and Discussion

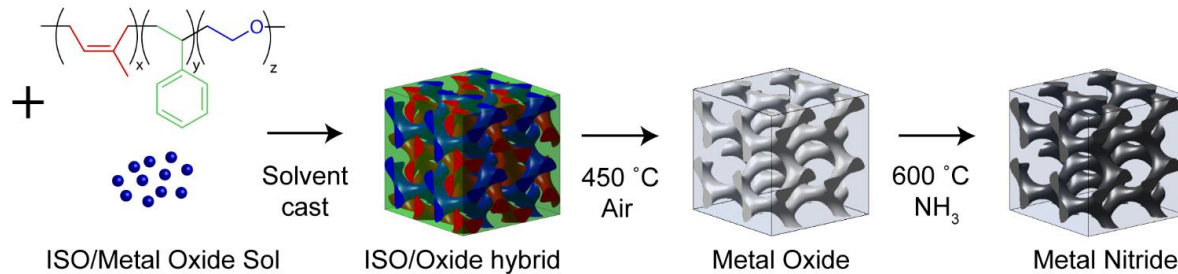


Figure 3.1. Schematic of the synthesis and processing for the various gyroidal metal oxides and gyroidal metal nitrides. The structure shown is the alternating gyroid (G^A) structure.

In order to synthesize freestanding gyroidal mesoporous oxides and nitrides, we used hydrolytic sol-gel chemistry for oxide precursor in combination with amphiphilic block terpolymers, poly(isoprene)-*block*-poly(styrene)-*block*-poly(ethylene oxide) (ISO) as structure-directing agents. The subsequently described processing is shown schematically in Figure 3.1. When the BCP is dissolved in tetrahydrofuran (THF) and mixed with the oxide sol, the hydrophilic sol nanoparticles hydrogen bond to the hydrophilic poly(ethylene oxide) (PEO) block. The solvent is then evaporated, allowing the block copolymer and oxide nanoparticles to self-assemble into an ordered mesoscale morphology.^{26,27} The oxide is incorporated into the PEO domain of the mesostructure, shown as the blue domains of the alternating gyroid in Figure 3.1. The polymer can subsequently be removed by calcination in air at 450 °C, leaving a freestanding gyroidal oxide behind, shown as the white network in Figure 3.1. This gyroidal oxide can subsequently be heated at 600 °C under flowing ammonia gas (NH₃) to convert it to a freestanding gyroidal nitride (shown as the black network in Figure 3.1), without collapse of the macro- or mesostructure. Three ISO block terpolymers were used as structure-directing agents:

ISO-64, ISO-69, and ISO-93 where the numbers denote the number-average total molar mass of the block terpolymers in kg mol⁻¹. The BCP compositions and corresponding polydispersity indices (PDIs) are compiled in Table 3.1.

Table 3.1. Compositions and polydispersity indices (PDIs) for the ISO block terpolymers used in this work.

	PI mol ⁻¹)	PS mol ⁻¹)	PEO mol ⁻¹)	PI (vol%)	PS (vol%)	PEO (vol%)	PDI
ISO-64	18.7	40.5	4.6	32.8	61.0	6.2	1.03
ISO-69	20.4	44.7	3.9	33.1	62.0	4.9	1.04
ISO-93	29.0	58.3	6.1	34.2	60.1	5.7	1.06

We used various oxide atomic compositions to generate gyroidal structures by varying the relative content of the titanium oxide and niobium oxide sol-gel precursors (titanium(IV) isopropoxide and niobium(V) ethoxide). The amounts of oxide sol added to the BCPs were designed to generate gyroidal morphologies with similar *d*-spacings for the resulting G^A nitride structures. ISO-64 and ISO-69 were used interchangeably for the various Ti:Nb compositions of G^A structures. ISO-93 was used for generating both G^A and G^D structures of Nb₂O₅/NbN by varying the BCP:oxide ratio. The differences in oxide loadings between ISO-64, ISO-69, and ISO-93 are noted in the additional experimental section in the SI.

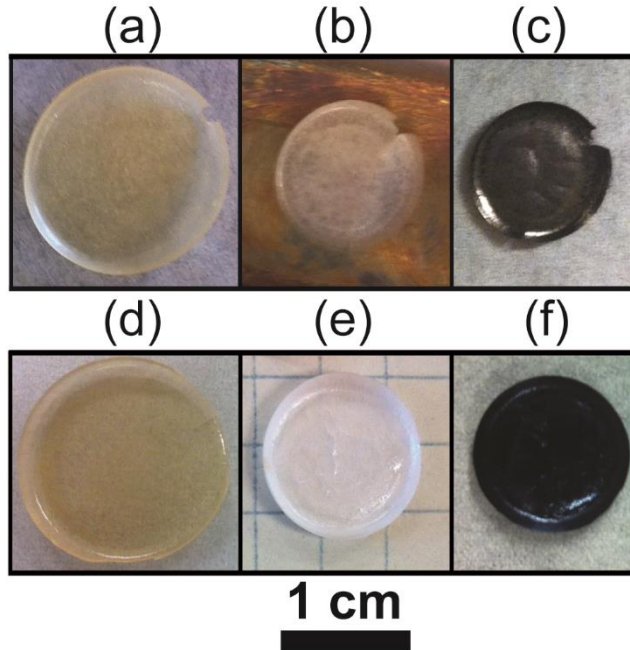


Figure 3.2. Photographs of two different atomic compositions at the different stages of processing. (a) ISO/Nb₂O₅ hybrid, (b) Nb₂O₅, (c) NbN; (d) ISO/TiO₂ hybrid*, (e) TiO₂, (f) TiN. *We note that the ISO/TiO₂ hybrid shown in (f) is from a different sample than (e) and (f).

Figure 3.2 shows photos of samples of the two binary nitrides studied here (i.e. with different atomic compositions of [Nb]/[Ti + Nb] = 0.0 and 1.0) as they progressed through the heat treatments: ISO/oxide hybrids after film casting and aging (Figure 3.2a,d), freestanding oxides (Figure 3.2b,e), and freestanding nitrides (Figure 3.2c,f). We note that the ISO/TiO₂ hybrid shown in Figure 3.2d is from a different sample as the oxide (Figure 3.2e) and nitride (Figure 3.2f). Completely intact films like those in Figure 3.2 were not always achieved but the samples still retained macroscopic dimensions and did not pulverize to powders. We have previously observed the macroscopic retention throughout the calcination and nitriding in ISO/Ti_{0.8}Nb_{0.2}O₂ and ISO/Ti_{0.5}Nb_{0.5}O₂ systems.²¹ The dimensions of the binary oxide and nitride samples in Figure 3.2 and their comparisons to the parent hybrids are compiled in Table A3.1. These values are later compared to the shrinkage of the cubic mesoscale *d*-spacings as measured

by small angle X-ray scattering (SAXS), *vide infra*. Any cracks tend to form during the film casting which are exacerbated during the heat processing. The samples shown in Figure 3.2 represent the best cases for macrostructure retention we have observed. After calcination, the highly porous films are quite fragile. However, an aging procedure at 130 °C in a vacuum oven after the solvent casting seems to mitigate cracking of the ISO/oxide hybrids. Nevertheless, it is remarkable that multiple atomic compositions of freestanding highly porous oxides and nitrides maintain their macrostructure, even as they are exposed to temperatures as high as 600 °C, undergo major macroscopic shrinkage, as well as other mesoscopic and atomic transitions which are further discussed below. With a broad range of atomic compositions retaining their macroscopic integrity, we attribute this property to the processing conditions and the gyroidal mesostructure rather than to the atomic composition.

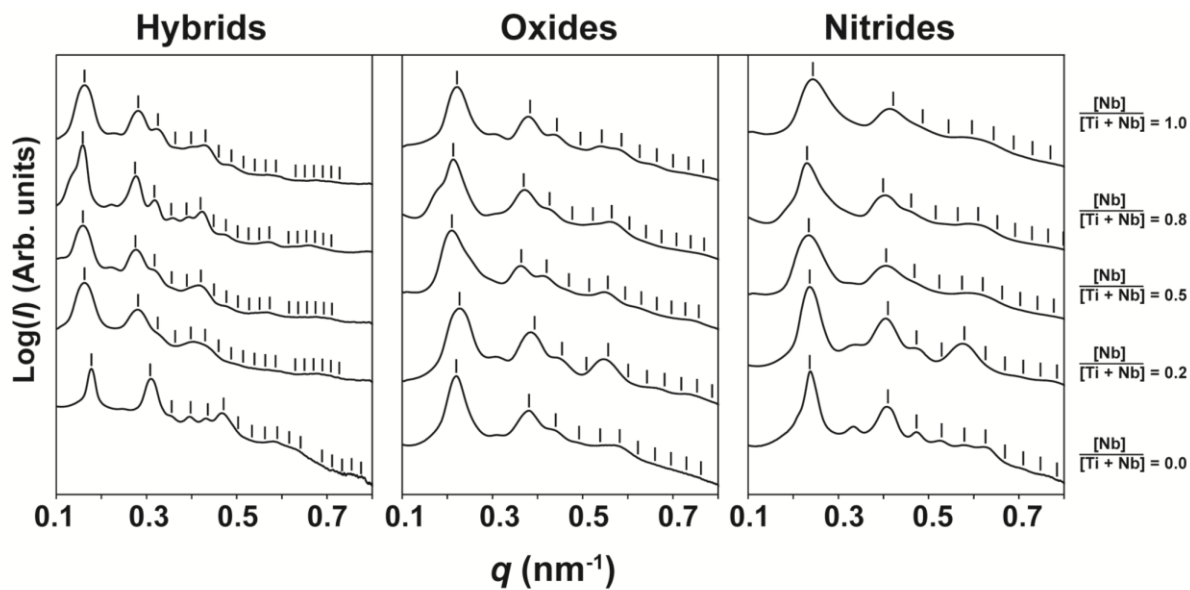


Figure 3.3. SAXS patterns for the five different Ti:Nb compositions at the three stages of processing: ISO/oxide hybrids (left), oxides (middle), and nitrides (right). The Ti:Nb ratio varies from 1:0 (bottom) to 0:1 (top). The peak markings indicate expected positions for the G^A morphology. $[Nb]/[Ti + Nb] = 0.0$ and 1.0 patterns used ISO-69 while the intermediate compositions used ISO-64. The SAXS patterns from the $Ti:Nb = 0.5$ sample and a different sample with the $Ti:Nb = 0.8$ composition have been previously reported²¹ and are shown here for comparison to the entire data set.

To investigate the samples' mesoscale morphologies and ordering, we used SAXS. SAXS patterns were collected for the different compositions (Figure 3.3) at the three processing steps: as-made BCP/oxide hybrids, freestanding mesoporous oxides, and freestanding mesoporous nitrides. The d_{100} -spacings for each sample are compiled in Table A3.2. For all atomic compositions, SAXS patterns for the BCP/oxide hybrids showed well-defined lattice reflections consistent with the G^A structure and d_{100} -spacings varying from 50 nm to 56 nm. We attribute these differences to differences in oxide loadings (see Supporting Information) and minor size and composition differences in ISO-64 and ISO-69. A small peak appears between $(q/q_{100})^2 = 2$ and $(q/q_{100})^2 = 6$ (the first two expected G^A peaks) in some patterns. This has been previously observed and attributed to the appearance of the forbidden $(q/q_{100})^2 = 4$ reflection due to symmetry breaking from compression of the structure in the z -axis occurring upon solvent evaporation and high T treatments.^{20,21,28} The broad shoulders on the $[Nb]/[Ti + Nb] = 0.8$ primary peaks are likely due to a small amount of mixed morphology with the G^A .

After calcination at 450 °C to yield freestanding mesoporous oxides, all compositions showed a similar trend in their SAXS patterns: shifting of the reflections to higher q (indicating shrinkage of the mesoscale unit cell), broadening of peaks (indicating a less well-defined scattering interface), and the loss of some higher order reflections (indicating some loss of long-range order). This behavior is consistent with what we expect and have previously observed in similar systems.^{21,28} The d_{100} -spacings at this step only varied from 39 nm to 42 nm. However, the amount of shrinkage in d_{100} -spacings varied between 19% to 28%, with no apparent trend. Differences in oxide loadings, densities, degrees of condensation, and degrees of crystallization could all contribute to these differences in shrinkage in this step.

After heating under flowing NH₃ gas at 600 °C to nitride the samples, all but one composition again showed the same trends: minor shrinkage of d_{100} -spacings, slight peak broadening and some loss of higher order peak intensity. While the d_{100} -spacing of the TiO₂/TiN sample decreases as expected, curiously, the peaks seem to sharpen and higher order peaks reappear. We believe this is due to the oxide film's normal having been slightly off-axis from the incident X-ray beam, causing some blurring of the scattering rings, rather than any exotic behavior (the corresponding two-dimensional patterns are shown in Figure A3.1). The d_{100} -spacings for the different nitride compositions only varied from 37 nm to 39 nm, despite differences in shrinkage from the oxides. As we have observed in previous work,²¹ the d_{100} -shrinkage between oxide and nitride is smaller than during the transition from BCP-oxide hybrid to freestanding oxide for all compositions, only varying from 4% to 9% from the oxide to nitride. The shrinkage for the Ti_{0.8}Nb_{0.2}O₂/Ti_{0.8}Nb_{0.2}N system is nearly half that of the next closest value for a different composition and this value is consistent with what we have observed previously for this particular composition.²¹ This very small shrinkage behavior seems to be unique to this composition and may be related to its partial crystallization which is only the case for this composition, as discussed in the X-ray diffraction section, *vide infra*.

We compared the shrinkage as measured from the photos of the diameters of the monolithic films (Figure 3.2) with the shrinkage measured from the SAXS d_{100} -spacings (Figure 3.3). We observe a good correlation between the macroscopic shrinkage and mesoscopic shrinkage, which is what we have previously shown for the gyroidal Ti_{0.8}Nb_{0.2}N and Ti_{0.5}Nb_{0.5}N systems.²¹ The comparison of these values is found in Table A3.3.

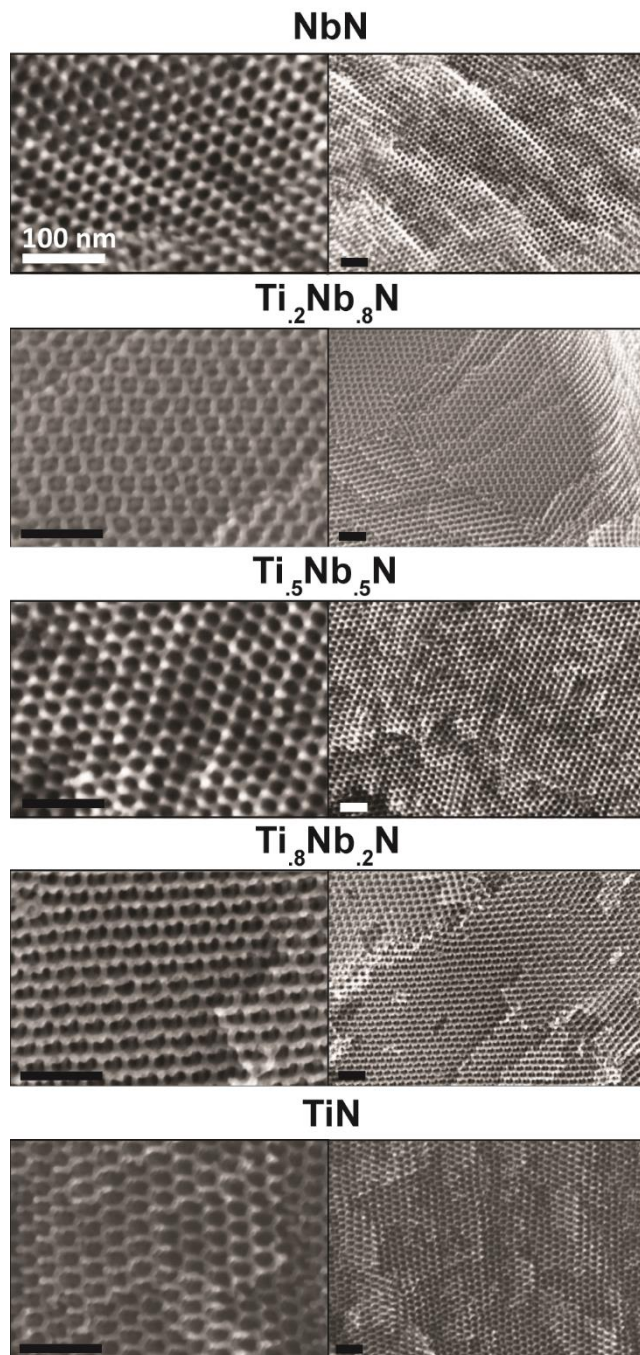


Figure 3.4. SEM images of the various G^A nitrides. The Ti:Nb ratio varies from 0:1 (top) to 1:0 (bottom). All scalebars are 100 nm. The Ti:Nb = 0.5 sample and a different sample with the Ti:Nb = 0.8 composition have been previously reported²¹ and are shown here for comparison with the rest of the data set.

Scanning electron microscopy (SEM) was used to complement the SAXS characterization of the nitrides' gyroidal mesostructures. Fractured samples of the different

nitride compositions were imaged without the addition of an electrically conductive coating, due to the materials' inherent electrical conductivity. The SEM images for the different compositions at two different magnifications are shown in Figure 3.4. All samples showed a structure consistent with the cubic G^A morphology, corroborating the SAXS results (Figure 3.3). All the compositions showed similar strut (~10 nm) and pore (~20 nm) dimensions, as measured from the SEM images and compiled in Table A3.4. However, we note that the dimensions measured *via* SEM are highly dependent on the sample orientation and that the SAXS measurements therefore provide a more reliable measurement of the morphology and lattice dimensions.

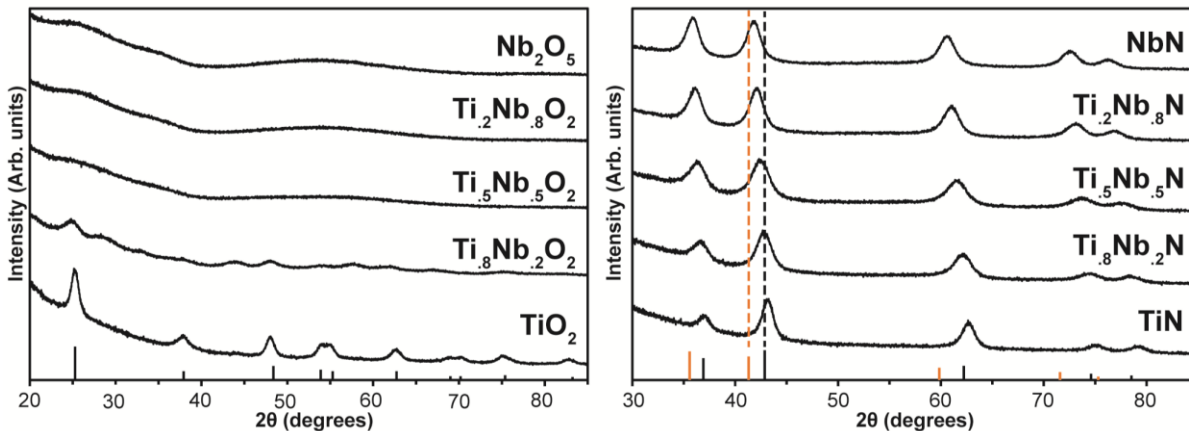


Figure 3.5. XRD patterns of the various G^A samples as oxides (left) and nitrides (right). The peak position and intensity markers for the oxide are for anatase TiO₂ (PDF card 00-001-0562). The peak markings and intensities for the nitrides are TiN (black, PDF card 04-015-2441) and NbN (orange, PDF card 04-008-5125). Dashed guides for the two nitrides' (200) peak positions show the shift of the reflection as a function of Nb content. The XRD patterns for the Ti:Nb = 0.5 sample and a different sample of the Ti:Nb = 0.8 composition have been previously reported²¹ and are shown here for comparison with the rest of the data set.

In order to study the atomic crystal structures of the gyroidal oxide and nitride compositions, powder X-ray diffraction (XRD) was used. As shown at the bottom left in Figure 3.5, after calcination in air at 450 °C, the oxide with the composition TiO₂ is crystalline anatase with a crystallite size of 8 nm as calculated from the Scherrer equation using the first peak. After the same heat treatment, the sample with the composition Ti_{0.8}Nb_{0.2}O₂ shows dramatically lower

intensity and broader reflections for the anatase peaks as compared to TiO₂. This indicates that crystallization is suppressed as compared to pure TiO₂, and that only very small crystallites are present in the sample along with predominantly amorphous content. This is consistent with what we have previously observed in gyroidal samples of this composition²¹ and it is due to the inclusion of Nb atoms in TiO₂ which suppresses the crystallization of anatase relative to pure TiO₂.^{8,9} After calcination at 450 °C, the Ti_{0.5}Nb_{0.5}O₂, Ti_{0.2}Nb_{0.8}O₂, and Nb₂O₅ compositions only show extremely broad humps in their XRD patterns, indicative of amorphous oxide material. These results are not surprising due to the crystallization suppression effect of Nb on TiO₂ and the fact that Nb₂O₅ crystallizes at or above 600 °C.⁴ As discussed in the SAXS section, at least four SAXS peaks are observed in each of these calcined oxide samples, indicating a retention of the gyroidal mesostructure during polymer removal, and in the case of TiO₂, crystallization.

Each of the aforementioned compositions of the freestanding gyroidal mesoporous oxides was subsequently nitrided by heating under flowing gaseous NH₃ at 600 °C. Powder XRD patterns were collected for all the nitride samples as shown on the right of Figure 3.5. In contrast to the gyroidal oxides, each composition of the nitrides crystallized during the nitridation. All the materials crystallize into the cubic rock salt structure, which is characteristic of transition metal nitrides including TiN, NbN, and Ti_{1-x}Nb_xN.^{12,13,29} In all cases, the peaks are shifted to higher 2θ values than the expected positions from the PDF cards, indicating a smaller unit cell which is almost certainly due to residual oxygen content in the material. This is expected considering the starting materials are oxides and the low nitriding temperatures employed in this work.³⁰⁻³³ The crystallite sizes for all the nitrides were calculated using the Scherrer equation using the first two XRD peaks and are tabulated together with crystallite sizes for the TiO₂ containing oxide samples in Table A3.5. While there is not a consistent trend of crystallite size as a function of

composition for the nitrides, the largest crystallite sizes are for the titanium rich compositions, TiN and $\text{Ti}_{0.8}\text{Nb}_{0.2}\text{N}$, suggesting that the more crystalline the starting oxide, the larger the subsequent nitride crystallites.

In the XRD patterns of the nitrides in Figure 3.5 (right side), as Nb content is increased, all of the peaks shift to lower angles and the relative intensities of the first two reflections (111 and 200) change from TiN-like to NbN-like. Using the 200 reflections (the second peak, between 40 and 45°), the cubic lattice parameters ($a = 2^*d_{200}$) were calculated for all samples and plotted (Figure A3.2) as function of Nb content ($[\text{Nb}]/[\text{Ti} + \text{Nb}]$). The data set shows excellent linearity, in accordance with Vegard's Law, which states that the lattice parameter in alloys is linearly proportional to the atomic composition of the alloy's components.³⁴ This finding, along with the appearance of only a single set of peaks for all nitride compositions suggests that the gyroidal Ti-Nb mesoporous nitrides studied here are single phase alloys at any composition and do not macrophase separate. This is consistent with what has been reported in the literature by us¹² and others.¹³ As mentioned above, all of the gyroidal nitride compositions retain at least three peaks in their SAXS patterns, indicating the retention of long-range order despite heat treatment up to 600 °C and crystallization or crystal structure changes. In the cases of the $\text{Ti}_{0.5}\text{Nb}_{0.5}\text{N}$, $\text{Ti}_{0.2}\text{Nb}_{0.8}\text{N}$, and NbN, the materials undergo amorphous-to-crystalline transitions while retaining the ordered mesostructure. Especially interesting are the $\text{Ti}_{0.8}\text{Nb}_{0.2}\text{N}$ and TiN compositions that showed at least some crystallinity as freestanding gyroidal oxides before nitriding. From their SAXS patterns, these two compositions show the best retention of their ordered mesostructure, maintaining sharp and higher order peaks better than the Nb-richer compositions. The combination of SAXS and XRD data suggests that the more crystalline the starting oxide material, the better the ordered mesostructure retention during heat processing. If an amorphous-

to-crystalline transition is a driving force for mesostructure collapse, the presence of some sort of support for the gyroidal structure may serve to mitigate collapse. With TiO_2 and $\text{Ti}_{0.8}\text{Nb}_{0.2}\text{O}_2$, some crystallization may be occurring before the polymeric material is completely removed which could serve as a support and lessen the loss of ordered structure. Additionally, $\text{Ti}_{0.8}\text{Nb}_{0.2}\text{O}_2$ appears to be comprised of small crystallites within an amorphous oxide matrix which could also serve as a solid support during further crystallization or crystal structure change.²¹ However, the complete crystalline-to-crystalline change in the TiO_2/TiN system without much loss of mesostructural order is quite surprising and may be due to the gradual direct conversion of anatase TiO_2 to rock salt TiN rather than an abrupt crystallization of TiN .³³ In all cases, we speculate that the three-dimensional continuous nature of the gyroid structure and the slow ramp rates of the heat processing contribute to the retention of the mesostructure despite polymer removal, shrinkage, atomic composition and crystal structure changes all at temperatures up to 600 °C.

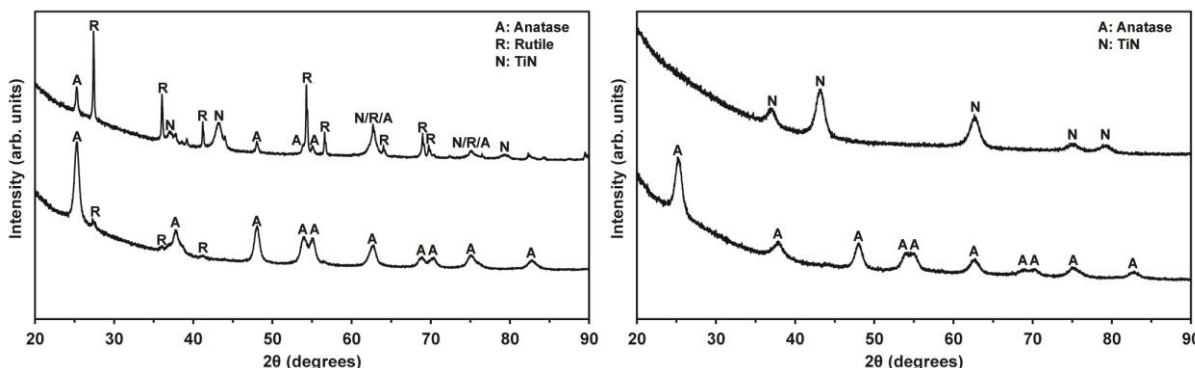


Figure 3.6. XRD patterns for non-mesostructured sol-gel TiO_2 after calcination (left, bottom) and heating under NH_3 (left, top) compared to G^A TiO_2 after calcination (right, bottom) and after heating under NH_3 (right, top). Peaks were labeled for the different observed phases: anatase TiO_2 (“A”), rutile TiO_2 (“R”), and cubic rock salt TiN (“N”).

In order to investigate the effects of the ordered mesostructure on the crystal structure and nitriding process, non-mesostructured sol-gel TiO_2 (no BCP present in the synthesis) was subjected to the same processing as the gyroidal structures. TiO_2 was the composition selected

since it is already crystalline after the calcination step. The XRD patterns of the resulting non-mesostructured TiO₂/TiN samples are shown in Figure 3.6 (left), in comparison with the gyroidal TiO₂/TiN Figure 3.6 (right). After calcination at 450 °C, the non-structured material (Figure 3.6, left bottom) shows predominantly anatase TiO₂ with a small amount of rutile TiO₂, whereas the gyroidal TiO₂ (Figure 3.6, right bottom) is purely anatase. The phase composition for the non-mesostructured material was estimated by the reference intensity ratio (RIR) method³⁵ to be 94 wt% anatase and 6 wt% rutile. Additionally, the crystallite sizes (calculated using the Scherrer equation and the first peak of each oxide phase) were 12 nm for anatase and 16 nm for rutile in the non-mesostructured TiO₂ and 8 nm for anatase in the gyroidal sample.

When constrained within the gyroidal network structure, the crystallites' size appears to be limited so rutile does not nucleate. It is well-known that rutile, the thermodynamically stable TiO₂ phase, begins nucleating and rapidly growing once anatase crystallites grow above a certain threshold, around 14 nm,³⁶⁻³⁹ which is consistent with our observations in this system. It has also been observed that the constraint of TiO₂ in mesoporous networks can limit crystallite growth at moderate temperatures, and thus suppress rutile crystallization while the network remains intact.⁴⁰ Once the crystallites overgrow the feature size of the network components, the mesostructure collapses, the size constraining effects are lost and concurrently, rutile rapidly crystallizes and grows.³⁹ Without this constraint, the non-structured material forms larger crystallites, thus nucleating rutile, even at 450 °C.

After nitriding at 600 °C, the non-mesostructured material (Figure 3.6, top left) shows a mixture of three phases: 46 wt% cubic TiN, 41 wt% rutile TiO₂, and 13 wt% anatase TiO₂. In stark contrast, the gyroidal sample nitrided at 600 °C only shows a single phase: cubic TiN and there is no crystalline oxide present. The crystallite sizes for the non-structured material were

calculated using the Scherrer equation using the first peak of each oxide phase and the second peak of the nitride: 9 nm for TiN, ~70 nm for rutile, and ~30 nm for anatase. For the gyroidal sample, the single phase of TiN crystallite size was estimated from the Scherrer equation using the second peak and was 6 nm.

Aside from preventing the nucleation of rutile, the gyroidal mesostructure also facilitates the nitriding process, resulting in a complete conversion of crystalline oxide into crystalline nitride (in contrast to the partial nitriding for the non-mesostructured material). The porosity of gyroidal oxide allows gases to easily diffuse in and out of the films, which is necessary for the conversion of oxides to nitrides. Additionally, the gyroidal structure has inorganic features smaller than 20 nm (see SEM section) which limits solid state diffusion lengths for O and N atoms during the nitridation, which in turn has been shown to be kinetically limited by diffusion.³³ Less mesoporosity and larger crystallites (and thus longer solid state diffusion lengths) in the non-mesostructured TiO₂ results in the incomplete nitridation observed in the XRD, yielding the mixture of nitride and oxide phases. Furthermore, it has been reported that the reaction of rutile TiO₂ with NH₃ is slower than that of anatase TiO₂ in the conversion to TiN, thus contributing to the incomplete conversion of the non-gyroidal material.³³ It is interesting that although the oxide crystallite sizes in the non-mesostructured material greatly exceed any crystallite sizes observed in gyroids, the nitride phase's crystallite size in the non-mesostructured material (9 nm) is not dramatically larger than crystallite size of the pure gyroidal TiN (6 nm) compared to the difference for the oxides. This similarity is attributed to the solid state diffusion of O and N, where only the outside of the oxide crystallites converts to nitride in the non-structured material. The gyroid's inorganic feature size is sufficiently small that O and N can diffuse sufficiently during the nitridation to yield only the nitride crystal structure. This

comparison shows the benefits of the gyroidal structure during the nitridation of oxides: allowing for lower temperatures and shorter dwells during the nitriding step. In turn, these mild heating procedures allow the preservation of the highly ordered gyroid structures which can collapse if the processing temperatures are too high for too long and the crystallites overgrow the network.^{40,41}

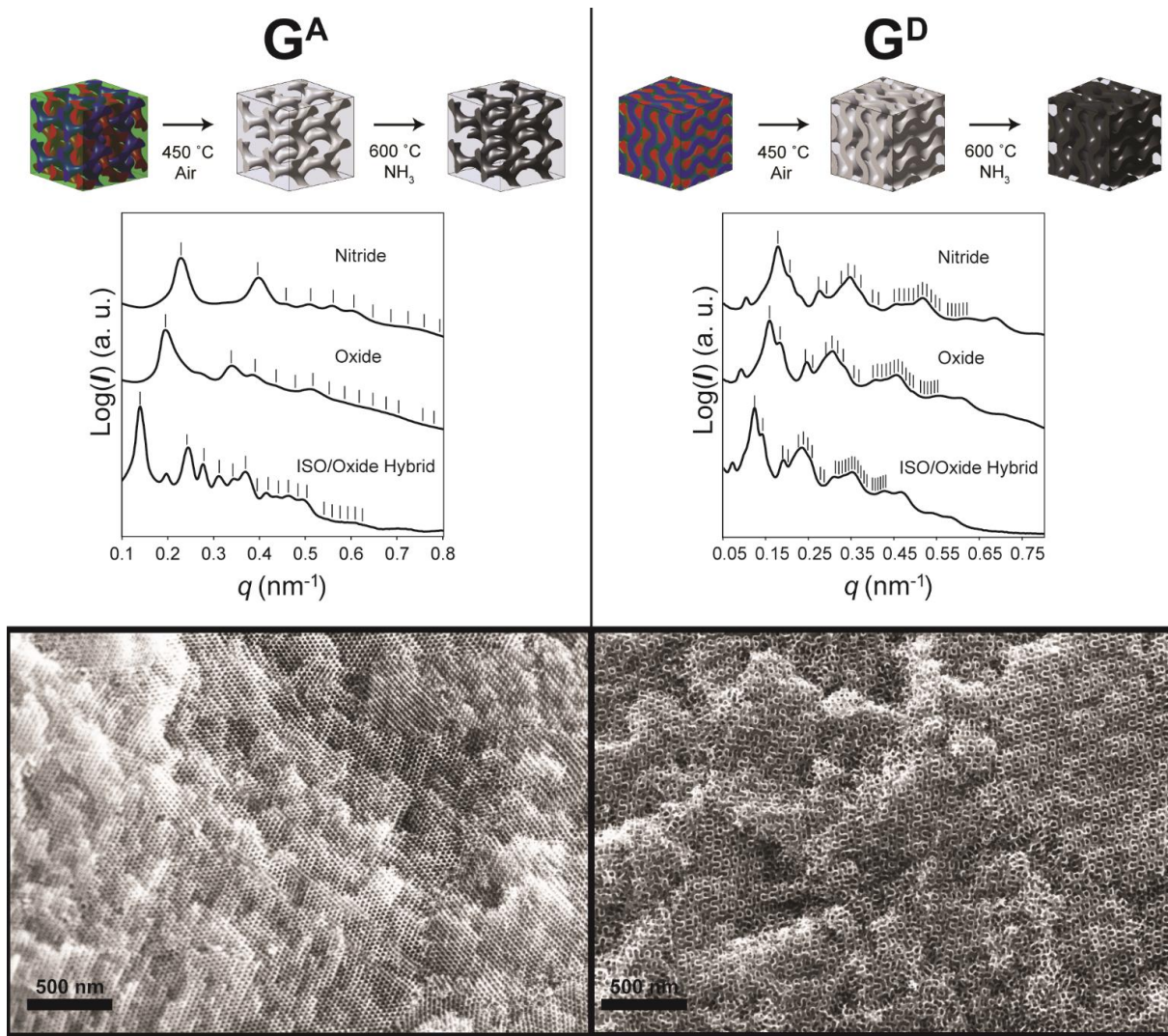


Figure 3.7. Schematics of syntheses and morphologies (top), SAXS patterns throughout processing (middle), and SEM images (bottom) for ISO-93 alternating gyroid (G^A) NbN (left) and core-shell double gyroid (G^D) NbN (right).

In order to demonstrate the tunability of nitride structures via the molecular terpolymer structure, a larger ISO terpolymer, ISO-93, was used to generate highly ordered mesoporous

gyroidal nitride structures using Nb_2O_5 sol. By tuning the BCP:oxide ratio, two different gyroidal structures (the alternating gyroid, G^{A} , and the core-shell double gyroid, G^{D}) were synthesized using the same BCP. At low oxide loadings (12 wt% oxide *via* TGA), the G^{A} structure is formed from ISO-93 where the PEO/oxide domains comprise one of the gyroid networks (shown as the blue network in Figure 3.7, left), as was the case with ISO-64 and ISO-69. At a higher oxide loading (26 wt% oxide *via* TGA), ISO-93 forms the G^{D} structure where the PEO/oxide domains comprise the matrix/majority between the core-shell gyroid minority networks (shown as the blue matrix in Figure 3.7, right). Schematics of the two different gyroid structures, as well as SAXS of the hybrids, oxides, and nitrides, and SEM images of the resulting nitrides are shown in Figure 3.7: G^{A} (left) and G^{D} (right). The gyroidal ISO/ Nb_2O_5 hybrids from ISO-93 were subjected to the same processing as described for ISO-64 and ISO-69: calcination at 450 °C in air to yield a freestanding gyroidal oxide, and nitridation at 600 °C in NH_3 to yield a freestanding gyroidal nitride. These samples also retain their macroscopic integrity during the heat processing and do not pulverize to powders.

The SAXS patterns of the two structures at the different stages of processing are shown in the middle of Figure 3.7: G^{A} ISO/ Nb_2O_5 hybrid (left, bottom), G^{A} Nb_2O_5 (left, middle), G^{A} NbN (left, top); G^{D} ISO/ Nb_2O_5 hybrid (right, bottom), G^{D} Nb_2O_5 (right, middle), G^{D} NbN (right, top). As we have seen in the smaller BCP systems, the d_{100} -spacings decrease throughout the heat treatment, indicating a shrinkage in the unit cell. For the ISO-93 G^{A} , the d_{100} -spacings were: 64 nm for the hybrid, 46 nm for the oxide, and 39 nm for the nitride. For the ISO-93 G^{D} , the d_{100} -spacings were: 124 nm for the hybrid, 97 nm for the oxide, and 86 nm for the nitride. These values are tabulated along with the d -spacings for the Nb_2O_5 system from ISO-69 in Table A3.6. The d -spacings for the G^{D} structure are about twice as large as for G^{A} . This is due to the fact that

the two gyroid networks in the G^A are from the two endblocks of the BCP while the two gyroid networks in the G^D are from the same endblock. As such, a single BCP chain can contribute volume to both networks and the matrix in the G^A but only one network with its shell and part of the matrix in the G^D.¹⁹ The appearance of a small sharp peak before the first indexed G^D peak and a broad shoulder on the first indexed G^D peak is similar to the appearance of the forbidden $(q/q_{100})^2 = 4$ reflection in the G^A. We attribute the appearance of these forbidden $(q/q_{100})^2 = 2$ and $(q/q_{100})^2 = 4$ reflections in the G^D to *z*-axis compression which has already been described in ISO/carbon G^D systems.⁴²

To our surprise, the gyroid structures from ISO-93 were remarkably ordered, based on the SAXS patterns and SEM images, showing an impressive retention of mesoscale ordering even after the calcination and nitridation—even better than that of the Nb₂O₅ samples from the smaller BCPs. It is also interesting that while ISO-93 is significantly larger than ISO-64 or ISO-69, it results in a similar *d*₁₀₀-spacing for the NbN G^A (39 nm) as the NbN G^A from ISO-69 (37 nm). This is due to a smaller oxide loading (12 wt% *via* TGA) for ISO-93 compared to that of ISO-69 (20 wt% *via* TGA). This shows the tunability of the cubic gyroidal lattice parameters by altering the molar mass and oxide loading, without dramatically changing the relative composition of the polymer blocks.

XRD measurements were performed on the oxides and nitrides of the different gyroidal samples synthesized from ISO-93 (Figures A3.3 and A3.4). Similar to the results with Nb₂O₅ and ISO-64 and ISO-69, both gyroid structures from ISO-93 were amorphous oxides after calcination, and crystallized in the cubic rock salt structure for NbN after nitriding. The G^A and G^D nitride crystallite sizes, estimated from the Scherrer equation using the first two peaks of each pattern, were both 5 nm, as was the ISO-69 NbN G^A. The results from ISO-93 show the ability to

synthesize highly ordered hybrid, oxide, and nitride structures using larger ISO BCPs, as well as the ability to achieve multiple gyroidal structures from the same BCP by changing the BCP:oxide ratio.

The ability to control both the atomic composition and mesoscale morphology of transition metal oxides and nitrides is critical for achieving the best possible performance for different applications. We have demonstrated here that amphiphilic block copolymers provide an excellent platform for the generation of gyroidal mesoporous oxides and nitrides with unprecedented macroscopic integrity and mesoscale ordering for inorganic materials. We showed various gyroidal binary and ternary oxides and nitrides by changing the Ti:Nb ratio in $Ti_{1-x}Nb_xO_2$ and $Ti_{1-x}Nb_xN$ systems. We then demonstrated the benefits of the networked cubic gyroid structure on the nitriding process, which facilitates impressive structural behavior and crystal phase purity. We also showed the use of a larger BCP to generate multiple gyroidal structures from a single polymer by changing the BCP:oxide ratio. We believe these synthetic strategies will prove useful for generating ordered 3D mesostructures of numerous oxides and nitrides and in analyzing the mesostructural effects in broadly ranging fields from energy conversion and storage and catalysis to plasmonics and superconductivity.

Acknowledgements

This work was supported as part of the Energy Materials Center at Cornell (EMC2), an Energy Frontier Research Center funded by the U.S. Department of Energy, Office of Science, Basic Energy Sciences under Award # DE-SC0001086. This work made use of the Cornell Center for Materials Research Shared Facilities, which are supported through the NSF MRSEC program (DMR-1120296). This work is based upon research conducted at the Cornell High Energy Synchrotron Source (CHESS), which is supported by the National Science Foundation and the

National Institutes of Health/National Institute of General Medical Sciences under NSF award DMR-0936384. H.S. was supported by the NSF Single Investigator Award (DMR-1104773).

REFERENCES

1. O'Regan, B.; Gratzel, M. *Nature* **1991**, *353*, 737.
2. Kazuhito, H.; Hiroshi, I.; Akira, F. *Japanese Journal of Applied Physics* **2005**, *44*, 8269.
3. Avellaneda, C. O.; Macedo, M. A.; Florentino, A. O.; Barros Filho, D.; Aegeerter, M. A. 1994; Vol. 2288, p 422.
4. Augustyn, V. *et al. Nat. Mater.* **2013**, *12*, 518.
5. Sproul, W. D. *Surf. Coat. Technol.* **1996**, *81*, 1.
6. Naik, G. V. *et al. Optical Materials Express* **2012**, *2*, 478.
7. Gerstenberg, D.; Hall, P. M. *J. Electrochem. Soc.* **1964**, *111*, 936.
8. Dros, A. B. *et al. Microporous Mesoporous Mater.* **2006**, *94*, 208.
9. Liu, Y. J. *et al. ACS Nano* **2010**, *4*, 5373.
10. Furubayashi, Y. *et al. Appl. Phys. Lett.* **2005**, *86*.
11. Cui, Z.; Burns, R. G.; DiSalvo, F. J. *J. Chem. Mater.* **2013**, *25*, 3782.
12. Yang, M.; Van Wassen, A. R.; Guarecuco, R.; Abruña, H. D.; DiSalvo, F. J. *J. Chem. Commun. (Cambridge, U. K.)* **2013**, *49*, 10853.
13. Vasu, K.; Krishna, M. G.; Padmanabhan, K. A. *J. Mater. Sci.* **2012**, *47*, 3522.
14. Córdoba, R. *et al. Nat. Commun.* **2013**, *4*, 1437.
15. Rolison, D. R. *et al. Chem. Soc. Rev.* **2009**, *38*, 226.
16. Orilall, M. C.; Wiesner, U. *Chem. Soc. Rev.* **2011**, *40*, 520.
17. Ren, Y.; Ma, Z.; Bruce, P. G. *Chem. Soc. Rev.* **2012**, *41*, 4909.
18. Deng, Y.; Wei, J.; Sun, Z.; Zhao, D. *Chem. Soc. Rev.* **2013**, *42*, 4054.
19. Meuler, A. J.; Hillmyer, M. A.; Bates, F. S. *Macromolecules* **2009**, *42*, 7221.
20. Stefk, M. *et al. J. Mater. Chem.* **2012**, *22*, 1078.
21. Robbins, S. W.; Sai, H.; DiSalvo, F. J.; Gruner, S. M.; Wiesner, U. *ACS Nano* **2014**, *8*, 8217.
22. Allgaier, J.; Poppe, A.; Willner, L.; Richter, D. *Macromolecules* **1997**, *30*, 1582.
23. Warren, S.; DiSalvo, F. J.; Wiesner, U. *Nat. Mater.* **2007**, *6*, 248.
24. Bailey, T. S.; Pham, H. D.; Bates, F. S. *Macromolecules* **2001**, *34*, 6994.

25. Finnefrock, A. C.; Ulrich, R.; Toombes, G. E. S.; Gruner, S. M.; Wiesner, U. *J. Am. Chem. Soc.* **2003**, *125*, 13084.
26. Templin, M. *et al. Science* **1997**, *278*, 1795.
27. Hoheisel, T. N.; Hur, K.; Wiesner, U. B. *Prog. Polym. Sci.* **2015**, *In Press*.
28. Toombes, G. E. S. *et al. Macromolecules* **2007**, *40*, 8974.
29. Yen, C. M.; Toth, L. E.; Shy, Y. M.; Anderson, D. E.; Rosner, L. G. *J. Appl. Phys.* **1967**, *38*, 2268.
30. Kamiya, K.; Nishijima, T.; Tanaka, K. *J. Am. Ceram. Soc.* **1990**, *73*, 2750.
31. Nomura, K.; Takasuka, Y.; Kamiya, K.; Nasu, H. *J. Mater. Sci.: Mater. Electron.* **1994**, *5*, 53.
32. Kościelska, B.; Winiarski, A.; Kusz, B. *J. Non-Cryst. Solids* **2009**, *355*, 1342.
33. Chen, H. *et al. The Journal of Physical Chemistry C* **2006**, *111*, 1366.
34. Denton, A. R.; Ashcroft, N. W. *Phys. Rev. A* **1991**, *43*, 3161.
35. Hubbard, C. R.; Evans, E. H.; Smith, D. K. *J. Appl. Crystallogr.* **1976**, *9*, 169.
36. Gribb, A. A.; Banfield, J. F. *Am. Mineral.* **1997**, *82*, 717.
37. Zhang, H.; F. Banfield, J. *J. Mater. Chem.* **1998**, *8*, 2073.
38. Hwang, J.; Kim, J.; Ramasamy, E.; Choi, W.; Lee, J. *Microporous Mesoporous Mater.* **2011**, *143*, 149.
39. Guldin, S. *et al. Energy & Environmental Science* **2011**, *4*, 225.
40. Fattakhova-Rohlfing, D.; Wark, M.; Brezesinski, T.; Smarsly, B. M.; Rathouský, J. *Adv. Funct. Mater.* **2007**, *17*, 123.
41. Choi, S. Y.; Mamak, M.; Speakman, S.; Chopra, N.; Ozin, G. A. *Small* **2005**, *1*, 226.
42. Werner, J. G.; Hoheisel, T. N.; Wiesner, U. *ACS Nano* **2013**, *8*, 731.

APPENDIX 2

Gyroidal ISO/Nb₂O₅ Hybrids: An amount of an ISO was dissolved in THF to give a 3.5-4.0 wt% solution. The Nb₂O₅ sol was prepared by a hydrolytic route using HCl and THF. 0.30 mL of HCl was combined with 1.0 mL (12.3 mmol) of THF and was stirred in a 4 mL vial. 0.51 mL (2.0 mmol) of Nb(OEt)₅ was quickly added to the vial through a vented septum cap. After 5 minutes of vigorous stirring, 1.0 mL (12.3 mmol) of THF was added. After stirring for 2 minutes, an aliquot of the bright yellow sol was added to the ISO/THF solution. For a G^A hybrid with ISO-64, 0.32 mL of sol was added per 100 mg of ISO. For a G^A hybrid with ISO-69, 0.34 mL of sol was added per 100 mg of ISO. For a G^A hybrid with ISO-93, 0.2 mL of sol was added per 100 mg of ISO. For a G^D hybrid with ISO-93, 0.4 mL of sol was added per 100 mg of ISO. For ISO-64 and ISO-69, the solutions were stirred for at least 3 hours and poured into PTFE casting dishes. The PTFE dishes were placed on a glass crystallization dish and covered with a glass hemispherical dome and placed on a hot plate set to 50 °C. The solvent was evaporated overnight and the samples were moved to a vacuum oven and heated at 130 °C in vacuum for at least 3 hours as an aging procedure. After this treatment, the samples were the BCP/oxide hybrid samples as characterized in the main text. For ISO-93 samples, the stirring and casting procedures slightly differed: the ISO/oxide/THF solution was stirred overnight and cast at 35 °C rather than 50 °C, and included a small PTFE dish with additional THF during casting. The evaporation process took 24-48 h.

Gyroidal ISO/Ti_{0.8}Nb_{0.2}O₂ Hybrids: An amount of an ISO was dissolved in THF to give a 3.5-4.0 wt% solution. The Ti_{0.8}Nb_{0.2}O₂ sol was prepared by a hydrolytic route using HCl and THF. A mixed alkoxide precursor was first prepared under the inert atmosphere of a glovebox. 2.0 mL (6.8 mmol) of Ti(OiPr)₄ was combined with 0.43 mL (1.7 mmol) of Nb(OEt)₅ in a small vial and

stirred. 0.93 mL of the mixed alkoxide precursor was drawn up to be used for the sol synthesis. 0.30 mL of HCl was combined with 1.0 mL (12.3 mmol) of THF and was stirred in a 4 mL vial. The 0.93 mL aliquot of the mixed $\text{Ti}(\text{O}i\text{Pr})_4/\text{Nb}(\text{OEt})_5$ alkoxide precursor was quickly added to the vial through a vented septum cap. After 5 minutes of vigorous stirring, 1.0 mL (12.3 mmol) of THF was added. After stirring for 2 minutes, an aliquot of the bright yellow sol was added to the ISO/THF solution. For a G^A hybrid with ISO-64, 0.32 mL of sol was added per 100 mg of ISO. The solutions were stirred at least 3 hours and poured into PTFE casting dishes. The PTFE dishes were placed on a glass crystallization dish and covered with a glass hemispherical dome and placed on a hot plate set to 50 °C. The solvent was evaporated overnight and the samples were moved to a vacuum oven and heated at 130 °C in vacuum for at least 3 hours as an aging procedure. After this treatment, the samples were the BCP/oxide hybrid samples as characterized in the main text.

Gyroidal ISO/ $\text{Ti}_{0.5}\text{Nb}_{0.5}\text{O}_2$ Hybrids: An amount of an ISO was dissolved in THF to give a 3.5-4.0 wt% solution. The $\text{Ti}_{0.5}\text{Nb}_{0.5}\text{O}_2$ sol was prepared by a hydrolytic route using HCl and THF. A mixed alkoxide precursor was first prepared under the inert atmosphere of a glovebox. 0.90 mL (3.0 mmol) of $\text{Ti}(\text{O}i\text{Pr})_4$ was combined with 0.74 mL (3.0 mmol) of $\text{Nb}(\text{OEt})_5$ in a small vial and stirred. 0.85 mL of the mixed alkoxide precursor was drawn up to be used for the sol synthesis. 0.30 mL of HCl was combined with 1.0 mL (12.3 mmol) of THF and was stirred in a 4 mL vial. The 0.85 mL aliquot of the mixed $\text{Ti}(\text{O}i\text{Pr})_4/\text{Nb}(\text{OEt})_5$ alkoxide precursor was quickly added to the vial through a vented septum cap. After 5 minutes of vigorous stirring, 1.0 mL (12.3 mmol) of THF was added. After stirring for 2 minutes, an aliquot of the bright yellow sol was added to the ISO/THF solution. For a G^A hybrid with ISO-64, 0.32 mL of sol was added per 100 mg of ISO. The solutions were stirred at least 3 hours and poured into PTFE casting dishes. The PTFE

dishes were placed on a glass crystallization dish and covered with a glass hemispherical dome and placed on a hot plate set to 50 °C. The solvent was evaporated overnight and the samples were moved to a vacuum oven and heated at 130 °C in vacuum for at least 3 hours as an aging procedure. After this treatment, the samples were the BCP/oxide hybrid samples as characterized in the main text.

Gyroidal ISO/Ti_{0.2}Nb_{0.8}O₂ Hybrids: An amount of an ISO was dissolved in THF to give a 3.5-4.0 wt% solution. The Ti_{0.2}Nb_{0.8}O₂ sol was prepared by a hydrolytic route using HCl and THF. A mixed alkoxide precursor was first prepared under the inert atmosphere of a glovebox. 0.25 mL (0.84 mmol) of Ti(O*i*Pr)₄ was combined with 0.83 mL (3.3 mmol) of Nb(OEt)₅ in a small vial and stirred. 0.63 mL of the mixed alkoxide precursor was drawn up to be used for the sol synthesis. 0.30 mL of HCl was combined with 1.0 mL (12.3 mmol) of THF and was stirred in a 4 mL vial. The 0.63 mL aliquot of the mixed Ti(O*i*Pr)₄/Nb(OEt)₅ alkoxide precursor was quickly added to the vial through a vented septum cap. After 5 minutes of vigorous stirring, 1.0 mL (12.3 mmol) of THF was added. After stirring for 2 minutes, an aliquot of the bright yellow sol was added to the ISO/THF solution. For a G^A hybrid with ISO-64, 0.32 mL of sol was added per 100 mg of ISO. The solutions were stirred at least 3 hours and poured into PTFE casting dishes. The PTFE dishes were placed on a glass crystallization dish and covered with a glass hemispherical dome and placed on a hot plate set to 50 °C. The solvent was evaporated overnight and the samples were moved to a vacuum oven and heated at 130 °C in vacuum for at least 3 hours as an aging procedure. After this treatment, the samples were the BCP/oxide hybrid samples as characterized in the main text.

Gyroidal ISO/TiO₂ Hybrids: An amount of an ISO was dissolved in THF to give a 3.5-4.0 wt% solution. The TiO₂ sol was prepared by a hydrolytic route using HCl and THF. 0.30 mL of HCl

was stirred in a 4 mL vial. 1.0 mL (3.4 mmol) of Ti(O*i*Pr)₄ was added to the vial through a vented septum cap. After 5 minutes of vigorous stirring, 2.0 mL (24.6 mmol) of THF was added. After stirring for 2 minutes, an aliquot of the bright yellow sol was added to the ISO/THF solution. For a G^A hybrid with ISO-69, of sol was added per 100 mg of ISO. The solutions were stirred at least 3 hours and poured into PTFE casting dishes. The PTFE dishes were placed on a glass crystallization dish and covered with a glass hemispherical dome and placed on a hot plate set to 50 °C. The solvent was evaporated overnight and the samples were moved to a vacuum oven and heated at 130 °C in vacuum for at least 3 hours as an aging procedure. After this treatment, the samples were the BCP/oxide hybrid samples as characterized in the main text.

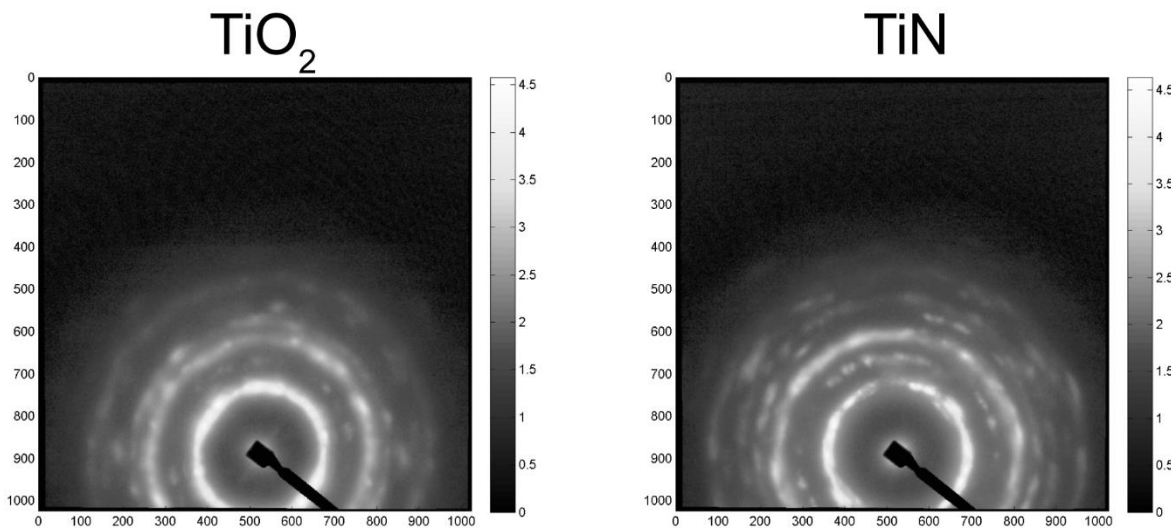


Figure A3.1. Two-dimensional SAXS patterns for gyroidal TiO₂ and gyroidal TiN. Measuring with the incident X-ray beam slightly off-axis of the film normal could cause the distortion and slight blurring of the pattern for TiO₂

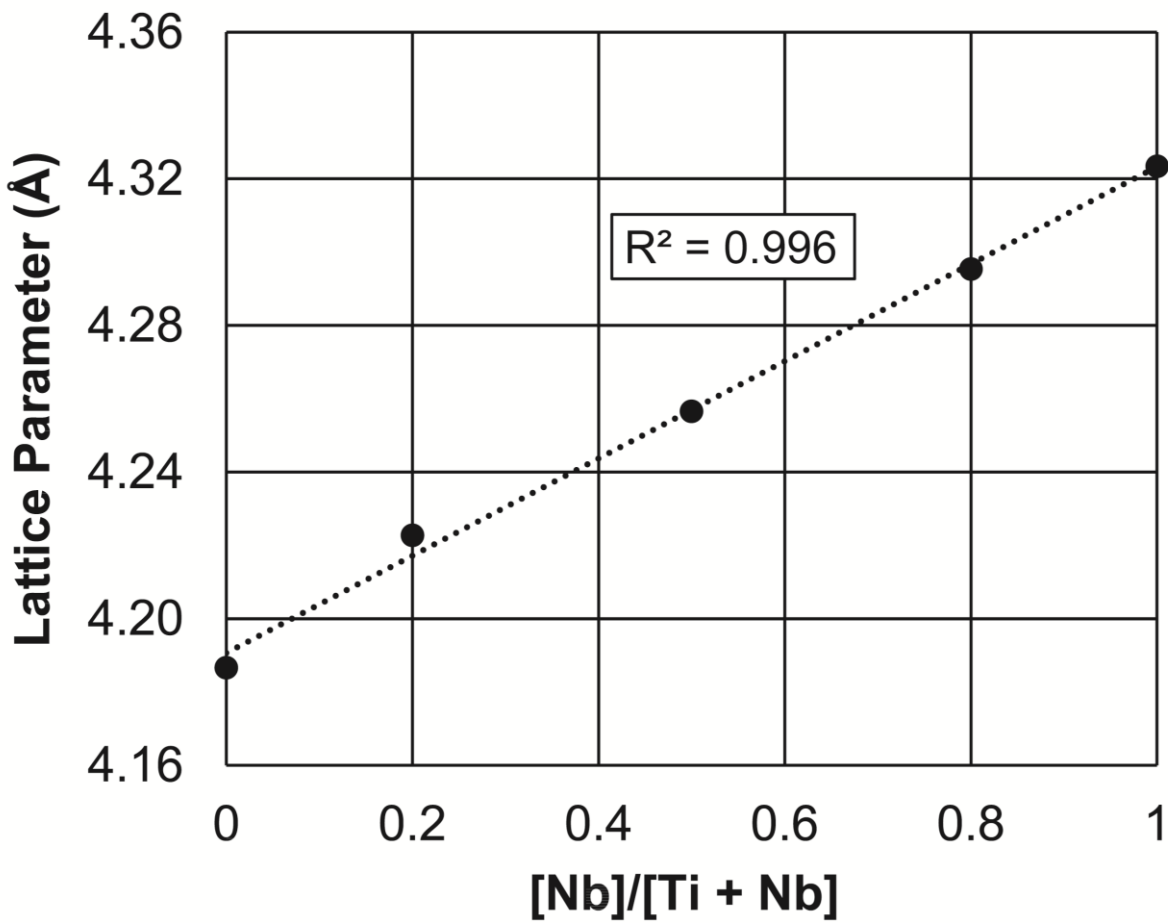


Figure A3.2. Plot of nitride lattice parameter versus Nb content. A linear fit shows excellent correlation to Vegard's Law which states that in alloys, the lattice parameter is linearly proportional to the composition of the constituents.

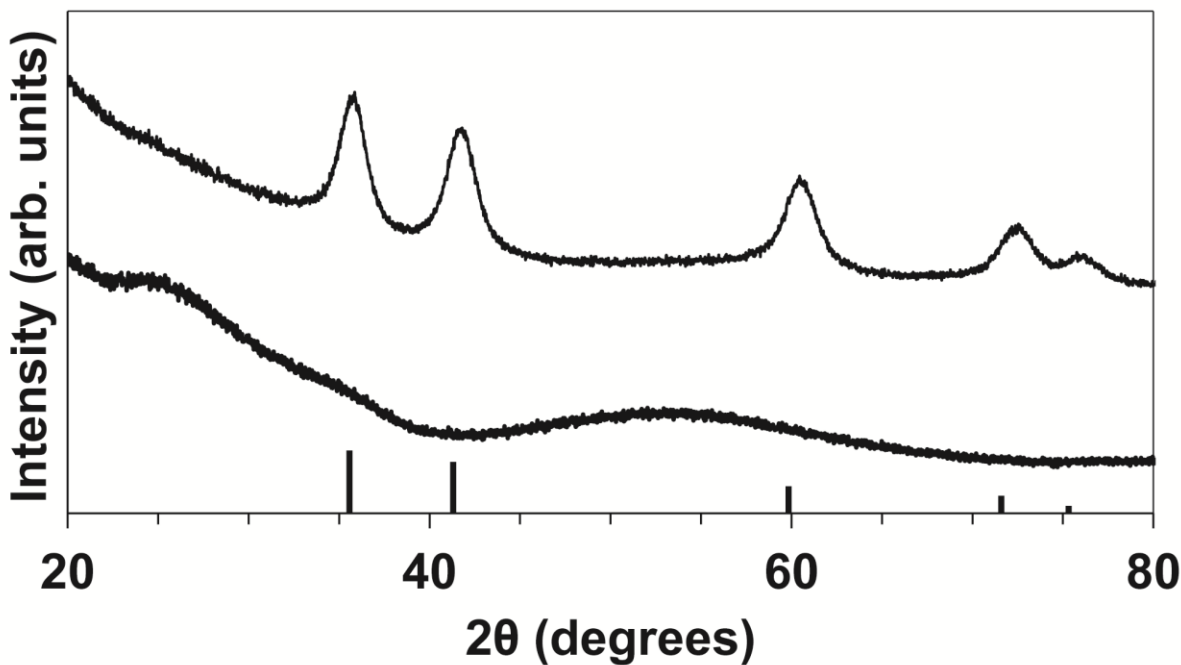


Figure A3.3. Powder XRD of the G^{A} Nb_2O_5 (bottom) and NbN (top) samples from ISO-93. The oxide is amorphous and the nitride is crystalline with the cubic rock salt structure characteristic of NbN. Peak position and intensity markers are shown for NbN (PDF Card 04-008-5125).

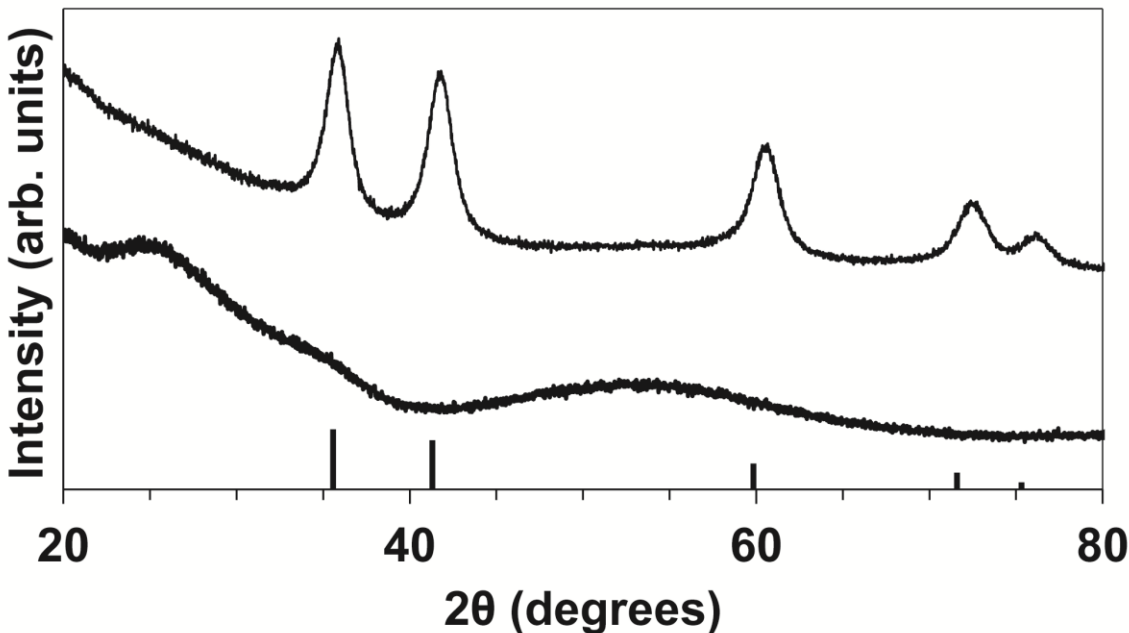


Figure A3.4. Powder XRD of the G^{D} Nb_2O_5 (bottom) and NbN (top) samples from ISO-93. The oxide is amorphous and the nitride is crystalline with the cubic rock salt structure characteristic of NbN. Peak position and intensity markers are shown for NbN (PDF Card 04-008-5125).

Table A3.1. Diameters and comparisons of samples at various stages of processing, as measured from the photos in Figure 3.2.

Composition [Nb]/[Ti + Nb]	Hybrid diameter (cm)	Oxide diameter (cm)	% of hybrid diameter	Nitride diameter (cm)	% of hybrid diameter
1	1.59	1.15	73%	1.08	68%
0.0	1.62	1.27	78%	1.21	75%

Table A3.2. d_{100} -spacings and comparisons of samples at various stages of processing, from the SAXS patterns in Figure 3.3.

Composition [Nb]/[Ti + Nb]	Hybrid d_{100} spacing (nm)	Oxide d_{100} spacing (nm)	% of hybrid d_{100} spacing	Nitride d_{100} spacing (nm)	% of hybrid d_{100} spacing
1	55	40	73%	37	67%
0.8	56	42	75%	39	70%
0.5	56	42	75%	38	68%
0.2	55	39	71%	38	69%
0.0	50	40	80%	37	74%

Table A3.3. Comparison of shrinkage measured from photos (Figure 3.2) and SAXS d_{100} -spacings (Figure 3.3) for $[Nb]/[Ti + Nb] = 1$, and 0.0.

Composition [Nb]/[Ti + Nb]	% of hybrid diameter from photos (oxide)	% of hybrid d_{100} spacing (oxide)	% of hybrid diameter from photos (nitride)	% of hybrid d_{100} spacing (nitride)
1	73%	73%	68%	67%
0.0	78%	81%	75%	75%

Table A3.4. Nitride gyroid features as measured by SEM for the various compositions.

Composition	Pore Diameter (nm)	Strut diameter (nm)
NbN	17	10
Ti _{0.2} Nb _{0.8} N	20	9

$\text{Ti}_{0.5}\text{Nb}_{0.5}\text{N}$	20	10
$\text{Ti}_{0.8}\text{Nb}_{0.2}\text{N}$	18	9
TiN	19	8

Table A3.5. Crystallite sizes from the Scherrer equation of gyroidal TiO_2 and various nitrides.

Composition	Crystallite size (nm)
TiO_2	8
TiN	7
$\text{Ti}_{0.8}\text{Nb}_{0.2}\text{N}$	6
$\text{Ti}_{0.5}\text{Nb}_{0.5}\text{N}$	5
$\text{Ti}_{0.2}\text{Nb}_{0.8}\text{N}$	5
NbN	5

Table A3.6. d_{100} -spacings and comparisons of samples at various stages of processing, from the SAXS patterns in Figure 3.3 and Figure 3.7.

Sample	Hybrid d_{100} spacing (nm)	Oxide d_{100} spacing (nm)	% of hybrid d_{100} spacing	Nitride d_{100} spacing (nm)	% of hybrid d_{100} spacing
ISO-69 $\text{Nb}_2\text{O}_5 \text{ G}^{\text{A}}$	50	40	80%	37	74%
ISO-93 $\text{Nb}_2\text{O}_5 \text{ G}^{\text{A}}$	64	46	72%	39	61%
ISO-93 $\text{Nb}_2\text{O}_5 \text{ G}^{\text{D}}$	124	97	78%	86	69%

CHAPTER 4

BLOCK COPOLYMER SELF-ASSEMBLY DIRECTED SYNTHESIS OF MESOPOROUS GYROID SUPERCONDUCTORS*

Abstract

Superconductors with periodically ordered mesoporous structures are expected to have very different properties compared to their bulk counterparts. Systematic studies of such phenomena to date are sparse, however, due to a lack of versatile synthetic approaches to such materials. Here we demonstrate the synthesis of three-dimensionally (3D) continuous and periodically ordered mesoporous niobium nitride (NbN) superconducting networks in a gyroid morphology. They are made from chiral ABC triblock terpolymer gyroid self-assembly directed sol-gel derived niobium oxide (Nb_2O_5) and subsequent thermal processing in air and flowing ammonia gas (NH_3). The resulting materials are characterized by a combination of small angle X-ray scattering and powder X-ray diffraction, scanning electron microscopy, nitrogen adsorption/desorption, room temperature conductivity and low temperature magnetization measurements. The superconducting materials exhibit a critical temperature, T_c , of about 8 K, a flux exclusion of about 5% compared to a dense NbN solid, and an estimated critical current density, J_c , of 440 A/cm^2 at 100 Oe and 2.5 K. Block copolymer directed self-assembly of mesoporous superconductors is expected to provide new avenues for mesostructure-superconductivity correlation studies.

* Robbins, S. W.; Sai, H.; Tan, K. W.; Beaucage, P. A.; Sethna, J. P.; DiSalvo, F. J.; Gruner, S. M.; van Dover, R. B.; Wiesner, U., *In Preparation*.

Introduction

Mesoscale structuring in the form of periodically ordered mesoporous arrays and different achiral or chiral mesoscale morphologies is expected to affect the properties of superconductors, including their critical field, critical current, and flux pinning behavior.¹⁻⁶ For example, pinning of superconducting vortex lines on the periodic mesostructure is expected to lead to commensurate-incommensurate transitions with applied magnetic field intensity, to angle dependent forces as the vortex lines align with the pore axes, and to vortex avalanches.⁷⁻⁹ The fact that superconductors can be thin compared to the magnetic penetration depth could lead to strikingly high maximum values for magnetic shielding.¹⁰ The chiral nature of some mesostructured superconductors will likely only couple weakly to the underlining superconducting pairing¹¹ but may give rise to unusual bulk material properties, especially coupling to magnetic fields, where the London penetration depth (*e.g.* 40 nm for Nb and 375 nm for NbN)^{12,13} is comparable to the mesopore lattice spacing. Finally, backfilling of mesopores with second material components should allow for leveraging the enormous surface areas to enhance interfacial superconductivity between non-superconducting constituents. Previously such studies have been restricted to planar interfaces between non-superconducting constituents, including metal-metal interfaces,¹⁴ metal-semiconductor interfaces,^{15,16} metal-insulator interfaces,¹⁷ semiconductor-semiconductor,^{18,19} and insulator-insulator interfaces.^{20,21} Mesostructured interfaces enable additional degrees of freedom to be introduced to the field of interfacial superconductivity: topology. Obviously, much of this is speculation, as no one has hitherto produced, *e.g.* a mesoporous superconducting material with a three-dimensionally continuous chiral cubic mesostructure. But the additional degrees of freedom then available, in terms of composition, morphology, and mesopore lattice constant, would beg investigation.

Despite growing interest in mesoscale science,²² to date few studies have pursued these kinds of phenomena. For example, there have been reports of a superconducting oxide asymmetric membrane with a mesoporous layer on a macroporous substrate²³ or of a sputtered superconducting Nb layer on a nanoporous Si substrate.²⁴ The sparsity of such studies is due, in part, to a lack of synthetic approaches to make mesostructured superconductors that would enable systematic investigations of mesostructure – superconductivity correlations. Block copolymer (BCP) self-assembly (SA) has proven to be a powerful tool to structure direct the composition, feature size, morphology, and porosity of various functional inorganic materials on the mesoscale.^{25,26} In principle, this structural control provides an ideal platform for tuning and studying mesostructural effects on superconducting properties of inorganic materials, but has not been exploited to date. To the best of our knowledge, the sole example in peer-reviewed literature involving block copolymers and superconductors describes the deposition of ferromagnetic/superconducting bilayers deposited on top of a diblock copolymer substrate.²⁷ In contrast, here we demonstrate how BCP SA can be used to structure direct a superconductor, niobium nitride (NbN), into a film of periodically ordered mesoporous material with networked three-dimensional (3D) mesostructure derived *via* heat treatments up to 850 °C from a BCP-inorganic hybrid precursor material with the alternating gyroid (G^A) morphology. This 3D mesoporous network exhibits a superconducting transition at 7.8 K. We expect this study to pave the way towards investigations of superconductors with a plethora of BCP SA directed mesostructures. Note that BCP SA is well suited to make structures of a given morphology with mesopore lattice constants ranging from tens to hundreds of nanometers by variation of the lengths of the copolymer.²⁸ This is expected to be of importance as the size ranges across length

scales specific to the superconducting component materials, such as the London penetration depth.

Results and Discussion

The triblock terpolymer poly(isoprene)-*block*-poly(styrene)-*block*-poly(ethylene oxide) (ISO) was used to structure direct sol-gel derived niobium oxide (Nb_2O_5) into a 3D alternating gyroid network structure by solvent evaporation-induced self-assembly (Figure 4.1).²⁹ BCP directed co-continuous cubic gyroid structures usually consist of two interpenetrating network sub-volumes related to one another by an inversion operation.³⁰ If these two minority networks are constituted by the same block (*e.g.* in AB diblock copolymers), the structure is referred to as a double gyroid (G^{D} , $Ia\bar{3}d$).³⁰ In the case pursued here where the two minority sub-volumes are made up of different blocks (*i.e.* the A and C end blocks in ABC triblock terpolymers; red and blue blocks/volumes in Figure 4.1) the resulting chiral structure is called the alternating (or single) gyroid (G^{A} , $I4_132$) and lacks an inversion center in its unit cell.³⁰ The chemical structures of the ISO terpolymer and inorganic sol-gel precursors used in this study are depicted in Figure 4.1 (left) together with a schematic of the synthesis approach and evolution of the alternating gyroid structure during different processing steps (right).

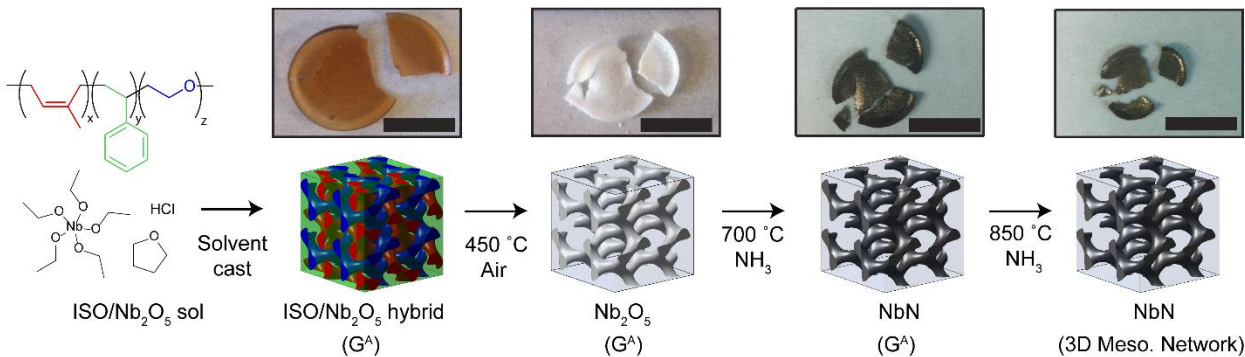


Figure 4.1. Chemical structures of compounds (left) and schematic of synthesis and processing steps (right) with photos of final materials (top). The block terpolymer ISO is combined with the Nb₂O₅ sol-gel precursors in a common solvent. The BCP/Nb₂O₅ hybrid alternating gyroid (G^A) structure is generated by solvent evaporation induced self-assembly. After calcination in air the mesoporous Nb₂O₅ G^A is transformed *via* a two-step nitriding process first to a NbN G^A and ultimately to a 3D mesoporous NbN network. Representation of the final NbN as a perfect G^A structure is for simplicity only (see text). Scale bars in all photographs represent 1 cm.

Superconducting NbN has been synthesized in the past by nitriding sol-gel derived Nb₂O₅ fibers.³¹ The resulting materials were not mesoporous and required nitriding temperatures of 1050 °C to exhibit superconductivity. Finding appropriate thermal treatments for block copolymer directed mesoporous inorganic materials is typically a balance between optimizing structure preservation by keeping temperatures low and materials property improvements by increasing processing temperatures. At 1050 °C, the mesostructure of the present BCP SA directed materials collapsed (see Figure A4.1). Lower nitriding temperatures of 600 °C, as used earlier,³² or even 700 °C, retained the mesostructure well but resulting materials showed no superconductivity. Overall, numerous heating profiles were explored to strike a balance between superconductivity and the retention of an ordered mesoporous structure. Ultimately, a two-step nitriding procedure described here consisting of first nitriding at 700 °C, then cooling to room temperature, and finally re-nitriding at 850 °C was necessary to successfully generate periodically ordered mesoporous nitrides that exhibited a superconducting transition. Interestingly, while nitriding in a single step at 850 °C in fact retained ordered mesoporosity, the resulting materials were not superconducting.

After solution casting and solvent evaporation at 50 °C, films were heat treated at 130 °C in a vacuum oven. The terpolymer was then removed by calcination in air at 450 °C, yielding freestanding single network alternating gyroidal mesoporous films of amorphous Nb₂O₅. The Nb₂O₅ alternating gyroids were converted into films of mesoporous superconducting niobium nitride (NbN) 3D network by heating under flowing ammonia gas (NH₃) in two steps, first to 700 °C and subsequently to 850 °C. For processing details the reader is referred to Materials and Methods. Photos of the materials at different processing steps are presented in Figure 4.1. They show that the as-made hybrids exhibit a yellow/brown color that disappears for the oxides upon calcination to 450 °C. Nitrided samples appear as black and shiny metallic solids. It is interesting to note that the materials remain close to their original shape with only a few cracks, rather than disintegrating into many pieces or even powders upon heat treatments.

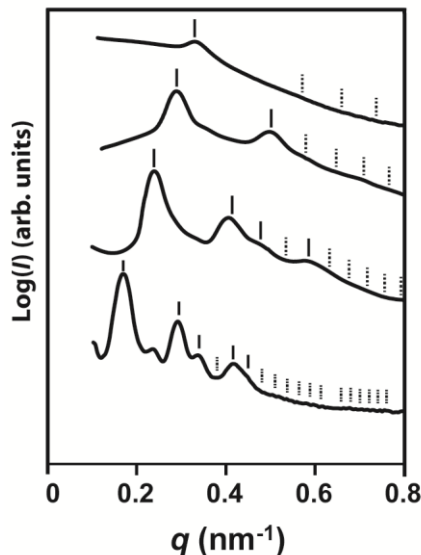


Figure 4.2. Small angle X-ray scattering patterns of samples at various processing stages. From bottom to top: ISO/oxide hybrid; Sample calcined at 450 °C in air; Sample nitrided at 700 °C; Sample nitrided at 850 °C. Observed (solid) and expected (dashed) peak positions for the alternating gyroid (G^A) structure are indicated by ticks above each curve.

Small angle X-ray scattering (SAXS) was used to characterize the mesostructural periodic order of the materials at various processing stages (Figure 4.2). The SAXS pattern for

the as-made BCP-oxide hybrid material (Figure 4.2, bottom) is consistent with the alternating gyroid morphology and a d_{100} -unit cell size of 52.3 nm. After calcining in air at 450 °C (Figure 4.2, second from bottom), the pattern remains consistent with the G^A morphology, but the peaks shift to higher q values and broaden, with a d_{100} -spacing of 37.2 nm. Peak broadening indicates some loss of long-range order of the mesoscale structure. The corresponding lattice shrinkage is typical during removal of organic material and condensation/crystallization of inorganic material in BCP-oxide systems.³³ After nitriding under NH₃ first at 700 °C and then at 850 °C, the SAXS patterns continue to shift to higher q values and to broaden (Figure 4.2, second from top and top). While for the 700 °C sample higher order reflections consistent with a G^A lattice can still be identified, the 850 °C sample only shows one reflection making structural lattice assignment by SAXS alone impossible. For comparison, assuming an alternating gyroid lattice for both samples the corresponding d_{100} -spacings from the first order reflections would be 30.7 nm and 27.0 nm.

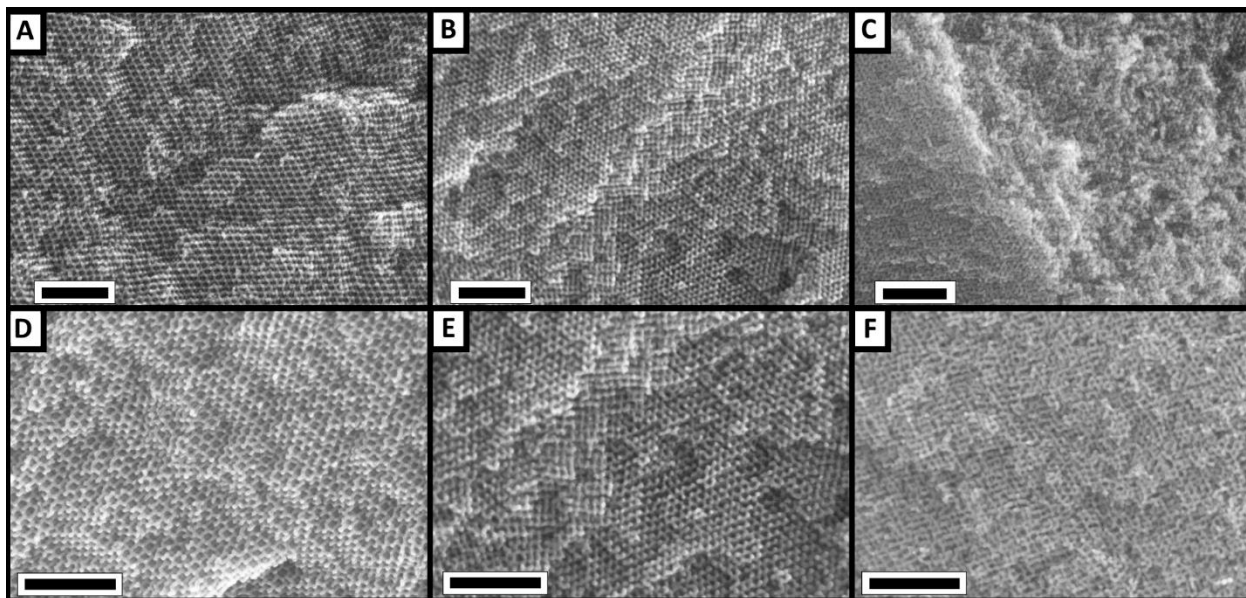


Figure 4.3. Scanning electron microscopy images of mesoporous samples at different processing stages. Periodically ordered gyroidal Nb₂O₅ (A, D) after calcination at 450 °C in air; Periodically ordered gyroidal NbN after nitriding at 700 °C (B, E) and after nitriding at 850 °C (C, F). All scale bars are 250 nm.

In order to corroborate the structural assignments from SAXS and to provide real space images of the structural sample evolution, scanning electron microscopy (SEM) was used to characterize the mesoscopic morphology of the materials obtained at different processing stages. In Figure 4.3 SEM images are shown of samples after calcining in air at 450 °C (Figure 4.3A,D), nitriding at 700 °C (Figure 4.3B,E), and after nitriding at 850 °C (Figure 4.3C,F). It is evident from Figure 4.3 that as the material progresses through the heat treatments and shrinks, it never completely loses its periodic order. Even though the overall order degraded relative to the samples treated at lower temperatures, this is also true for the sample heated at 850 °C for which a periodic 3D network morphology is still evident. Additional SEM images further supporting these conclusions are found in the Supporting Information (Figures A4.3-A4.6). Furthermore, as is apparent from these SEM images, the materials remained mesoporous throughout and did not structurally collapse, despite heat treatment up to 850 °C.

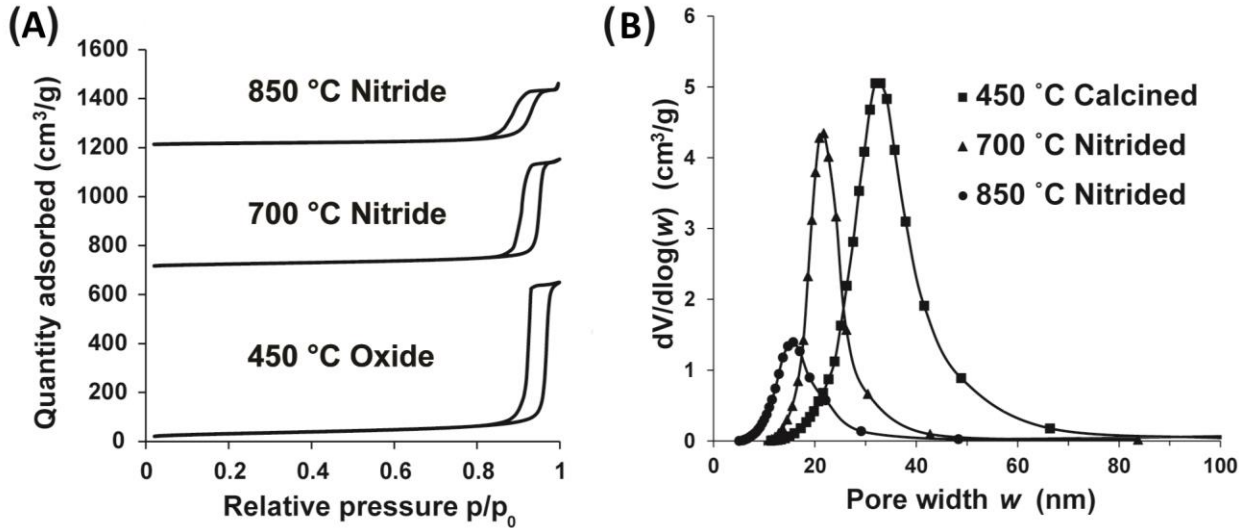


Figure 4.4. Materials porosity characterization from N₂ sorption measurements. N₂ adsorption/desorption isotherms (A) and pore size distributions (B) for 450 °C calcined, 700 °C nitrided, and 850 °C nitrided powder samples. For visibility, the isotherms of the 700 °C and 850 °C derived nitrides in (A) are offset by 700 cm³ g⁻¹ and 1200 cm³ g⁻¹ along the y-axis, respectively.

Materials porosity studies *via* N₂ sorption/desorption measurements were performed on powders of samples calcined at 450 °C, nitrided at 700 °C, and nitrided at 850 °C as shown in Figure 4.4A. All the isotherms in Figure 4.4A exhibit typical type-IV curves with H₁-type hysteresis.³⁴ In all cases, as expected, the surface area is dominated by mesoporosity rather than microporosity. In Figure 4.4B $dV/d\log(w)$ (where V is pore volume and w is pore width) *vs.* pore width is plotted for the three different samples showing a decrease in average pore sizes (as calculated from the BJH model – see Materials and Methods) from 31 nm to 21 nm to 16 nm with increasing temperature. Resulting surface areas and pore volumes are summarized in Table A4.1. Surface areas (as calculated from the BET model – see Materials and Methods) decrease from 111 m² g⁻¹ to 86 m² g⁻¹ to 59 m² g⁻¹, while pore volumes decrease from 1.01 cm³ g⁻¹ to 0.71 cm³ g⁻¹ to 0.41 cm³ g⁻¹ for samples treated to 450 °C, 700 °C, and 850 °C, respectively. These results are consistent with the observations of structural shrinkage from SAXS and SEM, and corroborate open and accessible mesoporosity for all samples. As an example, assuming a bulk density of 8.47 g cm⁻³ for the nitride and using the N₂ sorption derived pore volume, the sample treated at 850 °C had 77.5% porosity.

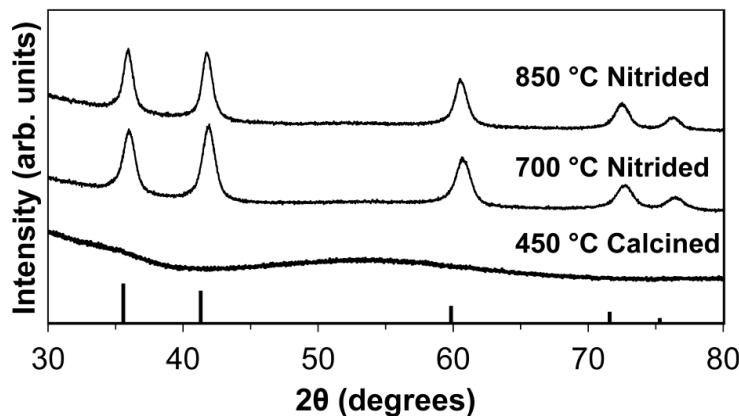


Figure 4.5. Powder X-ray diffraction patterns of samples calcined at 450 °C (bottom), and nitrided at 700 °C (middle) as well as 850 °C (top). For comparison, expected peak positions and relative intensities are indicated at the bottom for a cubic rock salt niobium nitride pattern (PDF Card # 04-008-5125).

The atomic crystal structure of the materials at different processing stages was characterized using wide-angle powder X-ray diffraction (XRD). As Figure 4.5 suggests, after the as-made BCP-oxide hybrid was calcined at 450 °C the resulting material was amorphous Nb₂O₅ (Figure 4.5, bottom). The XRD pattern in the middle of Figure 4.5 shows that nitriding at 700 °C for 12 h leads to material crystallization into a cubic rock salt structure characteristic of many binary metal nitrides, including NbN. From analysis of the XRD data, the cubic lattice parameter for this material is 4.31 Å, calculated from 2^*d_{200} ($2\theta \approx 42^\circ$) for the cubic structure. The crystallite size was estimated from the Scherrer equation and the average from all five peaks between 30 and 80 degrees was 7.2 nm, considerably smaller than the unit cell mesopore repeat. After further nitriding in the second step at 850 °C for 3 h (Figure 4.5, top), the material retained the rock salt structure but the lattice parameter increased to 4.33 Å and the crystallite size grew to 9.0 nm. The lattice parameter for the 850 °C nitrided sample is similar to that measured by Nomura *et al.* using the same nitriding temperature for macroscopic Nb₂O₅ fibers³¹ but is smaller than that of pure bulk cubic NbN.^{31,35} We attribute this difference in lattice parameter to residual oxygen content and anion vacancies. Interestingly, as noted earlier, in the work of Nomura *et al.* on NbN fibers, the rock salt structure was not observed until nitriding at 800 °C (and superconductivity was not observed until nitriding at 1050 °C).³¹ We attribute the ability to generate a cubic crystal structure in our mesostructured materials at lower temperatures to the porosity of the gyroidal Nb₂O₅ film and the resulting short solid-state diffusion lengths for oxygen and nitrogen atoms to reach a reactive solid-pore interface.

The conductivity of a networked film after the final nitridation at 850 °C was measured by a two point technique (detailed in Materials and Methods). The sample was found to have a

conductivity of 4.0 S/cm at room temperature, similar to values previously measured for mesoporous mixed transition metal nitrides that were generated by nitriding oxides.³²

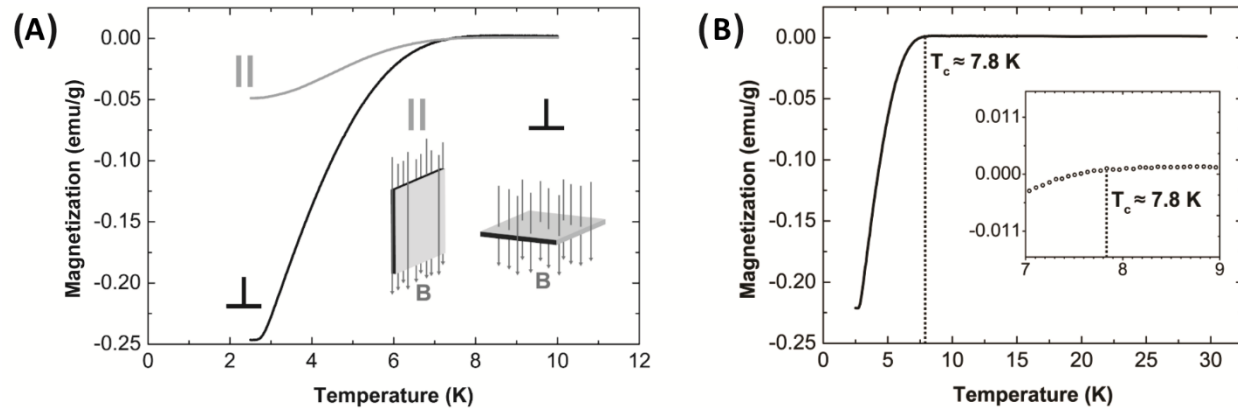


Figure 4.6. Magnetization behavior of samples nitrided to 850 °C. (A) Temperature dependent magnetization from 2.5 to 10 K for zero field cooled NbN films in a 200 Oe applied field with film long axis either parallel (top, \parallel) or perpendicular (bottom, \perp) to the applied field (see insets for different geometries tested). (B) Temperature dependent magnetization from 2.5 to 30 K for a zero field cooled NbN film with its long axis oriented perpendicular to a 70 Oe applied field. The inset in (B) shows the region of the superconducting transition temperature of approximately 7.8 K.

Finally, we characterized the magnetization behavior of the materials using a Quantum Design Physical Property Measurement System employing the Vibrating Sample Magnetometer setup. The temperature dependent magnetization was measured for rectangular prism samples of 850 °C nitrided materials oriented with their long axis either parallel or perpendicular to the applied magnetic field (Figure 4.6A). Samples were zero field cooled to 2.5 K, a 200 Oe field was applied, and the temperature swept to 10 K. Measurements in both geometries show a superconducting transition with a similar trend: a critical temperature, T_c , of 7.8 K and a broad transition down to 2.5 K. The observed T_c is below that of pure bulk NbN (16 K).^{31,35} Samples oriented with their long axis perpendicular to the applied magnetic field have larger demagnetization than the parallel-oriented samples, which is expected given the aspect ratio (~10) of the films. The perpendicular-oriented sample was also zero field cooled, a 70 Oe field was applied, and the temperature swept to 30 K to confirm the absence of changes between 10 K

and 30 K (Figure 4.6B). The inset of Figure 4.6B highlights the region between 7 and 9 K where the superconducting transition begins. Additionally, the parallel-oriented sample was zero field cooled to 2.5 K and its low field dependent magnetization was measured to determine the degree of flux exclusion and the critical current, J_c , of the material (See Figure A4.2). Interestingly, samples nitrided in single steps to only 700 °C or 850 °C did not exhibit a superconducting transition.

From the slope of the field dependent magnetization at low fields (Figure A4.2) and using the fractional density of the material calculated from the N₂ sorption data, the flux exclusion was calculated to be 5% compared to a dense, perfect superconductor with the same outer dimensions. This suggests that the flux lines are not perfectly excluded from the perimeter of the sample and may be passing through the mesopores. The critical current density, J_c , was estimated as 440 A/cm² at 100 Oe and 2.5 K. This relatively low value³⁵ may indicate weak links such as cracks or grains of weak superconductivity through the film thickness.

As noted above, the T_c of 7.8 K for the mesoporous superconducting material is below that of pure bulk NbN, which is around 16 K. It is known that non-stoichiometry, different crystal structures, oxygen content, atomic vacancies, and small feature sizes can all lower or suppress the T_c in niobium nitrides.^{31,36-41} The experimental T_c and lattice parameter for the superconducting mesoporous networked material studied here are consistent with values for a composition NbN_{1-x}O_y□_{x-y} (where □ represents anion vacancies) rather than highly stoichiometric δ-NbN.^{35,41-43} This is not surprising considering that the nitride precursor is Nb₂O₅ and that relatively low nitriding temperatures were employed.

For the present system, the nitriding temperatures necessary for generating superconducting materials (at least 850 °C) were in the same range in which loss of long-range

periodic order of the alternating gyroid mesostructure occurred. In future studies, as processing steps for block copolymer self-assembly directed mesoporous superconductors are optimized, we anticipate higher quality structural control for superconducting samples.

Conclusions

Block copolymer self-assembly is considered a hallmark of soft condensed matter physics. Due to structural versatility as well as precise tunability of morphology, dimensionality, and feature size, block copolymer self-assembly directed inorganic mesostructure formation is an ideal platform for studying periodically ordered mesostructural effects on superconducting properties. Generating such ordered mesoporous superconductors is not limited to niobium nitride nor to the particular synthetic strategy shown in this work. For example, block copolymer self-assembly could be used to tailor-make periodically ordered mesoporous superconductors *via* selective block etching and subsequent metal⁴⁴ or metal oxide⁴⁵ backfilling, or by block copolymer directed self-assembly of superconducting oxides. Furthermore, the resulting periodically ordered mesoporous superconductors could be coated or backfilled with different superconducting or non-superconducting materials to generate complex three-dimensional material interfaces. Moving forward, block copolymer self-assembly directed superconductors may provide a rich and fertile area for the study of superconductivity and the effects of periodic and chiral mesostructural order on superconducting properties.

Materials and Methods

Materials: Hydrochloric acid (37 wt%, ACS/NF/FCC), niobium(V) ethoxide (99.999%, metals basis), and tetrahydrofuran (anhydrous, ≥99.9%, inhibitor-free) were all used as received.

The block copolymer, poly(isoprene)-*block*-poly(styrene)-*block*-poly(ethylene oxide) (ISO), was synthesized by sequential anionic polymerization using known procedures.^{46,47} The block copolymer composition and polydispersity index (PDI) was characterized by a combination of size exclusion chromatography (GPC) and nuclear magnetic resonance (NMR). The ISO had an overall molar mass of 63.8 kg/mol and a PDI of 1.03. It was comprised of 18.7 kg/mol polyisoprene, 40.5 kg/mol polystyrene, and 4.6 kg/mol poly(ethylene oxide).

Synthesis of Mesoporous Niobium Nitride: 75 mg of ISO was dissolved in 2 mL anhydrous tetrahydrofuran (THF). The niobium oxide sol was prepared by a hydrolytic sol-gel route. First, 0.51 mL (2.03 mmol) of niobium(V) ethoxide was quickly added to 0.3 mL HCl in 1 mL of THF, and stirred vigorously in a 4 mL vial. After 5 minutes, 1 mL (12.33 mmol) THF was quickly added to the stirring vial. After 2 minutes, an aliquot of the transparent yellow sol was added to the polymer solution. The sol aliquot was 0.24 mL/75 mg ISO to generate an alternating gyroid morphology.

The ISO/oxide mixture was stirred vigorously for at least 3 hours. Films were then cast in PTFE dishes. The solvent was evaporated with the PTFE dish on a glass petri dish covered by a glass dome, on a hot plate set to 50 °C overnight. Films were subsequently aged at 130 °C for 2.5 h in a vacuum oven. To remove any closed layers on the polymer/oxide hybrid films, the films were treated with a CF₄ plasma in an Oxford PlasmaLab 80+ at 300 W for 40 minutes on each side of the film.

Films were calcined in air to generate freestanding mesoporous oxides in a flow furnace: ramped 1 °C/min to 450 °C and held for 3 hours at 450 °C, and allowed to cool to ambient temperature.

For nitriding the resulting oxides, films were heated in a flow furnace under anhydrous ammonia gas in two heating steps. In the first step, the oxide samples were heated under flowing ammonia gas at a flow rate of 2.5 L/h and a heating ramp rate of 350 °C/h to 700 °C, with a dwell time of 12 h at 700 °C. The tube was cooled to room temperature under flowing ammonia and purged with N₂. One tube valve was opened to air for 30 minutes, then the tube end was removed and the samples were removed from the tube. In the second step, samples were heated again under flowing ammonia gas at a flow rate of 2.5 L/h and a heating ramp rate of 350 °C/h to 850 °C, with a dwell time of 3 h at 850 °C. The tube was cooled to room temperature under flowing ammonia and purged with N₂. One tube valve was opened to air for 30 minutes, then the tube end was removed. Finally, samples were removed for characterization. The resulting freestanding mesoporous films were around 160 µm thick with lengths and widths around 5 mm.

Magnetization Characterization: Magnetization measurements were performed on a Quantum Design Physical Property Measurement System using the Vibrating Sample Magnetometer setup. For samples oriented with the large face perpendicular to the magnetic field, small flakes of the mesoporous films with a mass of 1-2 mg were mounted on a fused quartz cylinder using Lakeshore IMI-7031 low temperature varnish. The quartz cylinder was then loaded into a gold-coated brass half tube holder. For samples oriented with the large face parallel to the magnetic field geometry, flakes were mounted on a fused quartz paddle holder using Lakeshore IMI-7031 low temperature varnish. Samples were zero field cooled to 2.5 K. When the temperature stabilized, a magnetic field of 200 Oe was applied. The samples were then heated at a rate of 0.15 K/min from 2.5 K to 10 K while measuring the magnetic moment of the samples in the 200 Oe field.

For samples measured to 30 K in the perpendicular configuration, samples were zero field cooled to 2.5 K. Then a field of 70 Oe was applied and the temperature was swept at a rate of 0.5 K/min to 15 K, followed by 20 K/min to 300 K (only values from 2.5 to 30 K were plotted in Figure 4.6B).

XRD Characterization: Powder X-ray diffraction (XRD) data for the oxide and nitrides were collected on a Rigaku Ultima IV diffractometer equipped with a D/teX Ultra detector, using CuK α radiation and a scan rate of 2 °/min

SAXS Characterization: Small angle X-ray scattering (SAXS) patterns were obtained on either a custom-built beamline equipped with a Rigaku RU-3HR copper rotating anode generator, a set of orthogonal Franks focusing mirrors and a phosphor-coupled CCD detector, as described in detail elsewhere⁴⁸ or at the G1 station of the Cornell High Energy Synchrotron Source (CHESS) with a typical beam energy of 10.5 keV and sample-to-detector distance of 2.6 m or more. The two-dimensional patterns obtained from a point-collimated beam were azimuthally integrated to yield the one-dimensional plots shown in Figure 4.2. The oxide pattern was collected at CHESS while the as made hybrid and both nitride patterns were collected on the custom-built beamline.

SEM Characterization: Fractured and powdered monoliths samples were directly mounted on stubs using carbon tape. Oxide samples were coated with Au-Pd to increase conductivity while nitride samples required no coating. The samples were characterized by scanning-electron microscopy (SEM) on a TESCAN MIRA3 LM FE-SEM instrument and a Zeiss LEO-1550 FE-SEM using in-lens detectors.

Conductivity Characterization: After all heat treatments a piece of a nitride was used for a two point conductivity measurement. A portion of the sample's top surface was masked and Au-Pd coated to generate contacts. The mask was removed and drops of In-Ga liquid metal eutectic

were placed on the Au-Pd contacts. Resistance was measured across the known cross-section of the sample and was used to calculate conductivity. Mesoporosity was not taken into account in the conductivity calculations, which provide a lower bound for the conductivity of the sample.

N₂ Sorption Characterization: N₂ sorption characterization was performed on a Micromeritics ASAP 2020 surface area and porosity analyzer at -196 °C. The powdered samples were degassed at 120 °C under vacuum for at least 6 h prior to measurements. Surface areas were determined using the Brunauer-Emmett-Teller (BET) method⁴⁹ and pore size distributions were calculated employing the Barrett-Joyner-Halenda (BJH) method.⁵⁰

Acknowledgements

This work was supported as part of the Energy Materials Center at Cornell (EMC2), an Energy Frontier Research Center funded by the U.S. Department of Energy, Office of Science, Basic Energy Sciences under Award # DE-SC0001086. This work made use of the Cornell Center for Materials Research Shared Facilities, which are supported through the NSF MRSEC program (DMR-1120296). This work is based upon research conducted at the Cornell High Energy Synchrotron Source (CHESS), which is supported by the National Science Foundation and the National Institutes of Health/National Institute of General Medical Sciences under NSF award DMR-0936384. This work was performed in part at the Cornell NanoScale Facility, a member of the National Nanotechnology Infrastructure Network, which is supported by the National Science Foundation (Grant ECCS-0335765). H.S. was supported by the National Science Foundation (NSF) Single Investigator Award (DMR-1104773).

REFERENCES

1. Córdoba, R. *et al.* *Nat. Commun.* **2013**, *4*, 1437, doi: 10.1038/ncomms2437.
2. Piraux, L.; Hallet, X. *Nanotechnology* **2013**, *23*, 355301.
3. Welp, U. *et al.* *Physical Review B* **2002**, *66*, 212507.
4. Vanacken, J. *et al.* *Physica C: Superconductivity* **2008**, *468*, 585.
5. Lungu, A. *et al.* *Physica C: Superconductivity* **2001**, *349*, 1.
6. Hsu, Y. J.; Lu, S. Y.; Lin, Y. F. *Small* **2006**, *2*, 268.
7. Webb, R. A.; Voss, R. F.; Grinstein, G.; Horn, P. M., *Phys. Rev. Lett.* **1983**, *51*, 690.
8. Bean, C. P. *Phys. Rev. Lett.* **1962**, *8*, 250.
9. Bean, C. P. *Reviews of Modern Physics* **1964**, *36*, 31.
10. Tinkham, M., *Introduction to Superconductivity*. **1975**, (McGraw-Hill, New York).
11. Qi, X.-L.; Hughes, T. L.; Raghu, S.; Zhang, S.-C. *Phys. Rev. Lett.* **2009**, *102*, 187001.
12. Posen, S.; Catelani, G.; Liepe, M. U.; Sethna, J. P.; Transtrum, M. K. **2013**, *arXiv:1309.3239v2*.
13. Oates, D. E. *et al.* *Physical Review B* **1991**, *43*, 7655.
14. Brodsky, M. B. *Physical Review B* **1982**, *25*, 6060.
15. Burns, M. J.; Lince, J. R.; Williams, R. S.; Chaikin, P. M. *Solid State Commun.* **1984**, *51*, 865.
16. Akihama, R.; Okamoto, Y. *Solid State Commun.* **1985**, *53*, 655.
17. Gozar, A. *et al.* *Nature* **2008**, *455*, 782.
18. Murase, K. *et al.* *Surf. Sci.* **1986**, *170*, 486.
19. Fogel, N. Y. *et al.* *Physical Review B* **2006**, *73*, 161306.
20. Reyren, N. *et al.* *Science* **2007**, *317*, 1196.
21. Mannhart, J.; Schlom, D. G. *Science* **2010**, *327*, 1607.

22. U.S. Department of Energy Basic Energy Sciences, *From Quanta to the Continuum: Opportunities for Mesoscale Science* **2012**, <http://www.meso2012.com>.
23. Jang, E.-S. *et al.* *Chem. Mater.* **2007**, *19*, 3840.
24. Cirillo, C. *et al.* *Appl. Phys. Lett.* **2012**, *101*, 172601.
25. Smarsly, B.; Antonietti, M. *Eur. J. Inorg. Chem.* **2006**, *6*, 1111.
26. Orilall, M. C.; Wiesner, U. *Chem. Soc. Rev.* **2011**, *40*, 520.
27. Ruiz-Valdepeñas, L. *et al.* *J. Appl. Phys.* **2014**, *115*, 213901.
28. Urbas, A. M.; Maldovan, M.; DeRege, P.; Thomas, E. L. *Adv. Mater.* **2002**, *14*, 1850.
29. Templin, M. *et al.* *Science* **1997**, *278*, 1795.
30. Meuler, A. J.; Hillmyer, M. A.; Bates, F. S. *Macromolecules* **2009**, *42*, 7221.
31. Nomura, K.; Takasuka, Y.; Kamiya, K.; Nasu, H. *J. Mater. Sci.: Mater. Electron.* **1994**, *5*, 53.
32. Robbins, S. W.; Sai, H.; DiSalvo, F. J.; Gruner, S. M.; Wiesner, U. *ACS Nano* **2014**, *8*, 8217.
33. Toombes, G. E. S. *et al.* *Macromolecules* **2007**, *40*, 8974.
34. Sing, K. S. W. *Pure Appl. Chem.* **1985**, *57*, 603.
35. Martienssen, W.; Warlimont, H., *Springer Handbook of Condensed Matter and Materials Data.* **2006**, (Springer).
36. Storms, E. K.; Giorgi, A. L.; Szklarz, E. G. *J. Phys. Chem. Solids* **1975**, *36*, 689.
37. Lengauer, W. *Surf. Interface Anal.* **1990**, *15*, 377.
38. Gavalier, J. R.; Janocko, M. A.; Hulm, J. K.; Jones, C. K. *Physica* **1971**, *55*, 585.
39. Kang, L. *et al.* *J. Appl. Phys.* **2011**, *109*, 033908.
40. Patel, U. *et al.* *Appl. Phys. Lett.* **2007**, *91*, 162508.
41. Oya, G. I.; Onodera, Y. *J. Appl. Phys.* **1974**, *45*, 1389.
42. Terao, N. *Journal of the Less Common Metals* **1971**, *23*, 159.

43. Brauer, G. *Journal of the Less Common Metals* **1960**, *2*, 131.
44. Urade, V. N.; Wei, T.-C.; Tate, M.P.; Kowalski, J. D.; Hillhouse, H.W. *Chem. Mater.* **2007**, *19*, 768.
45. Crossland, E. J. *et al. Nano Lett.* **2008**, *9*, 2807.
46. Allgaier, J.; Poppe, A.; Willner, L.; Richter, D. *Macromolecules* **1997**, *30*, 1582.
47. Warren, S.; DiSalvo, F. J.; Wiesner, U. *Nat. Mater.* **2007**, *6*, 248.
48. Finnefrock, A. C.; Ulrich, R.; Toombes, G. E. S.; Gruner, S. M.; Wiesner, U. *J. Am. Chem. Soc.* **2003**, *125*, 13084.
49. Brunauer, S.; Emmett, P. H.; Teller, E. *J. Am. Chem. Soc.* **1938**, *60*, 309.
50. Barrett, E. P.; Joyner, L. G.; Halenda, P. P. *J. Am. Chem. Soc.* **1951**, *73*, 373.

APPENDIX 3

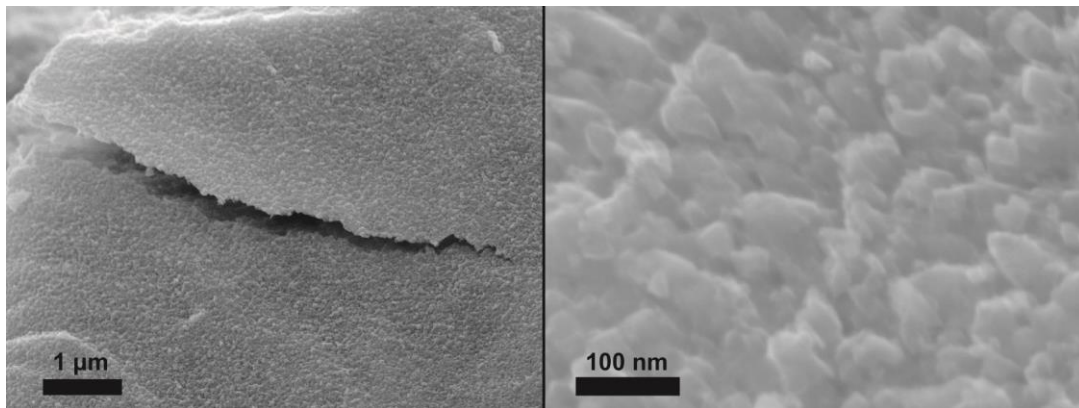


Figure A4.1. Cross-sectional SEM images of material nitrided in one step at 1050 °C. The ordered mesoporosity is lost as the structure collapses under the high temperature nitriding conditions.

Table A4.1. Surface area and pore volume, as measured by N₂ sorption, of materials at different stages of thermal processing.

Sample	Surface Area (m ² /g)	Pore Volume (cm ³ /g)
450 °C Calcined	111	1.01
700 °C Nitrided	86	0.71
850 °C Nitrided	59	0.41

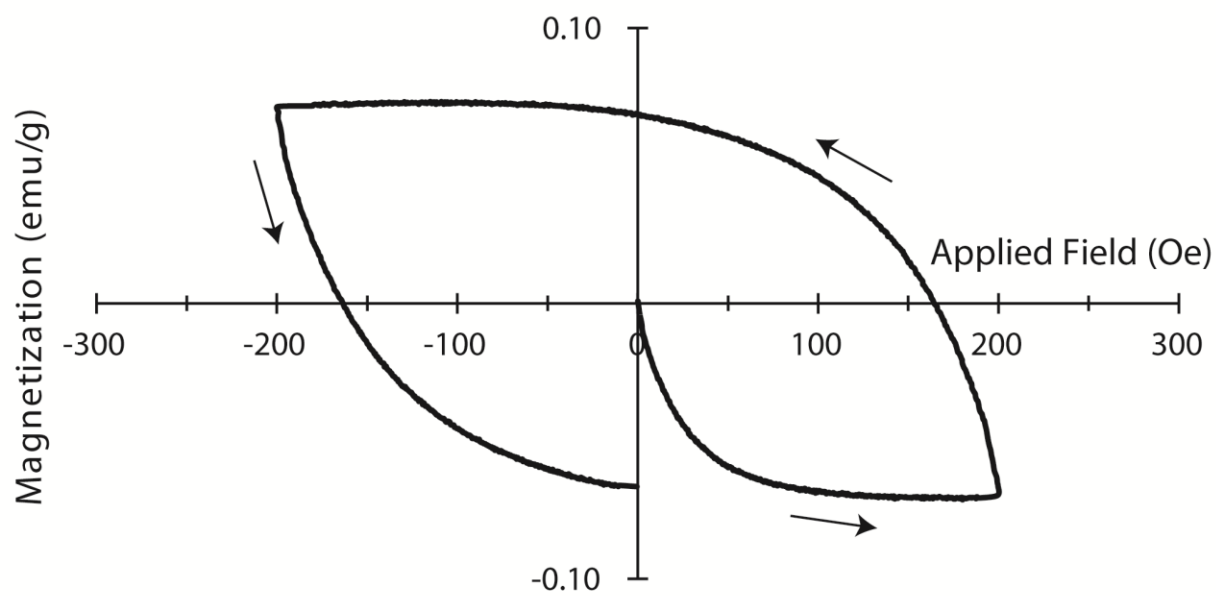


Figure A4.2. Field-swept magnetization behavior of 3D mesoporous NbN material heat treated to 850 °C. The field was swept from 0 Oe to 200 Oe, then from 200 Oe to -200 Oe and finally from -200 Oe to 0 Oe. The linear slope at low fields was used to calculate the flux exclusion and ΔM at 100 Oe was used to calculate the critical current density, J_c , using the Bean model.

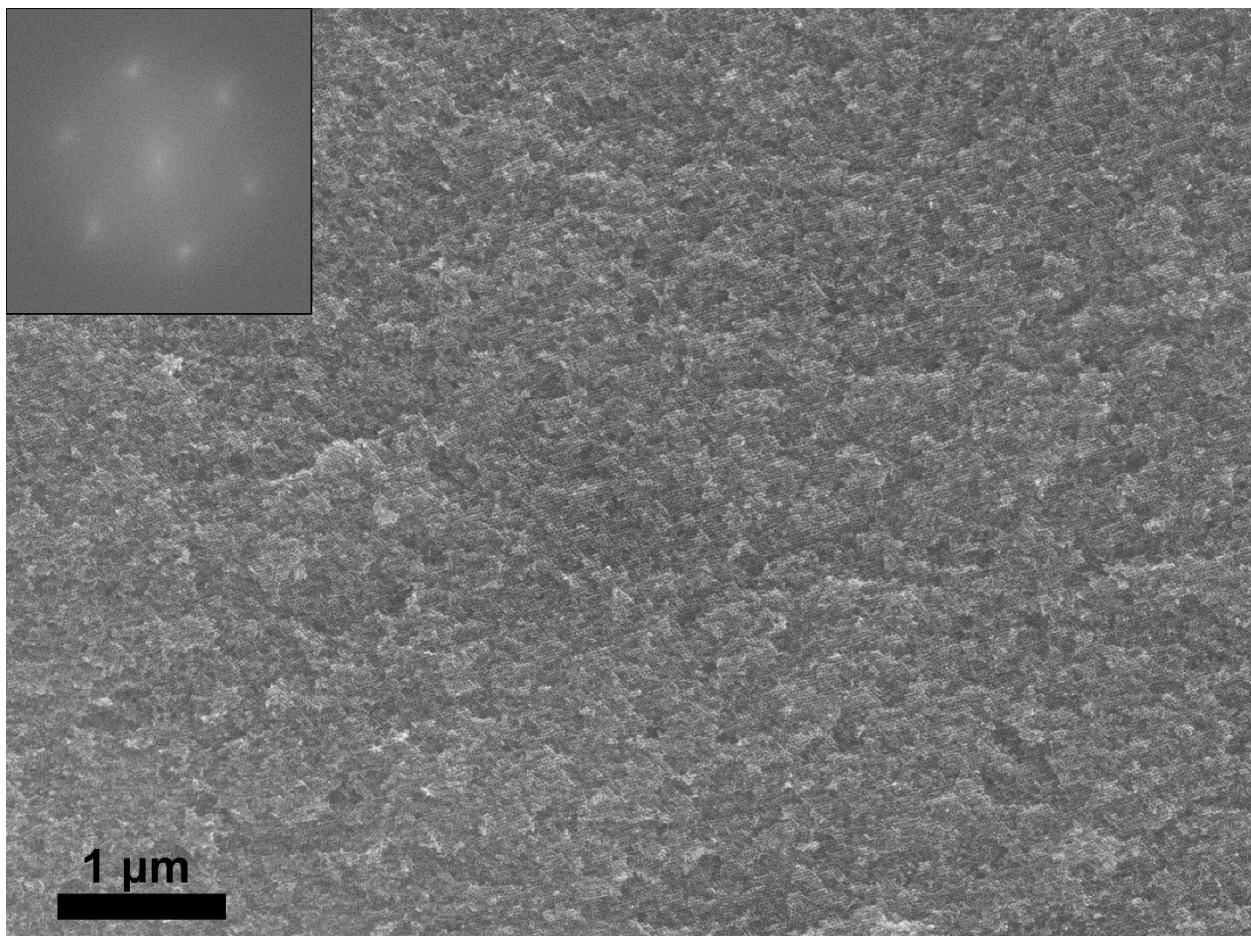


Figure A4.3. Cross-sectional SEM image of a monolith after final 850 °C nitriding. The inset is an FFT of a large square portion of the image, showing a sixfold pattern.

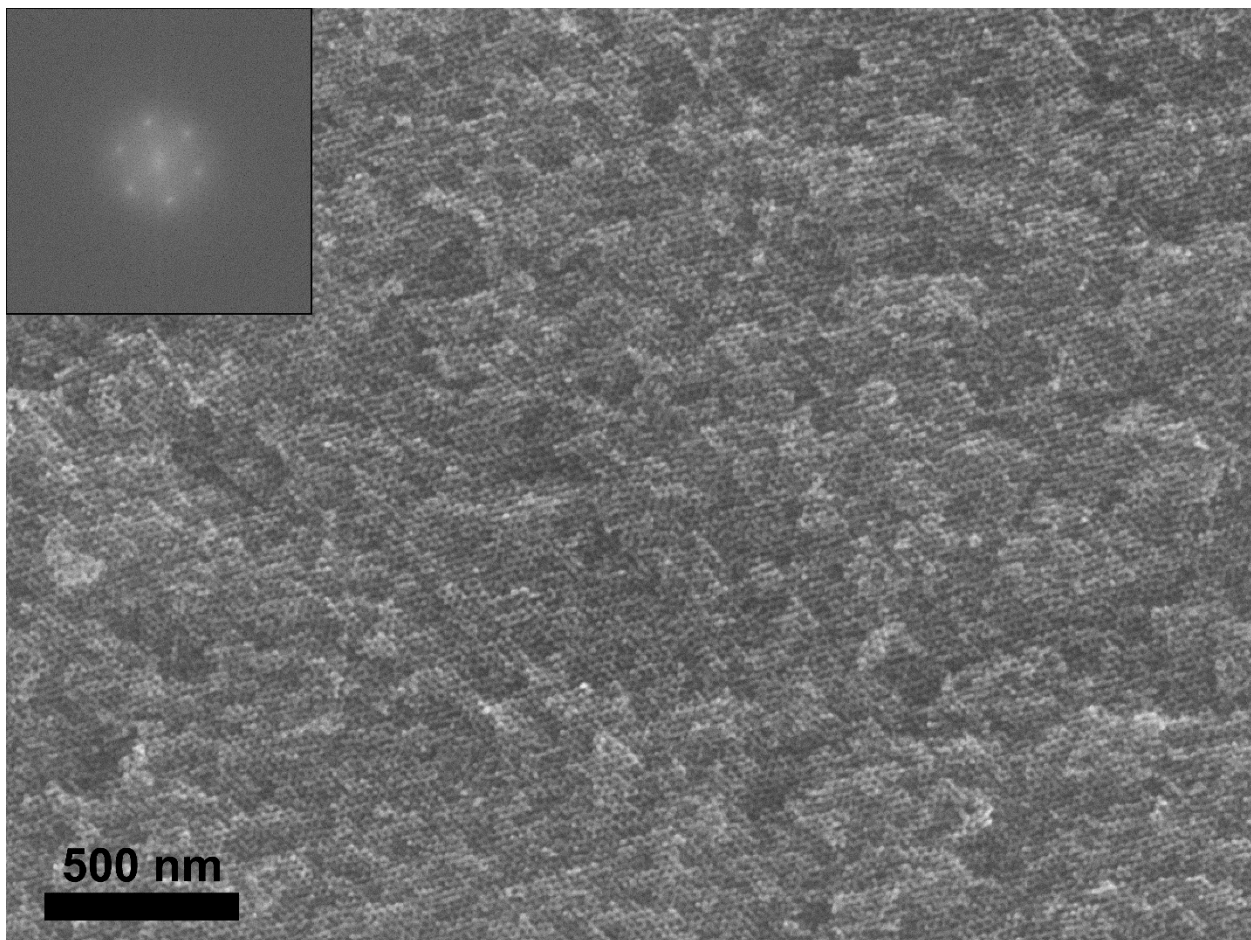


Figure A4.4. Cross-sectional SEM image of a monolith after final 850 °C nitriding. The inset is an FFT of a large square portion of the image, showing a sixfold pattern.

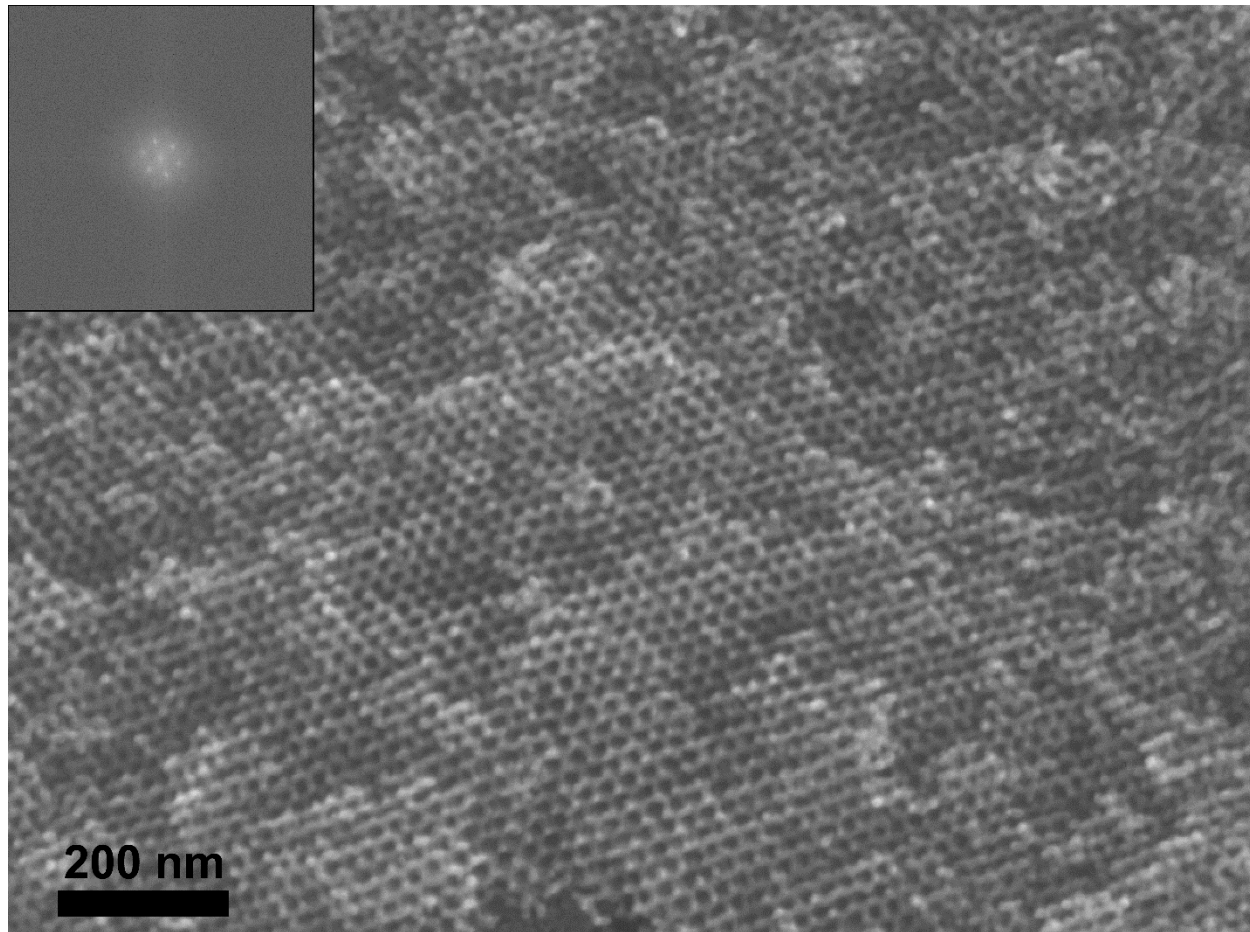


Figure A4.5. Cross-sectional SEM image of a monolith after final 850 °C nitriding. The inset is an FFT of a large square portion of the image, showing a sixfold pattern.

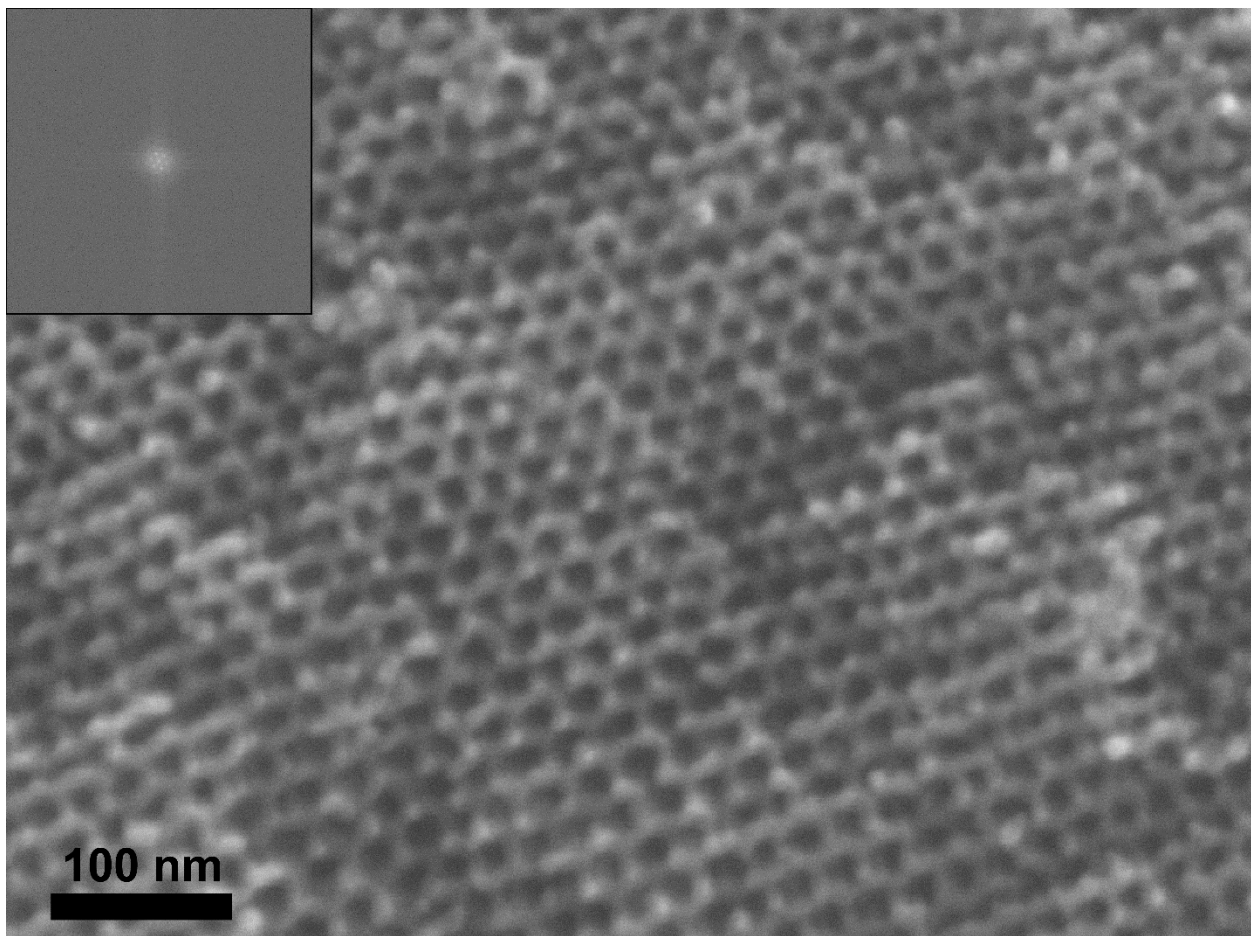


Figure A4.6. Cross-sectional SEM image of a monolith after final 850 °C nitriding. The inset is an FFT of a large square portion of the image, showing a sixfold pattern.

CHAPTER 5

GYROIDAL MESOPOROUS ANTIMONY-DOPED TIN OXIDE FROM SELF-ASSEMBLY OF CRYSTALLINE NANOPARTICLES AND A TRIBLOCK TERPOLYMER

Abstract

Conducting inorganic ordered mesoporous networks are of interest for improving energy conversion and storage applications. Block copolymer directed nanoparticle self-assembly is a powerful tool for generating inorganic nanostructures including cubic gyroid morphologies. These gyroid structures are desirable for energy applications where continuous pathways in both the inorganic and porosity conduct electrons and electrolytes, respectively. The use of crystalline rather than amorphous metal oxide nanoparticles is a strategy to access crystalline mesoporous networks without loss of the network structure from high temperature annealing protocols. Here, we report the self-assembly of crystalline antimony-doped tin oxide (ATO) nanoparticles with the amphiphilic triblock terpolymer poly(isoprene)-*block*-poly(styrene)-*block*-poly(ethylene oxide) (ISO), resulting in a hybrid film with the alternating gyroid (G^A) morphology. Calcination of the hybrid at 550 °C leaves a freestanding crystalline ATO alternating gyroid structure. This ordered mesoporous transparent conducting oxide material may find application in optoelectronics or energy conversion and storage.

* Robbins, S. W. †; Lechêne, B. P. †; Sai, H.; Tan, K.W.; DiSalvo, F. J.; Gruner, S. M.; Stefik, M.; Wiesner, U., *In Preparation*. †These authors contributed equally.

Introduction

Antimony-doped tin oxide (ATO) has been investigated as a cheaper transparent conducting oxide (TCO) for optoelectronics compared to indium tin oxide (ITO).¹⁻⁷ In ATO, conductivity is maximized at antimony concentrations below 20 mol% of the metal atoms⁴⁻⁷ whereas in ITO, indium often exceeds 80 mol% of the metal atoms.³ Indium oxide is a more costly component than tin oxide or antimony oxide, making ATO an attractive material for devices. Mesostructuring TCO electrodes in a device is desirable to maximize the interface between the TCO and active material which in turn minimizes the transport distance for the electrons from active material to electrode.⁸⁻¹² Generating a highly porous three-dimensional (3D) bicontinuous mesostructure is ideal for maximizing interfacial surface area between TCO and active material while ensuring a continuous pathway for electrons.⁸ A unique feature of network morphologies, not found in common sphere-based morphologies, is the relatively constant structural diameter that minimizes the amount inorganic used while simultaneously lowering the optical losses to absorption.

Crystallinity is also desirable in mesoporous nanostructures. Using crystalline building blocks is one strategy to achieve this, particularly while allowing for less harsh processing temperatures of material that may otherwise result in collapse of the mesoporosity.¹³ Consequently, nanocrystalline ATO synthesized by the benzyl alcohol route has been used as building blocks of ATO mesostructures.⁵ The benzyl alcohol route^{14, 15} is useful for generating ATO nanocrystals⁴ due to the ability to control particle growth and size, as well as provide uniform doping and generate crystalline materials at modest temperatures.¹⁵ Amphiphilic block copolymers (BCPs) have

proven powerful and versatile tools for structure-direction of highly ordered mesoporous crystalline metal oxides.^{13, 16} A key challenge combining crystalline oxide building blocks with BCP structure-direction is the solubility of these nanocrystals in an organic solvent which is also compatible with the amphiphilic block copolymers. The particles must be small and dispersible in the organic solvent without the use of a bulky ligand which can interrupt the particle's ability to selectively incorporate into the hydrophilic block of the amphiphilic BCP.^{17, 18} While tetrahydrofuran (THF) dispersible ATO nanocrystals have been reported in the literature,⁷ crystalline ATO particles have not been used to generate highly ordered 3D mesostructures with large amphiphilic BCPS.

The aforementioned challenges are generally not an issue for smaller Pluronic-type polymer systems which have been used to generate mesoporous ATO.^{5, 19} However, there have been just two reports using larger non-Pluronic amphiphilic AB diblock⁶ and ABA triblock²⁰ copolymers to generate ordered mesoporous ATO but both used amorphous sol-gel precursors resulting in thin films without a highly ordered 3D structure and did not use ABC triblock terpolymers. Using larger amphiphilic triblock terpolymers allows tunable structure-direction of larger feature sizes and increased thermal stability⁹ as well as enabling more complex morphologies for the final ordered mesoporous oxide compared to Pluronics or diblocks.¹³ One such complex morphology in triblock terpolymer systems is the alternating gyroid (G^A): a chiral tricontinuous three-dimensionally networked structure.²¹ A mesoporous G^A is an attractive morphology for a TCO electrode due to its high porosity and 3D continuity,

where electrons have a continuous path through the oxide, as well as high interfacial surface area to contact the next material of a device.²²

We report a G^A structure of ATO, through the use of crystalline ATO particles and their coassembly with the amphiphilic triblock terpolymer poly(isoprene)-*block*-poly(styrene)-*block*-poly(ethylene oxide) (ISO). The ATO nanocrystals were synthesized by a benzyl alcohol route modified from reports in the literature.^{4, 7} The molar concentration of [Sb]/[Sn + Sb] was around 6%, in the range to maximize conductivity of the oxide.⁴⁻⁷ The solution of metal chlorides (SnCl₄ and SbCl₃) in benzyl alcohol was heated to form the ATO nanocrystals. After precipitation in toluene, the particles were readily dispersible in THF in concentrations exceeding 15 mg/mL. An aliquot of THF dispersed particles was added to a solution of the block terpolymer ISO in THF. The hydrophilic oxide particles selectively hydrogen bond to the hydrophilic poly(ethylene oxide) (PEO) block of ISO. Through a process of evaporation-induced self-assembly,^{23, 24} the BCP self-assembles along with the oxide particles, into an ordered mesoscale morphology. The BCP can subsequently be removed by calcination, leaving a freestanding ordered mesoporous structure. In this work, the ISO/oxide hybrid was a G^A where the PEO/ATO domain forms one of the two gyroid minority networks. After calcination in air at 550 °C, the polymeric material is removed, leaving a freestanding single ATO G^A network. The steps of the synthesis are shown schematically in Figure 5.1.

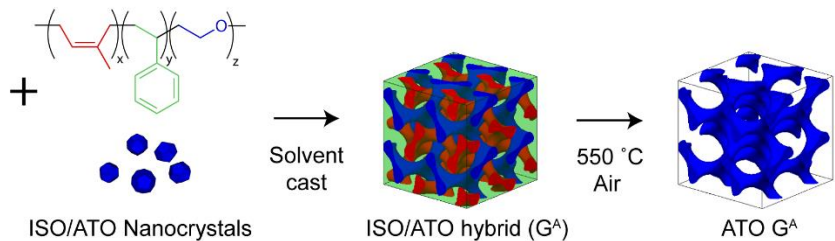


Figure 5.1. Schematic of the synthesis of alternating gyroid (G^A) ATO using poly(isoprene)-*block*-poly(styrene)-*block*-poly(ethylene oxide) (ISO) as structure directing agent. The ATO nanocrystals and BCP are mixed in an organic solvent, and coassemble into a hybrid with a G^A structure. Finally, calcination in air yields the freestanding G^A ATO.

Results and Discussion

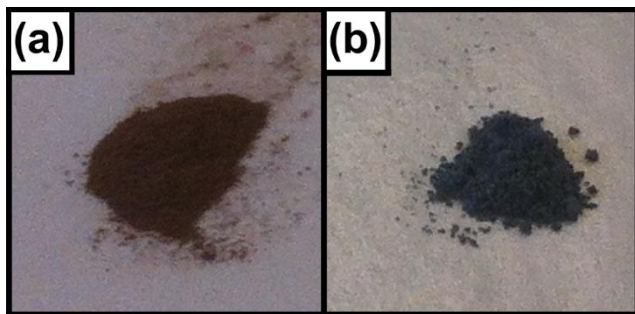


Figure 5.2. Photographs of (a) dried ATO particles and (b) ground powder of G^A ATO after calcination in air.

Photographs of the as-made particles and calcined BCP structure-directed ATO are shown in Figure 5.2. The as-made ATO particles are an orange-brown powder after drying, consistent with what has been reported.⁴ In contrast, undoped tin oxide is a pure white powder and the strong color in the ATO particles indicates the doping of antimony into tin oxide.⁴ After calcination and grinding, the mesostructured material is a bluish-grey powder and this coloration is due to mixed oxidation states of Sb^{III} and Sb^V in the ATO.^{25, 26}

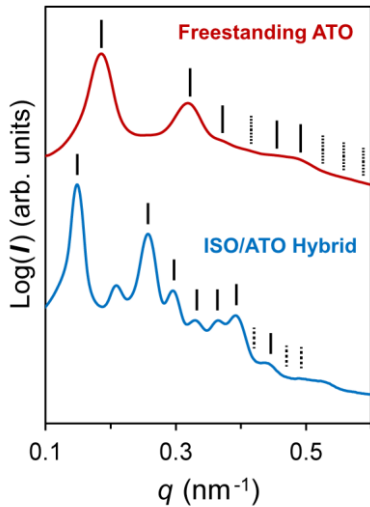


Figure 5.3. Small angle X-ray scattering patterns of the as-made ISO/ATO hybrid (bottom, blue), and freestanding mesoporous ATO (top, red) after calcination. Solid lines mark expected and observed peak positions for the G^A structure and dashed lines represent expected but unobserved peak positions for the G^A structure.

In order to study the mesoscale ordering and how it changes after calcination, small-angle X-ray scattering (SAXS) patterns were collected for the as-made ISO/ATO hybrid film and freestanding ATO after calcination. The SAXS pattern (Figure 5.3, bottom) obtained for the hybrid film is consistent with the alternating gyroid (G^A) structure, indicated by lines for expected peak positions for a G^A morphology at $(q/q_{100}^*)^2 = 2, 6, 8, 10, 12, 14$, and 16 (Figure 5.3). The best fit d_{100} spacing for the G^A structure is 60 nm. The small peak between the first two marked peaks is a forbidden peak that appears due to broken symmetry. We have observed this previously in other ISO/oxide systems and it is attributed to compression in the z -axis during film casting.^{22, 27, 28} The sharp peaks and the presence of numerous higher order reflections suggest a highly ordered structure with long range order.

After calcination, the sample undergoes several notable changes in the SAXS pattern. First, the d_{100} spacing shifts to higher q , indicating a shrinkage in the structure,

as expected during polymer removal. The d_{100} spacing changes from 60 nm in the as-made hybrid to 48 nm in the freestanding calcined ATO material, a shrinkage of 20%. Second, the SAXS peaks broaden from the hybrid to the freestanding oxide, indicating a less well-defined scattering interface. The distinct nanocrystals comprising the mesostructure causing surface roughness may contribute to this effect. Finally, some higher order peaks of the hybrid disappear in the calcined material, indicating loss of long-range mesoscale ordering which is also typical in heat treatments of BCP/oxide materials. However, the calcined material shows three peaks that are consistent with, though not conclusive of the G^A structure after the polymer is removed during calcination, suggesting the retention of the ordered structure.

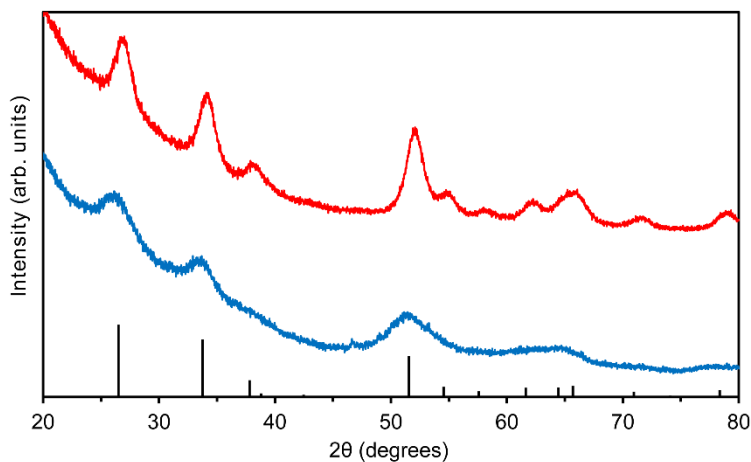


Figure 5.4. Powder X-ray diffraction patterns of the as-made ATO particles (bottom, blue) and calcined ATO G^A material (top, red). The expected peak positions and relative intensities for the SnO_2 cassiterite structure (PDF card 04-008-8130) are shown on the x-axis.

In order to verify the crystallinity of the ATO particles and the calcined ATO gyroid structure, powder X-ray diffraction (XRD) was used (Figure 5.4). Dried powder of the ATO particles was measured and shows the major reflections for the cassiterite SnO_2 structure, as expected. The crystallite size for the as-made particles

was estimated from the first two reflections ($2\theta \approx 27^\circ, 35^\circ$) to be 3 nm by the Scherrer equation. After calcination of the ATO/ISO hybrid at 550 °C in air, the peaks in the XRD pattern somewhat sharpen, and the crystallite size as estimated from the Scherrer analysis using the first two reflections increases to 5 nm. From the broad XRD peaks, it is unclear whether the increased crystallite size results from coalescing nanocrystals or any residual amorphous content crystallizing.

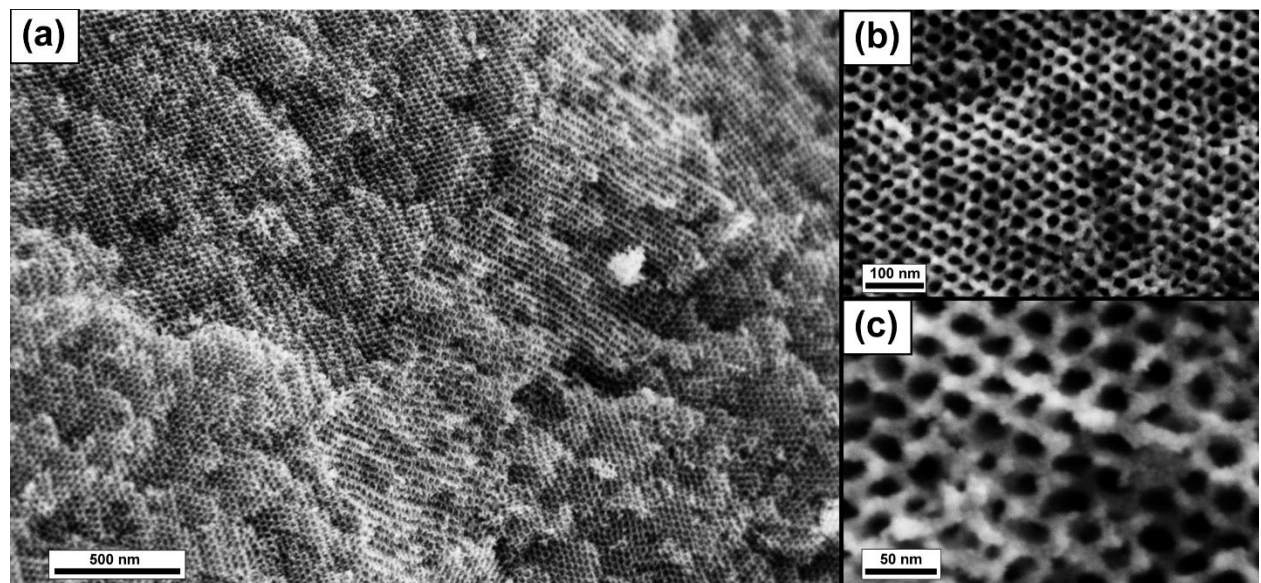


Figure 5.5. Scanning electron microscopy images of freestanding G^A ATO at various magnifications.

The mesostructure of the gyroidal mesoporous ATO was further investigated by scanning electron microscopy (SEM). Flakes of the calcined ATO were fractured on carbon tape mounted on stubs and were imaged without any conductive coating. As demonstrated in Figure 5.5 the samples are clearly mesoporous and a 3D ordered structure can be recognized, which is consistent with the networked G^A structure. As measured by SEM, the pores are around 19 nm, while the struts have a diameter of

about 9 nm. The SEM data are in good agreement with the patterns that were observed by SAXS which indicate the G^A structure. In particular in images at higher magnification (Figure 5.5c) it is interesting to note the roughened surface of the gyroidal struts, presumably from the nanocrystals comprising the network structure.

For measurement of the conductivity of the gyroidal mesoporous ATO, a film cast using freestanding gyroidal mesoporous ATO in combination with a binder was calcined, as described in the experimental section. The conductivity of the calcined film was subsequently measured by a four point probe setup and was found to be 4 x 10⁻² S/cm. This conductivity is low compared to what has been reported for other ordered mesoporous ATO.^{6, 20} This disparity may be due to high surface area and surface area to volume ratio of the gyroid increasing surface scattering.⁹ Furthermore, dramatic variations in conductivity for ATO have been reported in the literature through different doping levels or heating conditions⁵⁻⁷ and BCP:ATO ratios.²⁰

We have demonstrated the synthesis of antimony-doped tin oxide (ATO) with alternating gyroid (G^A) structure using self-assembly of a triblock terpolymer with crystalline ATO nanoparticles. To the best of our knowledge, this work represents the first report of a gyroidal structure achieved using crystalline nanoparticle building blocks. The material shows good thermal stability during calcination, retaining the 3D G^A structure and exhibits moderate conductivities. Using crystalline building blocks may prove a useful synthetic strategy for generating highly crystalline gyroidal structures. In particular, we expect using crystalline particles in combination with amorphous sol-gel material in a “brick-and-mortar” type synthesis²⁹ to provide even

greater tunability of the performance such as conductivity in these highly ordered systems using BCP-oxide self-assembly.

Experimental

Antimony(III) chloride (99.99%), tin(IV) chloride (99.999%), benzyl alcohol (99.8%, anhydrous), and tetrahydrofuran (anhydrous, inhibitor-free) were purchased from Sigma-Aldrich and used as received. Toluene (ACS grade) from J.T. Baker was used as received.

The block copolymer, poly(isoprene)-*block*-poly(styrene)-*block*-poly(ethylene oxide) (ISO), was synthesized *via* sequential living anionic polymerization as described in detail elsewhere.³⁰ The block copolymer had a composition of 17.75 kg/mol poly(isoprene), 37.45 kg/mol poly(styrene), and 4.48 kg/mol poly(ethylene oxide), with a total number average molar mass, M_n , of 59.68 kg/mol and a polydispersity index of 1.09. This composition corresponds to 33.3 vol% poly(isoprene), 60.2 vol% poly(styrene), and 6.5 vol% poly(ethylene oxide).

The ATO particles were obtained by the benzyl alcohol route using syntheses modified from literature procedures.^{4, 7} ATO particles were synthesized in a 75 mL glass pressure vessel sealed with an O-ring and a PTFE cap. In a glovebox with a N₂ atmosphere, 58 mg (0.25 mmol) of SbCl₃ were placed in the pressure vessel with a stirbar. In the glovebox, the SbCl₃ was dissolved in 30 mL of benzyl alcohol and was stirred for at least 15 min. Next, 0.48 mL (4.10 mmol) of SnCl₄ was added very slowly, dropwise, under vigorous stirring. The reaction of SnCl₄ with benzyl alcohol is violent, so caution must be taken, ensuring very slow addition of the SnCl₄! The pressure vessel was sealed and removed from the glovebox.

The pressure vessel was placed in an oil bath at 145 °C, stirring at 710 rpm. The vessel was heated while stirring for 45 minutes. As a precaution, the reaction should be

shielded. After 45 minutes, the vessel was removed from the oil bath and allowed to cool in air to ambient temperature. The solution/dispersion is orange and totally translucent, with a small amount of solid above the liquid line. The vessel was allowed to sit overnight. Finally, the liquid contents of the vessel were slowly precipitated into 70 mL of toluene total (split between two centrifuge tubes). The fluffy orange precipitate was centrifuged at 5000 rpm (11.5 cm rotor radius) for 10 min at 20 °C. The remaining clear liquid was decanted. The solids were immediately dispersed in 15 mL total of anhydrous tetrahydrofuran (THF). The particles readily formed a translucent deep orange dispersion. The particles were sonicated for 1 hour and allowed to sit overnight.

The concentration of ATO in THF was determined by drying and weighing an aliquot of the dispersion and was found to exceed 15 mg/mL. Thermogravimetric analysis of dried particles showed approximately 15 wt% organic content on the particles. This information was used to calculate the amount of the ATO dispersion to add to the BCP to achieve a G^A structure.

To prepare the ISO/ATO hybrids, first 100 mg of ISO was dissolved in 3 mL anhydrous THF. Next, 2 mL of the ATO dispersion was added to the ISO solution and stirred at least 30 min. The ISO/ATO in THF was placed in a PTFE dish that was placed on a crystallization dish covered with a glass hemisphere. The ISO/ATO hybrid film was cast by placing the crystallization dish on a 50 °C hot plate overnight, evaporating off the solvent and self-assembling the ordered structure. The film was subsequently aged in a vacuum oven at 100 °C overnight.

To generate the freestanding mesoporous ATO, the film was calcined in a tube furnace in air: ramped at 10 °C/min and held at 550 °C for 1 h to remove the block copolymer and sinter the oxide particles.

We note that while the material shown in this work were prepared using ATO synthesized in a pressure vessel in an oil bath, a pressure vessel is not necessary. ATO can be prepared analogously using PTFE-capped vials and an aluminum heating block on a hot plate, which we found to be a simpler setup.

SAXS Characterization: Small angle X-ray scattering data for the ISO/ATO hybrid was collected at the G1 station of the Cornell High Energy Synchrotron Source (CHESS) with a beam energy around 10.5 keV and a sample-to-detector distance of around 2.5 m. The data for the calcined ATO was collected on a home-built beamline with a Rigaku RU-3HR Cu rotating anode, orthogonal Franks focusing mirrors, and a phosphor-coupled CCD detector, detailed elsewhere.³¹ Two-dimensional patterns were azimuthally integrated to obtain the one-dimensional plots shown in Figure 5.3.

XRD Characterization: Powder X-ray diffraction measurements were performed on a Rigaku Ultima IV diffractometer equipped with a d/Tex Ultra detector and using Cu K α radiation and a scan rate of 5°/min.

SEM Characterization: Flakes of the G^A ATO were mounted on stubs using carbon tape and did not require any coating for imaging. Images were acquired on a Zeiss LEO-1550 FE-SEM using the in-lens detector with a 3 kV accelerating voltage.

Conductivity: Freestanding calcined ATO was mixed with 2 wt% poly(vinylidene fluoride) in N-methyl-2-pyrrolidone giving 15 wt% ATO total in the mixture. The material was ball milled for 3 minutes to generate a slurry. The slurry was doctorbladed onto a glass slide with

a gate height of 200 μm . The film was dried under vacuum at 80 °C. To remove the binder, the film was calcined at 450 °C in air. Conductivity measurements were performed on a 4 point probe system with a Cascade Microtech CPS-06 using tungsten carbide probes and a Keithley 2400 SourceMeter.

Acknowledgements

This work was supported as part of the Energy Materials Center at Cornell (EMC2), an Energy Frontier Research Center funded by the U.S. Department of Energy, Office of Science, Basic Energy Sciences under Award # DE-SC0001086. This work made use of the Cornell Center for Materials Research Shared Facilities, which are supported through the NSF MRSEC program (DMR-1120296). This work is based upon research conducted at the Cornell High Energy Synchrotron Source (CHESS), which is supported by the National Science Foundation and the National Institutes of Health/National Institute of General Medical Sciences under NSF award DMR-1332208. H.S. was supported by the NSF Single Investigator Award (DMR-1104773). M.S. was supported by USC startup funds. M.S. thanks Markus Niederberger for the helpful discussions regarding nanoparticle solubility. S.W.R. thanks J.G. Werner for help with the conductivity.

REFERENCES

1. Shanthi, E.; Dutta, V.; Banerjee, A.; Chopra K. L. *J. Appl. Phys.* **1980**, *51*, 6243.
2. Elangovan, E.; Ramamurthi K. *Appl. Surf. Sci.* **2005**, *249*, 183.
3. Minami, T. *Thin Solid Films* **2008**, *516*, 5822.
4. Müller, V. *et al. Chem. Mater.* **2009**, *21*, 5229.
5. Müller, V. *et al. Small*, **2010**, *6*, 633.
6. Wang, Y.; Brezesinski, T.; Antonietti, M.; Smarsly, B. *ACS Nano* **2009**, *3*, 1373.
7. Conti, T. G.; Chiquito, A. J.; Da Silva, R. O.; Longo, E.; Leite, E. R.; *J. Am. Ceram. Soc.* **2010**, *93*, 3862.
8. Fattakhova-Rohfing, D. *et al. Adv. Mater. (Weinheim, Ger.)* **2006**, *18*, 2980.
9. Till von, G. *et al. Science and Technology of Advanced Materials*, **2011**, *12*, 025005.
10. Emons, T. T.; Li, J.; Nazar, L. F. *J. Am. Chem. Soc.* **2002**, *124*, 8516.
11. Stefk, M. *et al. Nano Lett.* **2012**, *12*, 5435.
12. Rauda, I. E. *et al. Adv. Funct. Mater.* **2014**, *24*, 6717.
13. Deng, Y.; Wei, J.; Sun, Z.; Zhao, D. *Chem. Soc. Rev.* **2013**, *42*, 4054.
14. Niederberger, M.; Bartl, M. H.; Stucky, G. D. *Chem. Mater.* **2002**, *14*, 4364.
15. Niederberger, M. *Acc. Chem. Res.* **2007**, *40*, 793.
16. Orilall, M. C.; Wiesner, U. *Chem. Soc. Rev.* **2011**, *40*, 520.
17. Jain, A.; Wiesner, U. *Macromolecules* **2004**, *37*, 5665.
18. Rauda, I. E. *et al. ACS Nano* **2012**, *6*, 6386.
19. Hou, K. *et al. Adv. Mater. (Weinheim, Ger.)* **2009**, *21*, 2492.
20. Suzuki, N. *et al. CrystEngComm* **2013**, *15*, 4404.
21. Meuler, A. J.; Hillmyer, M. A.; Bates, F. S. *Macromolecules* **2009**, *42*, 7221.

22. Robbins, S. W.; Sai, H.; DiSalvo, F. J.; Gruner, S. M.; Wiesner, U. *ACS Nano* **2014**, *8*, 8217.
23. Templin, M. *et al. Science* **1997**, *278*, 1795.
24. Brinker, C. J.; Lu, Y. F.; Sellinger, A.; Fan, H. Y. *Adv. Mater. (Weinheim, Ger.)* **1999**, *11*, 579.
25. Kurz, A.; Brakecha, K.; Puetz, J.; Aegeuter M. A. *Thin Solid Films* **2006**, *502*, 212.
26. Kojima, M.; Kato, H.; Gatto M. *Philosophical Magazine Part B* **1993**, *68*, 215.
27. Toombes, G. E. S. *et al. Macromolecules* **2007**, *40*, 8974.
28. Stefk, M. *et al. Chem. Mater.* **2009**, *21*, 5466.
29. Szeifert, J. M. *et al. Chem. Mater.* **2009**, *21*, 1260.
30. Stefk, M. *J. Mater. Chem.* **2012**, *22*, 1078.
31. Finnefrock, A. C.; Ulrich, R.; Toombes, G. E. S.; Gruner, S. M.; Wiesner, U. *J. Am. Chem. Soc.* **2003**, *125*, 13084.

CHAPTER 6

CONCLUSION

In this dissertation, I have explored synthesis and characterization of ordered mesoporous metal oxides and nitrides using block copolymer coassembly as the primary tool: G^A $Ti_{0.8}Nb_{0.2}O_2/Ti_{0.8}Nb_{0.2}N$ and $Ti_{0.5}Nb_{0.5}O_2/Ti_{0.5}Nb_{0.5}N$ (Chapter 2); G^A TiO_2/TiN , G^A $Ti_{1-x}Nb_xO_2/Ti_{1-x}Nb_xN$, and both G^A and G^D Nb_2O_5/NbN (Chapter 3); superconducting ordered mesoporous NbN (Chapter 4); G^A antimony-doped tin oxide from crystalline nanoparticles (Chapter 5).

In Chapter 2, the triblock terpolymer ISO was used as a structure-directing agent to generate freestanding monolithic alternating gyroids of titanium-nitrides with remarkable retention of the macrostructure and mesostructure. These materials also demonstrated electrical conductivity, which is of use for generating mesoporous electrodes for devices. This represented the first report of a freestanding ordered mesoporous transition metal nitrides, opening a new class of very interesting materials that can be generated using block copolymer inorganic coassembly.

In Chapter 3, the versatility of the synthesis of gyroidal transition metal nitrides was explored and expanded. Freestanding monolithic G^A s of the binary oxides and nitrides of TiO_2/TiN and Nb_2O_5/NbN as well as a variety of intermediate $Ti_{1-x}Nb_xO_2$ $Ti_{1-x}Nb_xN$ compositions were synthesized. It was also demonstrated that the high porosity and short solid state distances in G^A oxides facilitate the nitriding process and thus phase purity of the nitrides. Finally, the first G^D nitride structure was demonstrated with NbN. Overall, the utility and versatility of the synthetic strategy for generating ordered mesoporous nitrides was shown.

In Chapter 4, the processing of G^A NbN was optimized to generate the first ordered mesoporous superconductor. The high temperature nitriding was performed in two steps to

generate the freestanding superconducting material that retains its mesoporosity despite rigorous heat treatment. This work demonstrates the power of block copolymer inorganic coassembly as a tool for generating ordered mesoporous superconductors. Using block copolymers to generate ordered mesoporous superconductors should prove fruitful in studying the effects of ordered mesostructure on superconducting behavior.

In Chapter 5, an alternate approach to generating crystalline gyroidal oxides was demonstrated using ISO and antimony-doped tin oxide nanocrystals. This is the first gyroidal ATO structure, and the first ordered mesostructure using a large amphiphilic block terpolymer in combination with crystalline oxide nanoparticles. This synthetic strategy provides an additional pathway to controlling the crystallinity and properties of ordered mesoporous oxides.

In summary, a variety of ordered mesoporous oxides and nitrides with various interesting properties and applications have been synthesized using triblock terpolymers as structure-directing agents. A variety of materials and synthetic techniques have been introduced so one can tune the composition, dimensions, and morphology for the desired application.

By laying the framework for the synthesis and characterization of these ordered mesoporous oxides and nitrides, rigorous studies on the effects of mesostructure on their properties and performance can proceed. For example, studies on the plasmonic and superconducting behavior as a function of mesostructure have already begun on the nitrides. Additionally, studies on the catalytic water splitting behavior of the ordered mesoporous oxides have also begun. It is expected that numerous applications will be explored for ordered mesoporous oxides and nitrides, including energy storage and conversion, plasmonics, and catalysis. Further extensions of the synthetic methods such as careful control of oxidation and nitridation will result in further control over the performance of such materials.